



**Universidade do Estado do Rio de Janeiro**

Centro de Tecnologia e Ciências

Faculdade de Engenharia

Eduardo Vitral Freigedo Rodrigues

**Nano-patterning of surfaces by ion sputtering:  
Numerical study of the anisotropic damped  
Kuramoto-Sivashinsky equation**

Rio de Janeiro

2015

Eduardo Vitral Freigedo Rodrigues

**Nano-patterning of surfaces by ion beam sputtering:  
Numerical study of the anisotropic damped  
Kuramoto-Sivashinsky equation**

Dissertação apresentada, como  
requisito parcial para obtenção  
do título de Mestre em Ciências,  
ao Programa de Pós-Graduação em  
Engenharia Mecânica, da Universidade  
do Estado do Rio de Janeiro. Área de  
concentração: Mecânica dos Sólidos.

Advisor: Prof. Ph.D. Gustavo Rabello dos Anjos  
Co-Advisor: Prof. D.Sc. José da Rocha Miranda Pontes

Rio de Janeiro

2015

Eduardo Vitral Freigedo Rodrigues

**Nano-patterning of surfaces by ion beam sputtering: Numerical study of  
the anisotropic damped Kuramoto-Sivashinsky equation**

Dissertação apresentada, como requisito parcial para obtenção do título de Mestre em Ciências, ao Programa de Pós-Graduação em Engenharia Mecânica, da Universidade do Estado do Rio de Janeiro. Área de concentração: Mecânica dos Sólidos.

Aprovado em: 24 de julho de 2015

Banca Examinadora:

---

Prof. Ph.D. Gustavo Rabello dos Anjos (Orientador)  
Faculdade de Engenharia - UERJ

---

Prof. D.Sc. José da Rocha Miranda Pontes (Co-orientador)  
Faculdade de Engenharia - UERJ

---

Prof. Ph.D. Norberto Mangiavacchi  
Faculdade de Engenharia - UERJ

---

Prof. D.Sc. Rogério Martins Saldanha da Gama  
Faculdade de Engenharia - UERJ

---

Prof. D.Sc. Fernando Pereira Duda  
COPPE - UFRJ

Rio de Janeiro

2015

## **ACKNOWLEDGMENTS**

First and foremost, I would like to acknowledge the fundamental contribution of Prof. Daniel Walgraef to this work. In fact, he was the one who proposed the present research line based on mutual interests, providing all the information and guidance necessary to perform the investigations. I am profoundly grateful for his trust in my capabilities, solely based on Prof. José Pontes recommendations. Thank you for gifting me with such fascinating research subject.

There are no words to express my gratitude towards Prof. José Pontes, my mentor and co-advisor. He is a true friend who supported and inspired me throughout my bachelor years, with whom I had the unique opportunity to work during this Master thesis. His contribution to my education goes beyond the scope of this endeavor. Not only he was my teacher of transport phenomena, numerical methods, linear algebra and differential equations, but I also learned a lot with him about the evolution of science, complex systems and life in general.

I am very grateful for the counseling of my advisor Prof. Gustavo Rabello, who was a young scientist I looked up to even before coming to UERJ. Besides his assistance in many crucial parts of my thesis, he was kind enough to share his experiences with me and to advise me on how to take the initial steps in the research life.

A heartfelt thanks go to:

Prof. Norberto Mangiavacchi, for receiving me into GESAR lab, a center of excellence in numerical simulations, and a marvelous place to work. I am grateful for his feedback during my thesis development, and for assisting me with code verification.

Prof. Rogério Gama, for giving me the mathematical basis for continuum mechanics. I am really happy to have met such exemplar and honorable researcher at UERJ. I appreciated all the fruitful conversations we had.

Prof. Fernando Duda, for the enlightening discussions we had before I decided to enroll in UERJ Master's Program, and also for organizing the 52th Meeting of the Society for Natural Philosophy in Rio. This event triggered my interest in the field of continuum mechanics and mathematical modeling of materials, and besides, it introduced me to a wide range of brilliant professionals. Particularly, it was an amazing experience to be in the presence of Roger Fosdick and Constantine Dafermos.

Prof. Francisco Soeiro, for the top notch classes in Linear Elasticity.

Prof. Renato Cotta, for his encouragement, which was determinant for our resolution to complete this work in one year.

Prof. Leonardo Alves, for sharing his scientific ideals and for his willingness to help.

Prof. Celio Albano, my undergraduate project supervisor, for all the attention and support he gave me during the last years. Working with him motivated me to follow the scientific career, and for this I will be forever grateful.

Prof. Álvaro Coutinho, for his exceptional Finite Elements Method course, which provided me with many hours of entertaining challenges.

Sonia Nina, Jorge Martins and Renata, for their valuable assistance.

Those who received me so well at GESAR: Gustavo Charles, Rodolfo Sobral, and Rachel Lucena. Thank you for being a great company, and for the lessons I learned with each one of you.

My great coworkers at GESAR: Mariana Rocha, Rodrigo Moraes, Apoena Calil, Gabriel Meletti, and Leon Lima.

My beloved girlfriend Glenda, for being the perfect partner. She has been supporting my decisions and cherishing my work for years, and my time with her during the development of this thesis made my weeks much more agreeable and less stressful. Thank you for hearing me talk for hours about crazy stuff happening in atomic scale, mad scientists and my uncertainties towards life. She was also an incredible help in revising the text of this thesis.

My dear parents, for giving me the support and tranquility necessary to make carefree decisions in life, without burdens. I am grateful for all their love, kindness, and for investing so much in my education.

CAPES-Brazil, for the financial assistance.

‘I wish life was not so short,’ he thought.  
‘Languages take such a time, and so do all  
the things one wants to know about.’

*J.R.R. Tolkien,  
The Lost Road and Other Writings*

## RESUMO

**VITRAL, Eduardo** *Nano-patterning of surfaces by ion sputtering: Numerical study of the anisotropic damped Kuramoto-Sivashinsky equation.* 94 f. Dissertação (Mestrado em Engenharia Mecânica) - Faculdade de Engenharia, Universidade do Estado do Rio de Janeiro (UERJ), Rio de Janeiro, 2015.

Apresenta-se uma abordagem numérica para um modelo que descreve a formação de padrões por *sputtering* iônico na superfície de um material. Esse processo é responsável pela formação de padrões inesperadamente organizados, como ondulações, nanopontos e filas hexagonais de nanoburacos. Uma análise numérica de padrões preexistentes é proposta para investigar a dinâmica na superfície, baseada em um modelo resumido em uma equação anisotrópica amortecida de Kuramoto-Sivashinsky, em uma superfície bidimensional com condições de contorno periódicas. Apesar de determinística, seu caráter altamente não-linear fornece uma rica gama de resultados, sendo possível descrever acuradamente diferentes padrões. Um esquema semi implícito de diferenças finitas com fatoração no tempo é aplicado na discretização da equação governante. Simulações foram realizadas com coeficientes realísticos relacionados aos parâmetros físicos (anisotropias, orientação do feixe, difusão). A estabilidade do esquema numérico foi analisada por testes de passo de tempo e espaçamento de malha, enquanto a verificação do mesmo foi realizada pelo Método das Soluções Manufaturadas. Ondulações e padrões hexagonais foram obtidos a partir de condições iniciais monomodais para determinados valores do coeficiente de amortecimento, enquanto caos espaço-temporal apareceu para valores inferiores. Os efeitos anisotrópicos na formação de padrões foram estudados, variando o ângulo de incidência.

Palavras-chave: Sputtering; Método das diferenças finitas; equação de Kuramoto-Sivashinsky.

## ABSTRACT

A numerical approach is presented for a model describing the pattern formation by ion beam sputtering on a material surface. This process is responsible for the appearance of unexpectedly organized patterns, such as ripples, nanodots, and hexagonal arrays of nanoholes. A numerical analysis of preexisting patterns is proposed to investigate surface dynamics, based on a model resumed in an anisotropic damped Kuramoto-Sivashinsky equation, in a two dimensional surface with periodic boundary conditions. While deterministic, its highly nonlinear character gives a rich range of results, making it possible to describe accurately different patterns. A finite-difference semi-implicit time splitting scheme is employed on the discretization of the governing equation. Simulations were conducted with realistic coefficients related to physical parameters (anisotropies, beam orientation, diffusion). The stability of the numerical scheme is analyzed with time step and grid spacing tests for the pattern evolution, and the Method of Manufactured Solutions has been used to verify the scheme. Ripples and hexagonal patterns were obtained from a monomodal initial condition for certain values of the damping coefficient, while spatiotemporal chaos appeared for lower values. The anisotropy effects on pattern formation were studied, varying the angle of incidence.

Keywords: Sputtering; Finite-difference method; Kuramoto-Sivashinsky equation.

## LIST OF FIGURES

Figure 1	Ripples formed by ion sputtering compared to three patterns present in nature	19
Figure 2	Microstructural zoology obtained by the anisotropic DKS equation .....	20
Figure 3	Sputtering mechanism [21]: an energetic particle hits the material's surface and promotes collision cascade of atoms, leading to the ejection of atoms from the solid. ....	21
Figure 4	Regimes of sputtering as a function of the energy: (A) single knock-on, (B) linear collision cascade, (C) thermal spike. Edited from [21] .....	22
Figure 5	Experimental results extracted from Wei et al. (2009) [8]. SEM images of nanohole domains are present in <b>a</b> (low magnification) and <b>b</b> (high magnification). A perfect ordered domain with hexagonal arrays is displayed by <b>c</b> . In <b>c</b> we have two dashed lines, whose cross-sectional height profiles can be seen in <b>d</b> . Image <b>e</b> is a 3D image of the hexagonal pattern constructed from the previous data. ....	25
Figure 6	Experimental results extracted from Gago et al. (2006) [7]. AFM $1 \times 1 \mu\text{m}^2$ images of Si(001) substrates sputtered for 10 min under normal incidence with 1 keV Ar <sup>+</sup> ions. Temperature influence is shown comparing the results for <b>a</b> 300 K, <b>b</b> 425 K, <b>c</b> 475 K, <b>d</b> 500 K, <b>e</b> 525 K, and <b>f</b> 550 K. ....	26
Figure 7	Simplification of the effects caused by ionic incidence according to Sigmund: the ion penetrates the material's matrix and continues up to P, where its kinetic energy is distributed to the neighboring region, defined by the widths $\sigma$ and $\mu$ [15]. ....	27
Figure 8	Illustration of the local reference frame ( $\hat{X}, \hat{Y}, \hat{Z}$ ) and the laboratory coordinate frame ( $\hat{x}, \hat{y}, \hat{z}$ ) [15]. ....	30
Figure 9	Evolution in time of the $L_2$ norm comparing different grid spacing. ....	47
Figure 10	$L_2$ norm of the surface height for the manufactured solution. First and second order error lines are also displayed for comparison. ....	48
Figure 11	$L_1$ norm rate of variation and internal iterations for $\Delta X = 2$ .....	50
Figure 12	$L_1$ norm rate of variation and internal iterations for $\Delta X = 1$ .....	51

Figure 13	$L_1$ norm, internal iterations and maximum values for $\bar{h}_n$ as a function of time $\tau$ , for an initial pattern with $\vec{q} = q_0 \vec{1}_X$ (outside the stable domain), $\Delta\tau = 0.1$ , $\Delta X = \Delta Y = 2$ , on a $256 \times 256$ nodes domain. ....	56
Figure 14	Surface height values $\bar{h}_n$ and their respective Fourier Transform for $\tau = 0$ (initial monomodal pattern with $\vec{q} = q_0 \vec{1}_X$ ). ....	56
Figure 15	Surface height values $\bar{h}_n$ and their respective Fourier Transform for $\tau = 15$ . ....	57
Figure 16	Surface height values $\bar{h}_n$ and their respective Fourier Transform for $\tau = 30$ . ....	57
Figure 17	Surface height values $\bar{h}_n$ and their respective Fourier Transform for $\tau = 40$ . ....	57
Figure 18	Surface height values $\bar{h}_n$ and their respective Fourier Transform for $\tau = 150$ . Each wavelength from the initial pattern was approximately split in two with the decay and growth of new harmonics. The steady state maintains the 1D structure. ....	58
Figure 19	$L_1$ norm, internal iterations and maximum values for $\bar{h}_n$ as a function of time $\tau$ , for an initial pattern with $\vec{q} = q_0 \vec{1}_X$ (inside the stable domain), $\Delta\tau = 0.1$ , $\Delta X = \Delta Y = 2$ , on a $256 \times 256$ nodes domain. ....	59
Figure 20	Surface height values $\bar{h}_n$ and their respective Fourier Transform for $\tau = 0$ (initial monomodal pattern with $\vec{q} = q_0 \vec{1}_X$ ). ....	59
Figure 21	Surface height values $\bar{h}_n$ and their respective Fourier Transform for $\tau = 15$ . ....	60
Figure 22	Surface height values $\bar{h}_n$ and their respective Fourier Transform for $\tau = 150$ . ....	60
Figure 23	Surface height values $\bar{h}_n$ and their respective Fourier Transform for $\tau = 200$ . ....	60
Figure 24	Surface height values $\bar{h}_n$ and their respective Fourier Transform for $\tau = 1250$ . ....	61
Figure 25	Surface height values $\bar{h}_n$ and their respective Fourier Transform for $\tau = 70000$ . A well ordered nanohole pattern is obtained, but some defects remain in the structure, slowly and continuously moving in time. ....	61
Figure 26	$L_1$ norm, internal iterations and maximum values for $\bar{h}_n$ as a function of time $\tau$ , for an initial pattern with $\vec{q} = q_0 \vec{1}_Y$ (inside the stable domain), $\Delta\tau = 0.1$ , $\Delta X = \Delta Y = 2$ , on a $256 \times 256$ nodes domain. ....	62
Figure 27	Surface height values $\bar{h}_n$ and their respective Fourier Transform for $\tau = 0$ (initial monomodal pattern with $\vec{q} = q_0 \vec{1}_Y$ ). ....	63
Figure 28	Surface height values $\bar{h}_n$ and their respective Fourier Transform for $\tau = 150$ . ....	63
Figure 29	Surface height values $\bar{h}_n$ and their respective Fourier Transform for $\tau = 200$ . ....	64
Figure 30	Surface height values $\bar{h}_n$ and their respective Fourier Transform for $\tau = 500$ . ....	64

Figure 31	Surface height values $\bar{h}_n$ and their respective Fourier Transform for $\tau = 750\dots$	64
Figure 32	Surface height values $\bar{h}_n$ and their respective Fourier Transform for $\tau = 40000$ . A nanohole defectless pattern is obtained in the steady state. ....	65
Figure 33	$L_1$ norm, internal iterations and maximum values for $\bar{h}_n$ as a function of time $\tau$ , for an initial pattern with $\vec{q} = q_0 \vec{1}_Y$ (inside the stable domain), $\Delta\tau = 0.1$ , $\Delta X = \Delta Y = 2$ , on a $256 \times 256$ nodes domain. ....	66
Figure 34	Surface height values $\bar{h}_n$ and their respective Fourier Transform for $\tau = 0$ (initial monomodal pattern with $\vec{q} = q_0 \vec{1}_Y$ ). ....	66
Figure 35	Surface height values $\bar{h}_n$ and their respective Fourier Transform for $\tau = 150\dots$	67
Figure 36	Surface height values $\bar{h}_n$ and their respective Fourier Transform for $\tau = 200\dots$	67
Figure 37	Surface height values $\bar{h}_n$ and their respective Fourier Transform for $\tau = 500\dots$	67
Figure 38	Surface height values $\bar{h}_n$ and their respective Fourier Transform for $\tau = 750\dots$	68
Figure 39	Surface height values $\bar{h}_n$ and their respective Fourier Transform for $\tau = 40000$ . A nanohole defectless pattern is obtained in the steady state. ....	68
Figure 40	$L_1$ norm, internal iterations and maximum values for $\bar{h}_n$ as a function of time $\tau$ , for a random initial pattern, $\Delta\tau = 0.1$ , $\Delta X = \Delta Y = 2$ , on a $256 \times 256$ nodes domain. ....	69
Figure 41	Surface height values $\bar{h}_n$ and their respective Fourier Transform for $\tau = 0$ (random initial pattern). ....	70
Figure 42	Surface height values $\bar{h}_n$ and their respective Fourier Transform for $\tau = 15\dots$	70
Figure 43	Surface height values $\bar{h}_n$ and their respective Fourier Transform for $\tau = 200\dots$	70
Figure 44	Surface height values $\bar{h}_n$ and their respective Fourier Transform for $\tau = 400\dots$	71
Figure 45	Surface height values $\bar{h}_n$ and their respective Fourier Transform for $\tau = 1000$ .	71
Figure 46	Surface height values $\bar{h}_n$ and their respective Fourier Transform for $\tau = 49200$ . A nanohole defectless pattern is obtained in the steady state. ....	71
Figure 47	$L_1$ norm, internal iterations and maximum values for $\bar{h}_n$ as a function of time $\tau$ , for a random initial pattern, $\Delta\tau = 0.1$ , $\Delta X = \Delta Y = 2$ , on a $256 \times 256$ nodes domain. Nonlinear coefficients are discarded. ....	72
Figure 48	Surface height value $\bar{h}_n$ for $\tau = 0$ . ....	73
Figure 49	Surface height values $\bar{h}_n$ and their respective Fourier Transform for $\tau = 15\dots$	73
Figure 50	Surface height values $\bar{h}_n$ and their respective Fourier Transform for $\tau = 100\dots$	73
Figure 51	Surface height values $\bar{h}_n$ and their respective Fourier Transform for $\tau = 250\dots$	74

Figure 52	$L_1$ norm, internal iterations and maximum values for $\bar{h}_n$ as a function of time $\tau$ , for an initial pattern with $\vec{q} = q_0 \vec{1}_X$ (inside the stable domain), $\Delta\tau = 0.1$ , $\Delta X = \Delta Y = 1$ , on a $512 \times 512$ nodes domain .....	75
Figure 53	Surface height values $\bar{h}_n$ and their respective Fourier Transform for $\tau = 0$ (initial monomodal pattern with $\vec{q} = q_0 \vec{1}_X$ ). ....	76
Figure 54	Surface height values $\bar{h}_n$ and their respective Fourier Transform for $\tau = 30$ ....	76
Figure 55	Surface height values $\bar{h}_n$ and their respective Fourier Transform for $\tau = 150$ ...	76
Figure 56	Surface height values $\bar{h}_n$ and their respective Fourier Transform for $\tau = 400$ ...	77
Figure 57	Surface height values $\bar{h}_n$ and their respective Fourier Transform for $\tau = 2500$ . 77	
Figure 58	Surface height values $\bar{h}_n$ and their respective Fourier Transform for $\tau = 14630$ . A nanohole defectless pattern is obtained in the steady state. ....	77
Figure 59	Numerical solution for a 2D anisotropic DKS equation - Spatiotemporal chaotic pattern, $\alpha = 0$ .....	79
Figure 60	Numerical solution for a 2D anisotropic DKS equation - Chaotic semi-organized oscillatory behavior, $\alpha = 0.05$ .....	79
Figure 61	Numerical solution for a 2D anisotropic DKS equation - Stationary hexagonal structure, $\alpha = 0.15$ .....	80
Figure 62	Relative anisotropy $A$ versus $\theta$ for $\bar{K} = 5$ and $a_\mu = 4$ .....	81
Figure 63	Numerical result of Eq. 5.1 obtained by Rost and Krug (1995) [17]. The parameters were $\alpha = 1$ and $\beta = -1$ in order to cancel the nonlinearities. Parallel ridges nucleate and coalesce, taking over the system. ....	82
Figure 64	$L_1$ norm rate of variation per time for the reproduction of the results from Rost and Krug with the semi-implicit time splitting scheme.....	83
Figure 65	System of size $512 \times 512$ , showing the evolution in time of Equation 5.1 with $\Delta\tau = 0.01$ , $\alpha = 1$ and $\beta = -1$ . The numerical results obtained through the semi-implicit time splitting reveals the nucleation and growth of parallel ridges.....	83
Figure 66	$L_1$ norm rate of change per time for $\theta = 66.17^\circ$ . Movements in the structure remain until the end, without reaching a stationary state.....	84

Figure 67 Simulation results for a system $512 \times 512$ with an angle $\theta = 66.17^\circ$ . The nonlinearities cancel each other and a well defined direction arises from the unstable mode. This is made clear by the selection of the $\vec{I}_x$ direction for $\tau = 180$ .	85
Figure 68 $L_1$ norm rate of change per time for $\theta = 40^\circ$ . Hexagonal modes emerge around $\tau = 500$ and the stationary state criteria is met at $\tau = 41,960$ .	86
Figure 69 Simulation results for a system $512 \times 512$ with an angle $\theta = 40^\circ$ . Hexagonal modes emerge and reorganize the structure. The final pattern displays the cells connected in the diagonal, like chains.	87

## LIST OF TABLES

Table 1	Parameter values for the MMS .....	46
Table 2	Meshes employed for code verification by MMS .....	47
Table 3	Parameters value and description for scheme stability tests .....	49
Table 4	Parameters used for the preliminary simulations .....	54
Table 5	Parameters for the 66.17° simulation.....	84

## CONTENTS

<b>INTRODUCTION .....</b>	17
<b>1 LITERATURE REVIEW .....</b>	21
<b>1.1 Physics of Sputtering.....</b>	21
1.1.1 Single Knock-On .....	22
1.1.2 Linear Collision Cascade .....	23
1.1.3 Thermal Spike .....	23
<b>1.2 Experimental Results .....</b>	23
1.2.1 Nanohole pattern formation .....	23
1.2.2 Nanodot pattern formation.....	24
<b>1.3 Theoretical Approaches .....</b>	27
1.3.1 Sigmund's Theory .....	27
1.3.2 BH Theory.....	28
1.3.3 Kuramoto-Sivashinsky equation .....	29
1.3.4 Continuum equation for the surface height.....	29
<b>2 MATHEMATICAL MODELLING AND NUMERICAL SCHEME .....</b>	32
<b>2.1 Governing equation .....</b>	32
<b>2.2 The target scheme .....</b>	34
<b>2.3 Internal iterations .....</b>	35
<b>2.4 The splitting scheme .....</b>	36
<b>2.5 Spatial discretization .....</b>	37
<b>2.6 Periodic Boundary conditions .....</b>	39
<b>2.7 Linear Stability Analysis.....</b>	40
<b>3 VERIFICATION AND STABILITY .....</b>	43
<b>3.1 Code Verification .....</b>	43
<b>3.2 The Method of Manufactured Solutions .....</b>	44
3.2.1 Generating a manufactured solution.....	45
3.2.2 Discretization error and order of accuracy .....	46
<b>3.3 Verification results .....</b>	47

3.4	<b>Scheme stability</b> .....	48
3.4.1	Case 1: $\Delta X = 2$ , $64 \times 64$ points in a domain $128 \times 128$ .....	50
3.4.2	Case 2: $\Delta X = 1$ , $128 \times 128$ points in a domain $128 \times 128$ .....	51
3.4.3	Scheme stability discussion .....	52
4	<b>PRELIMINARY RESULTS</b> .....	53
4.1	<b>Anisotropic DKS evolution on preexisting patterns</b> .....	53
4.2	Parameters definition.....	54
4.3	<b>Simulation results</b> .....	55
4.3.1	[Case 1] Initial pattern with $\vec{q} = q_0 \vec{1}_X$ , 14 wavelengths.....	55
4.3.2	[Case 2] Initial pattern with $\vec{q} = q_0 \vec{1}_X$ , 2 wavelengths .....	58
4.3.3	[Case 3] Initial pattern with $\vec{q} = q_0 \vec{1}_Y$ , 2 wavelengths .....	62
4.3.4	[Case 4] Initial pattern with $\vec{q} = q_0 \vec{1}_Y$ , 21 wavelengths.....	65
4.3.5	[Case 5] Initial pattern with random values, ranging from 0 to 0.1 .....	68
4.3.6	[Case 6] Test: Random initial pattern, discarding the nonlinear contribution ....	72
4.3.7	[Case 7] Spatial resolution test, 18 points per critical wavelength: Initial pattern with $\vec{q} = q_0 \vec{1}_X$ , 2 wavelengths .....	74
5	<b>ADVANCED RESULTS</b> .....	78
5.1	<b>The damping term effect</b> .....	78
5.2	<b>Anisotropy and angle of incidence</b> .....	81
	<b>CONCLUSION</b> .....	88
	<b>APPENDIX A - PUBLICATIONS</b> .....	89
	<b>REFERENCES</b> .....	90

## INTRODUCTION

Natural and social sciences present complex systems with remarkable nonlinear behavior, in which the emergence of order may surprise the common sense. In nature, they appear as patterns in vegetation (e.g., *tiger bush* studied by Lefever [1]), climate phenomena (hurricanes, tornadoes), human anatomy (heart beats), and oscillations, just to name a few. These natural systems continuously exchange materials and energy with their environment, since they are open nonequilibrium systems. Human interactions and interference in natural systems also lead to nonlinear phenomena. Social relations and economical agents behavior, such as in stock-market dynamics, are examples of highly nonlinear systems.

The mathematical theory of nonlinear dynamics was successful in modeling some of these phenomena, even though making predictions about a nonlinear system far from equilibrium is a hard task. In highly nonlinear complex systems, the models usually become less accurate, although remaining qualitatively valuable. The issue lies in the mechanism of continuously adding new harmonics to the functions governing the system, which is introduced by the nonlinearities. In our ignorance of the exact initial conditions, strongly diverging solutions may be attained for two close initial states in a dynamical system. This is one possible scenario when distant from equilibrium, and it is known as chaos. The onset of chaos may happen in a system with at least three degrees of freedom, and its main characteristic is the high sensitivity towards the initial conditions.

On the other hand, some of the aforementioned examples make us realize that even in a strongly nonlinear system the onset of order is also possible. Pattern formation or coherent temporal behavior in complex systems may appear due to symmetry breaking instabilities. The spontaneous appearance and evolution of organized states of matter far from equilibrium were described in 1977 by Prigogine and Nicolis as *Dissipative Structures* [2]. Following this investigation, Haken developed in 1983 the concept of *synergetics* to express the cooperative effects resulting from nonlinearities [3], which was also named by Krinsky in 1984 as *self-organization* [4]. Synergy was the most accepted of these terms, and nowadays it is well known in many other fields of knowledge, specially in biology.

During the last decades, huge advances in materials science technologies permitted the processing of new materials and structures through operations in nonequilibrium conditions, dodging the limitations imposed by equilibrium thermodynamics [5]. Among the

techniques, some of the best known are: ion implantation, spark plasma sintering, laser beam melting, glow discharge sputtering and ion beam sputtering. The theoretical comprehension of such processes is still an ongoing challenge, and their mathematical modeling needs more development. These phenomena are complex, and their behavior presents a drastic change: near equilibrium, the temporal evolution can be described by linear equations, while far from equilibrium nonlinearities introduce a variety of new modes, a scenario that may conduct to spatio-temporal chaos or even to stationary ordered structures by synergistic effects.

The present study addresses the development of a numerical scheme in an effort to solve a model proposed to the ion beam sputtering erosion on a material surface. The phenomenon consists on the ionic bombardment of a surface, which may spontaneously develop a well-ordered structure over a large area under certain conditions [6]. In this sense, sputtering is a physical process that may lead to the formation of periodic structures on a surface by removal and reorganization of its atoms. Depending on the energy of the incident ion, a train of collision event may be established, resulting in the ejection of atoms from the matrix. The morphology of the surface can drastically change due to these sputtered atoms, being responsible for the appearance of unexpectedly organized patterns, such as ripples, nanodots and hexagonal arrays of nanoholes (see [7] and [8]). Nanodots were also observed after ion implantation on semiconductors, a process which presents sputtering as a direct consequence [9]. Furthermore, sputtering may promote the faceting of some preexisting structures, such as nanorods and nanonodules [10].

Similar pattern formations can appear between dynamical systems related to very distinct phenomena. For example, the surfaces bombarded by low energy ions have close relatives: sandy deserts, cloud arrangements in the sky and water ripples. Figure 1 compares the ripple formation in nature with a silicon surface sputtered by  $\text{Ar}^+$  ions. The mechanisms, however, couldn't be more different: sand patterns as in Figure 1b result from the dynamical instability of the sand surface submitted to the action of strong wind [11], whereas Figure 1a is an atomic force microscope (AFM) image of a surface eroded by  $\text{Ar}^+$  ions with an energy of 500 eV under 67° (the ripples have a periodicity of 35 nm and a height of 2 nm). These kind of spatial structures are even described by art, as in *La Grenouillère* from Monet (Figure 1d).

Since the sputtering experimental technique has a series of applications, being largely used for depth profiling, surface analysis, micromachining, and sputter deposition by the thin film community, advances in the theoretical comprehension of this phenomenon and

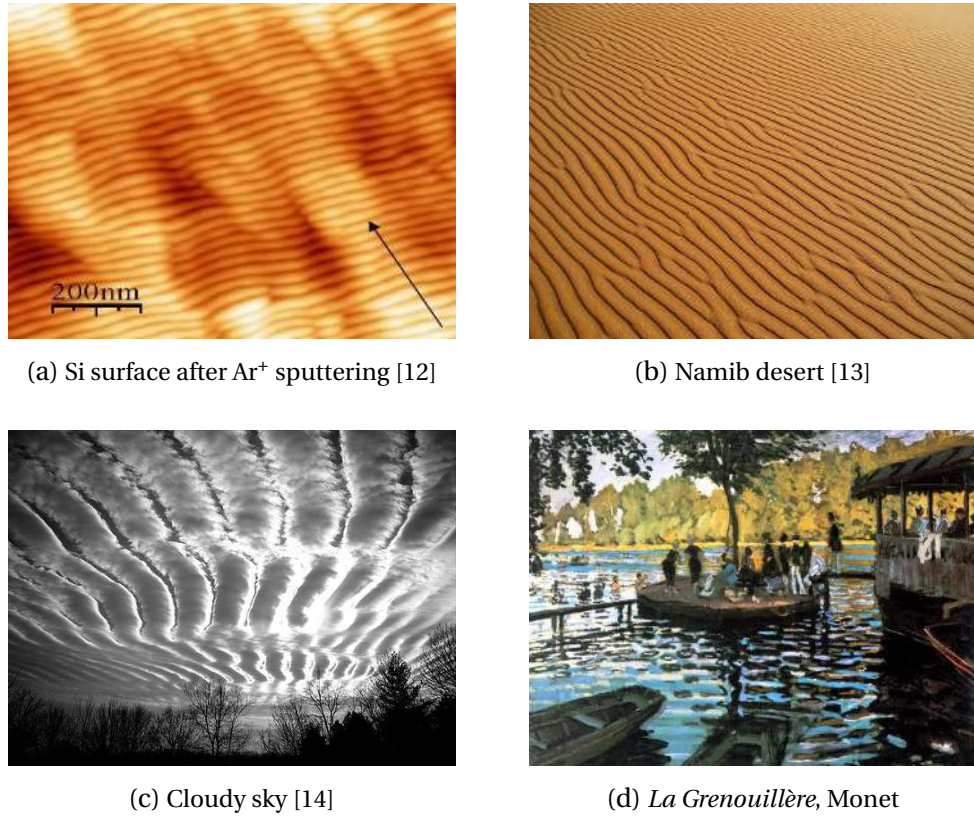


Figure 1: Ripples formed by ion sputtering compared to three patterns present in nature

improvements on the modeling tools will be welcomed by the users. On industrial terms, patterns formed by sputter erosion are of special interest to the semiconductors fabricators, seeing that the technique is used for etching patterns during the production of microelectronic devices [15]. In addition, nanodot formation is being studied for the application on magnetic storage medias, and rippled substrates are attracting attention as templates for thin film deposition [16].

The nonequilibrium regime present in the sputtering process is affected by parameters like incident ion energy, substrate temperature, chemical composition of the material and angle of incidence of the beam. Besides the formation of ripples and other patterns in resultant smooth surfaces, experimental evidences also reveal that under certain conditions the surfaces can become rough, without any of the previous patterns. Although both morphologies result from the same technique, only recently theoretical approaches were proposed to unify their treatment [15].

Continuum theories have been studied to describe surfaces eroded by ion bombardment, reproducing ripple formation and other organized patterns. The Kuramoto-Sivashinsky equation, which was initially formulated to describe flame fronts and chemical waves [15], is

deterministic and highly nonlinear, being capable of producing a great variety of morphologies. Rost and Krug [17] describe the equation as being remarkable for the stabilization of the linear instability by the nonlinear term. This stabilization makes the equation a good candidate to represent the complexity behind the structure formation on sputtered surfaces, specially considering its rich dynamics, capable of representing different regimes. Figure 2 contains some samples of the zoology obtained throughout our work with the damped Kuramoto-Sivashinsky (DKS) equation.

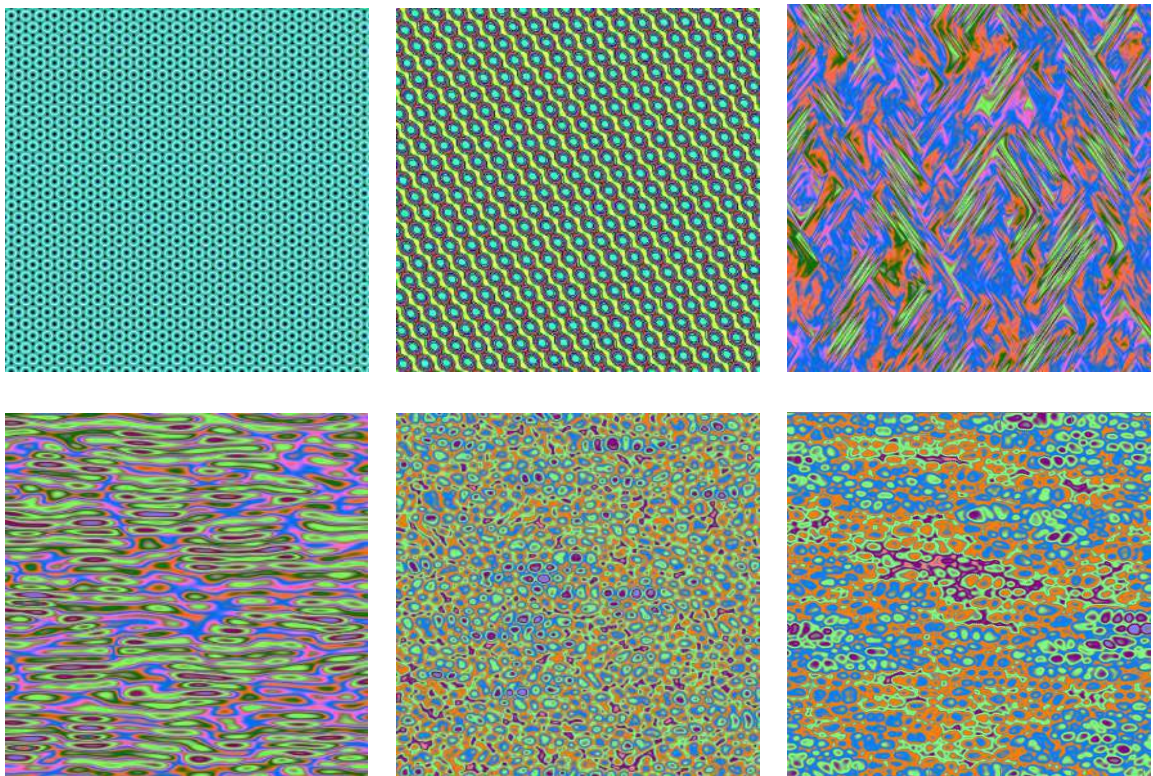


Figure 2: Microstructural zoology obtained by the anisotropic DKS equation

In the present endeavor, a finite-difference semi-implicit splitting scheme of second order in time and space is proposed to numerically solve an anisotropic DKS equation subjected to periodical boundary conditions for two dimensional surfaces. Internal iterations are used inside each time step to enhance the approximation of the nonlinear terms. Previously, a similar numerical scheme was successfully implemented for the Swift- Hohenberg Equation by Chistov et al. [18, 19], which also dealt with the challenges of high-order spatial derivatives and nonlinearity. The numerical scheme is verified by the Method of Manufactured Solutions, and its stability is analyzed with time step and grid spacing tests for the pattern evolution. The simulation results are discussed based on the sputtering physics, previous studies regarding the damping effect on the DKS equation and linear stability analysis predictions.

## 1 LITERATURE REVIEW

### 1.1 Physics of Sputtering

Sputtering is a process which leads to the ejection of atoms from a target solid material by its bombardment by high speed particles [20]. The momentum transfer from the particles to the atoms on the target surface will be responsible for their removal if enough energy is involved. The bombardment is usually made by plasma or ion beam, and prolonged exposure can lead to a significant erosion of the surface. This technique is utilized for various applications: thin-film deposition, pattern etching for the fabrication of integrated circuits, and chemical analysis.

Due to the nature of the present investigation, this section is devoted to the erosion phenomena on materials by ion beam sputtering. These ions are generally controlled in terms of mass and charge, and the beam can be well focused, which makes them drastically different from the ions that arise from plasma (broader energy distribution with random trajectories). The nature of the interaction with the surface will be largely defined by the ion beam energy, leading to some of these outcomes: incoming atoms may be reflected back, scatter, adsorb, sputter surface atoms or get buried in subsurface layers [21].

The momentum exchange between the ions and atoms can promote a train of collision events in the material. If this collision cascade recoils, and enough energy is transferred to the target surface atoms, they can surpass their binding surface energy and be ejected from the material (sputtered). The phenomenon is illustrated by Figure 3.

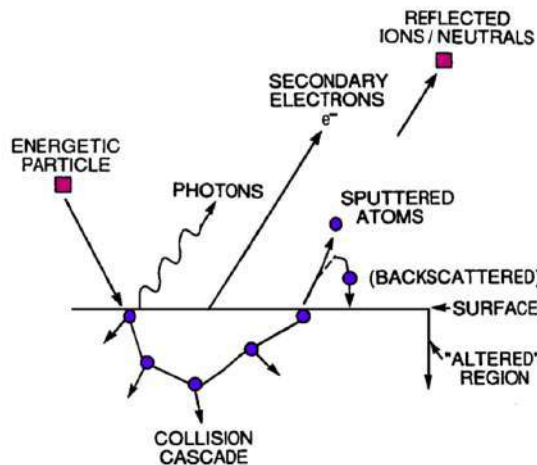


Figure 3: Sputtering mechanism [21]: an energetic particle hits the material's surface and promotes collision cascade of atoms, leading to the ejection of atoms from the solid.

The sputtering yield  $S$  is an important parameter to measure the efficiency of sputtering and can be defined as:

$$S = \frac{\text{Number of sputtered atoms}}{\text{Number of incident ions}} \quad (1.1)$$

This efficiency depends on the binding energy of the target atoms, the nature of these atoms, the incident ion energy, the relative mass of ions and atoms, and the angle of incidence of the ions. Each of them must be taken into account when proposing a mathematical model to the process. The values for  $S$  range from  $10^{-5}$  to  $10^3$  [22], but in most typical uses they are limited from  $10^{-1}$  to 10.

As a function of the incident ion energy, we can distinguish three sputtering regimes: single knock-on (low energy), linear cascade (medium energy) and thermal spike (high energy).

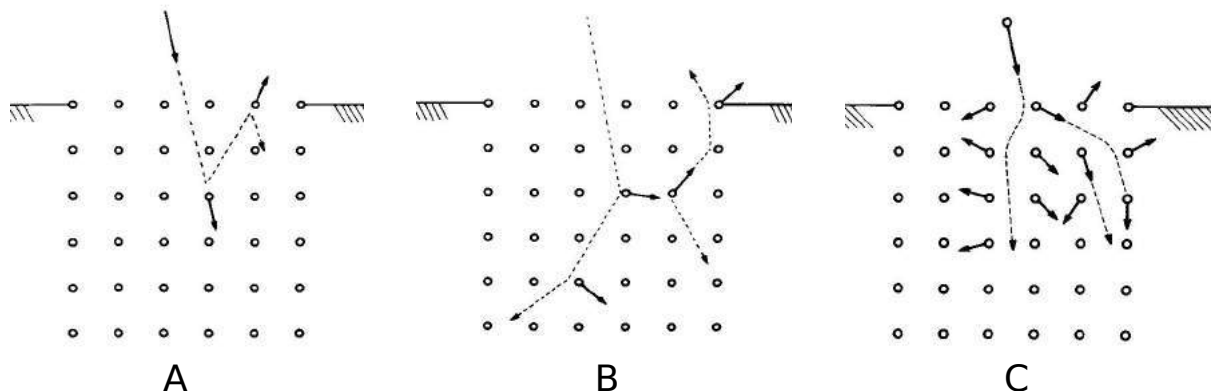


Figure 4: Regimes of sputtering as a function of the energy: (A) single knock-on, (B) linear collision cascade, (C) thermal spike. Edited from [21]

### 1.1.1 Single Knock-On

For incident ions with low energy, separate knock-on events may be initiated if enough energy is transferred during ion-surface collisions, setting atoms in motion and exceeding the binding energy of atoms on the surface to make them sputter. The latter is considered as the heat of sublimation or evaporation (between 2 and 5 eV). However, the threshold energy required for the incident ions will be higher, roughly four times the binding energy if the mass ratio  $M_{\text{ion}}/M_{\text{atom}}$  ranges from 0.08 to 1.

### 1.1.2 Linear Collision Cascade

Increasing the incoming ion energy (100 eV to 10 keV), the density of recoils will be minimal, and most collisions will involve one moving and one stationary particle (instead of two moving particles). Then, linear collision cascades start to take place, and the ultimate result will also be the sputtering of surface atoms. Sigmund's Theory was the first one to successfully model this regime, allowing the sputtering yield to be calculated under the assumption of random slowing down in an infinite medium [23]. Two main stages of the collision cascade were distinguished by this theory: the first one accounts for the slowing down of the primary ion and all recoiling atoms that have comparable energies, which determine the spatial extent of the cascade; the second stage is defined by the creation and slowing down of low energy recoils, comprehending the majority of the atoms set in motion.

### 1.1.3 Thermal Spike

In this regime definition, the term *spike* refers to a high density cascade. This phenomenon occurs when we have the incidence of high energy heavy ions (e.g. Au), with values greater than 100 keV [24, 25], or when bombarding at an elevated target temperature. In this scenario, cascades are so dense that binary encounters of recoiled atoms and collisions of atoms at rest have a similar probability to occur.

## 1.2 Experimental Results

As explained, a train of collision cascades may be established in the solid surface if the energy of the incoming ions is sufficient, resulting in the removal of atoms. The morphology of the surface can drastically change due to these sputtered atoms, and it may result in the formation of unexpectedly organized patterns. In this section, we will review some of the recent experimental results obtained by other authors.

### 1.2.1 Nanohole pattern formation

Wei et al. [8] investigated the low-energy-ion bombardment of semiconductors, focusing their interest in the formation of highly ordered patterns on the surface, since those structures could present optical, electronic and magnetic properties different from those

of the bulk. Their strategy was to take advantage of the morphological instability brought by ion beam sputtering to a surface, driven by the kinetic balance between smoothing and roughening, in order to fabricate ordered patterns over large areas. They were motivated by the lack of experimental data regarding the formation of nanoholes on a sputtered surface, considering it was an expected feature from the previous developed theory regarding the phenomenon.

Through the use of a focused ion beam (FIB) of  $\text{Ga}^+$  ions on a Ge surface at normal incidence, they were able to produce a hexagonally ordered, honeycomb-like structure of holes 35 nm across and 45 nm apart on a Ge surface. This result was acquired with an ion energy of 5 keV, and 5 min long bombardment. They observed the formation of domains ca. 500 nm of hexagonal arrays, separated by lattice defects resembling grain boundaries. In order to study the orientation effect of the crystalline structure planes in the substrate, different orientation samples were bombarded, and no clear distinction was found. This remark is coherent with the development of an amorphous layer on the surface under ion beam sputtering, as discussed by Facsko et al. [26]. Figure 5 contains those experimental results, with scanning electron microscope (SEM) images from the nanohole domains, a cross-sectional height profile, and a 3D surface based on the acquired data.

Four mechanisms are cited as responsible for the pattern formation: sputtering, surface diffusion, redeposition of sputtered atoms, and viscous flow. The DKS equation is mentioned as a growth model capable of describing these four mechanisms, since it was successful in predicting the production of dot patterns during ion bombardment [27]. Regarding the case of dot formation, the nonlinear term of the DKS model is set to positive. Wei et al. also performed a numerical simulation of an isotropic noiseless DKS equation in 2D with a  $512 \times 512$  mesh, and periodic boundary conditions. Their numerical result is in good agreement with the surfaces obtained experimentally, reinforcing the importance of nonlinear effects in the pattern formation by ion beam sputtering.

### 1.2.2 Nanodot pattern formation

Nanodot morphology is another kind of pattern that can be achieved by ion beam sputtering (IBS). They have been achieved by normal beam incidence and also by off-normal beam incidence with simultaneous sample rotation [28]. Gago et al. [7] studied the nanostructuring of nanodot patterns by the bombardment of 1 keV  $\text{Ar}^+$  ions on a Si surface, allowing to

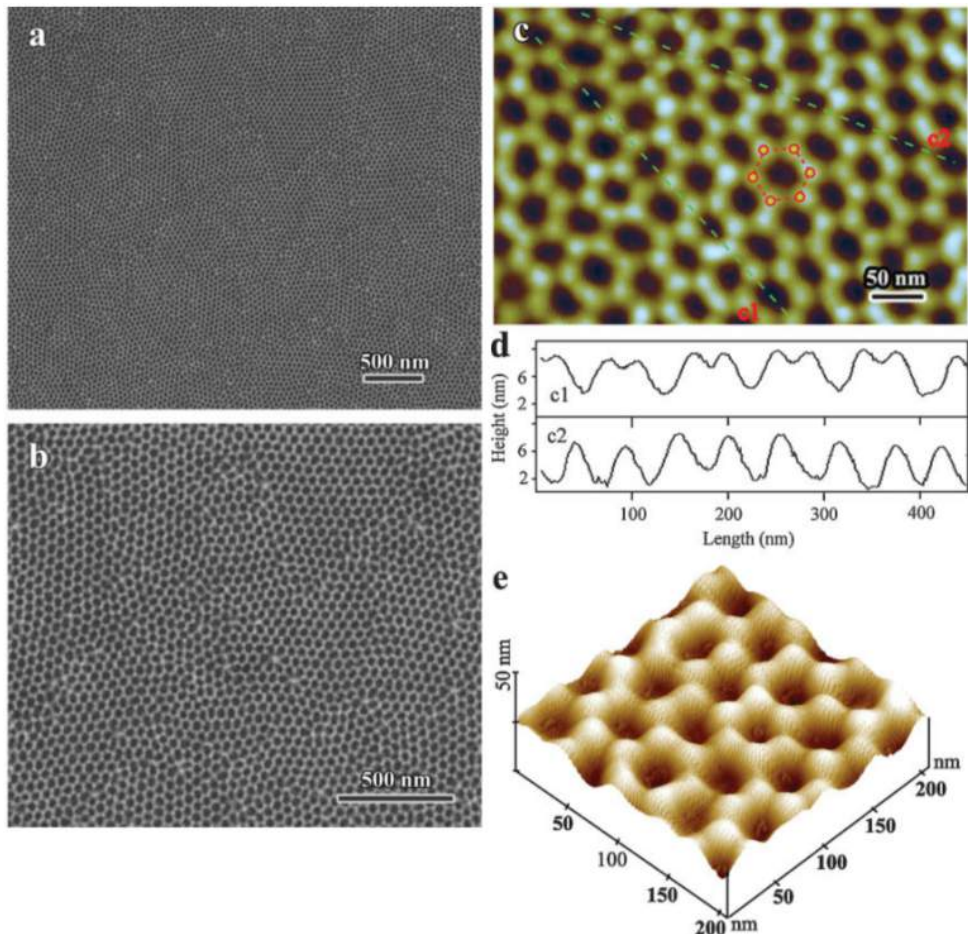


Figure 5: Experimental results extracted from Wei et al. (2009) [8]. SEM images of nanohole domains are present in **a** (low magnification) and **b** (high magnification). A perfect ordered domain with hexagonal arrays is displayed by **c**. In **c** we have two dashed lines, whose cross-sectional height profiles can be seen in **d**. Image **e** is a 3D image of the hexagonal pattern constructed from the previous data.

pattern large surface areas after a few minutes of ion irradiation. The effect of the temperature in the nanostructuring process during IBS was investigated, in the range  $T = 300 - 625$  K, and three different regimes were observed: up to 425 K, the nanodot pattern did not present a significant, with the nanodot volume being mostly crystalline; in the 425 – 525 K range, the nanodot height decreases with T and the crystalline core contribution to the dot morphology progressively diminishes; above 550 K, the nanodot formation is inhibited and the surface becomes flat.

Figure 6 shows six AFM  $1 \times 1 \mu\text{m}^2$  images of Si(001) surfaces bombarded with 1 keV Ar<sup>+</sup> under normal incidence during 10 min, each one for a different temperature. A short-range hexagonal ordered arrays of nanodots appears for  $T = 300$  K, where each dot possesses 40 – 50 nm width and 5 – 6 nm height. After 425 K, the average interdot distant decreases continuously, up to 525 K. For  $T = 550$  K, the nanodot pattern disappears.

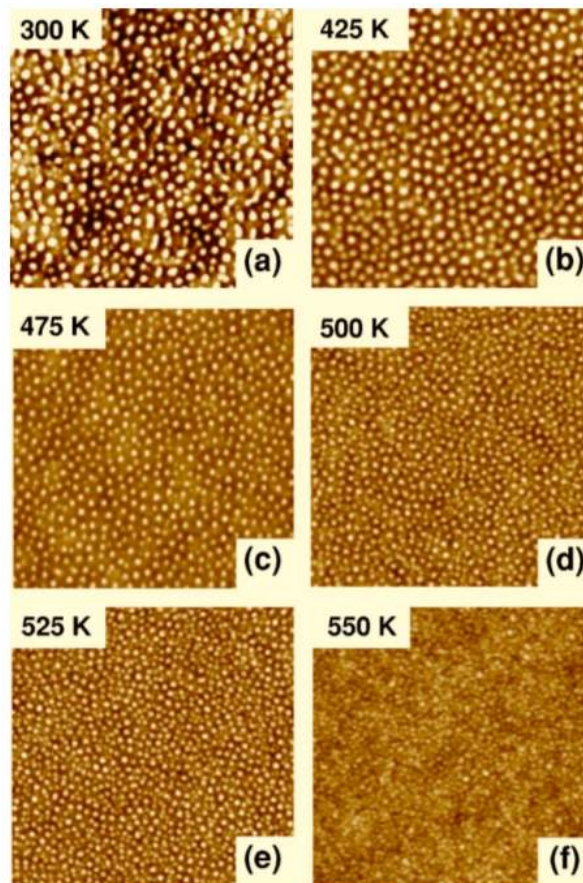


Figure 6: Experimental results extracted from Gago et al. (2006) [7]. AFM  $1 \times 1 \mu\text{m}^2$  images of Si(001) substrates sputtered for 10 min under normal incidence with 1 keV Ar<sup>+</sup> ions. Temperature influence is shown comparing the results for **a** 300 K, **b** 425 K, **c** 475 K, **d** 500 K, **e** 525 K, and **f** 550 K.

### 1.3 Theoretical Approaches

#### 1.3.1 Sigmund's Theory

As previously described, during ion beam sputtering, incoming ions penetrate the material's surface and transfer their kinetic energy to the substrate, leading to an atomic cascade of collisions. Here, we define  $a$  as the average depth where scattering events might culminate in sputtering, which is in the order of the incident ion penetration depth.

A set of transport equations describing the energy transfer during sputtering in an amorphous target was derived by Sigmund [23]. It was the first widely accepted quantitative approach to the phenomenon. One of its biggest contributions was the prediction of the deposited energy distribution.

According to the Sigmund's Theory, the kinetic energy of an ion deposited at a point P inside the bulk of the material will spread following the Gaussian distribution [15]:

$$E(\mathbf{r}) = \frac{\epsilon}{(2\pi)^{3/2}\sigma\mu^2} \exp\left(-\frac{Z'^2}{2\sigma^2} - \frac{X'^2 + Y'^2}{2\mu^2}\right) \quad (1.2)$$

where  $\epsilon$  is the total energy carried by the ion,  $\sigma$  and  $\mu$  are the widths of energy distribution in the directions parallel and perpendicular to the ion beam,  $Z'$  is the distance from  $P$  to point O in Figure 7, and  $X'$ ,  $Y'$  are measured in the perpendicular plane to  $\overline{PO}$ .

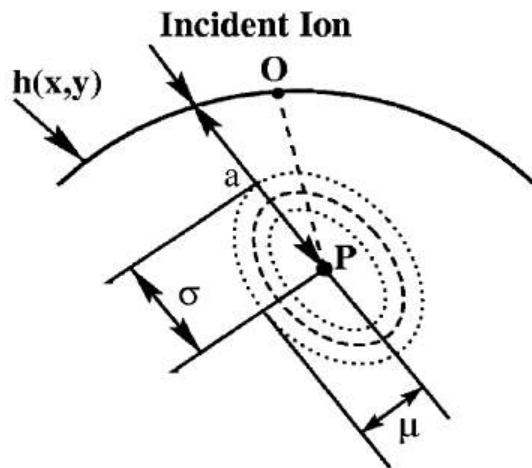


Figure 7: Simplification of the effects caused by ionic incidence according to Sigmund: the ion penetrates the material's matrix and continues up to P, where its kinetic energy is distributed to the neighboring region, defined by the widths  $\sigma$  and  $\mu$  [15].

Equation 1.2 describes the effect of a single incident ion; however, since we consider a surface bombarded by an uniform flux  $J$  of ions, the model must considerate the contribution of multiple ions penetrating different points of the material simultaneously. Therefore, the velocity at an arbitrary point  $O$  will be affected by the energy contributed by all the ions reaching the range of distribution centered at  $O$ . After this remark, the normal erosion velocity at  $O$  can be defined as:

$$V_o = p \int_D \Phi(\mathbf{r}) E(\mathbf{r}) d\mathbf{r} \quad (1.3)$$

In Equation 1.3,  $D$  is the region defined by  $\sigma$  and  $\mu$ ,  $p$  is a material constant related to the surface binding energy and scattering cross section, and  $\Phi$  is a local correction of the uniform flux  $J$  as a function of the local slopes variation.

Despite offering a detailed description of ion bombardment in energetic terms, Sigmund wasn't able to provide information on the morphology of ion sputtered surfaces with his theory. Besides, this theory assumes a planar surface for the incidence, and doesn't take into account the contribution of the surface roughness to the sputtering yield. The derivation of a continuum equation was required to model the erosion dynamics, depending only on the local surface morphology.

### 1.3.2 BH Theory

Another successful theoretical model was developed by Bradley and Harper (BH) in 1988 [29], which used the Sigmund's Theory to relate the sputter yield to the energy deposited onto the surface by the incoming ions. It is a widely accepted approach to describe the process of ripple formation on amorphous substrates, whose wavelength and orientation predictions were in agreement with numerous experimental results. For the first time, ripples were described as a result of a surface instability caused by the curvature dependence of the sputter yield. However, since the equation derived for the BH Theory is linear, it predicts an unbounded exponential growth for the ripple amplitude, and does not sustain for the stabilization of ripples or more sophisticated morphologies.

### 1.3.3 Kuramoto-Sivashinsky equation

The Kuramoto-Sivashinsky (KS) equation comes from the continuum theory and it was initially proposed to characterize flame fronts and chemical waves [30]. This is a deterministic equation, with a highly nonlinear and unstable character. The general formulation for the KS equation is the following:

$$\partial_t h = -|\nu| \nabla^2 h - K \nabla^4 h + \frac{\lambda}{2} (\nabla h)^2$$

The KS equation was studied by a series of authors in relation to the sputter erosion. For small time scales, it presents a stable pattern forming behavior, producing ripple-like structures. For long time scales, the nonlinear effects can lead to the formation of numerous different patterns, as cellular morphologies. Now, it is necessary to formalize the construction of a continuum model to validate the importance of the KS equation to the nano-patterning by ion sputtering.

### 1.3.4 Continuum equation for the surface height

In order to derive a continuum equation for the erosion dynamics [15], the normal component of the erosion velocity  $V_o$  is calculated at a point  $O$  of the surface in a local frame of reference  $(\hat{X}, \hat{Y}, \hat{Z})$  displayed in Figure 8, where axis  $\hat{Z}$  is parallel to the local normal to the surface. Axis  $\hat{X}$  is perpendicular to  $\hat{Z}$  and lies in the same plane formed by  $\hat{Z}$  with the trajectory of the penetrating ion. The third axis,  $\hat{Y}$ , is perpendicular to the plane spanned by  $\hat{X}$  and  $\hat{Z}$ .

Afterward, a laboratory frame  $(\hat{x}, \hat{y}, \hat{h})$  is related to the local frame  $(\hat{X}, \hat{Y}, \hat{Z})$ . This new frame is built starting from a  $\hat{h}$  axis in the direction normal to the uneroded flat surface: axis  $\hat{x}$  is set in the plane generated by  $\hat{h}$  and the incident ion direction, perpendicular to  $\hat{h}$ , while  $\hat{y}$  is perpendicular to the  $(\hat{h}, \hat{x})$  plane. Figure 8 also defines the local angle of incidence  $\phi$ , between  $\hat{Z}$  and the ion trajectory, and the angle  $\theta$ , between  $\hat{h}$  and the ion trajectory.

The equation of motion for the surface profile  $h(x, y, t)$  can be obtained through the projection of the normal component of the erosion velocity onto the  $\hat{h}$  axis. At a point  $O$  on the surface, the time derivative of  $h(x, y, t)$  is proportional to the velocity  $V_o$  (with a minus

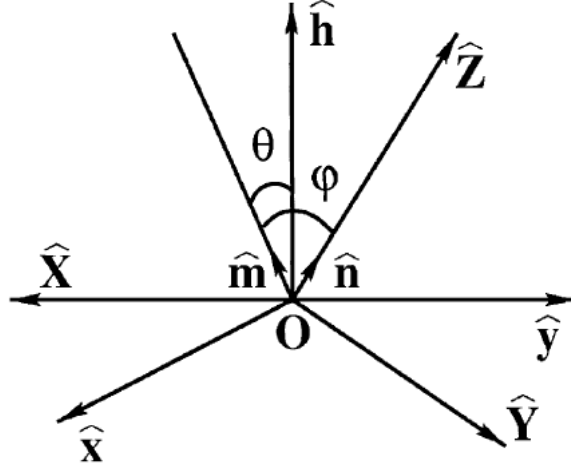


Figure 8: Illustration of the local reference frame  $(\hat{X}, \hat{Y}, \hat{Z})$  and the laboratory coordinate frame  $(\hat{x}, \hat{y}, \hat{z})$  [15].

sign, since it is an erosive process) at  $O$ , and the local normal is considered the gradient of the surface profile  $h(x, y, t)$  at the point  $O$ . The projection will lead to the following development (from a unit vector along the  $\hat{Z}$  axis):

$$\begin{aligned}\hat{n}(\hat{Z}) &= \frac{(-\frac{\partial h}{\partial x}, -\frac{\partial h}{\partial y}, 1)}{\sqrt{g}} \\ g &= 1 + \left(\frac{\partial h}{\partial x}\right)^2 + \left(\frac{\partial h}{\partial y}\right)^2 \\ \frac{\partial h}{\partial t} &= -V_o \sqrt{g}\end{aligned}\tag{1.4}$$

The model can also receive the contribution from surface diffusion effects, represented by  $-K\nabla^4 h$ . Fluctuations in the flux of the bombarding particles are another possible addition, with the shot noise  $\eta(\mathbf{r}, t)$ . Then, we will have the following evolution in time:

$$\frac{\partial h}{\partial t} = -V_o \sqrt{g} - K\nabla^4 h + \eta(\mathbf{r}, t)\tag{1.5}$$

Makeev et al. [15] present a more detailed approach to the model development. From Equation 1.5, performing a small slope expansion, neglecting the noise, and adding a damping term, we obtain the following evolution equation:

$$\begin{aligned}
\frac{\partial h}{\partial t} = & -v_0 - \alpha h - \gamma \frac{\partial h}{\partial x} + \mu \frac{\partial^2 h}{\partial x^2} + \nu \frac{\partial^2 h}{\partial y^2} + \lambda \frac{\partial^3 h}{\partial x^3} + \rho \frac{\partial^3 h}{\partial x \partial y^2} \\
& - D_{xx} \frac{\partial^4 h}{\partial x^4} - D_{xy} \frac{\partial^4 h}{\partial x^2 \partial y^2} - D_{yy} \frac{\partial^4 h}{\partial y^4} - K \left( \frac{\partial^4 h}{\partial x^4} + 2 \frac{\partial^4 h}{\partial x^2 \partial y^2} + \frac{\partial^4 h}{\partial y^4} \right) \\
& + \nu_x \left( \frac{\partial h}{\partial x} \right)^2 + \nu_y \left( \frac{\partial h}{\partial y} \right)^2 + \frac{\partial h}{\partial x} \Omega \left( \frac{\partial^2 h}{\partial x^2}, \frac{\partial^2 h}{\partial y^2}, \left( \frac{\partial h}{\partial x} \right)^2, \left( \frac{\partial h}{\partial y} \right)^2, \dots \right) + \dots
\end{aligned} \tag{1.6}$$

The damping coefficient  $\alpha$  influences the effective growth of the ripple amplitude, and the term  $-\alpha h$  may prevent kinetic roughening, since it induces smoothing of all spatial frequencies [16]. However, the physical meaning of this coefficient is still unclear to the erosive sputtering phenomenon, although some authors affirm that it is related to the redeposition of the sputtered species [8]. The anisotropy comes with the coefficients  $\gamma, \mu, \nu, \lambda, \rho, D_{xx}, D_{xy}, D_{yy}, \mu_x$  and  $\mu_y$ . The next chapter will simplify this model into a damped Kuramoto-Sivashinsky equation before the numerical implementation takes place.

## 2 MATHEMATICAL MODELLING AND NUMERICAL SCHEME

### 2.1 Governing equation

The present study proposes a second order in time finite differences numerical scheme for solving modifications of the generalized Kuramoto-Sivashinsky equation [15, 23, 29, 31, 32]. The general model has the following form:

$$\begin{aligned} \frac{\partial h}{\partial t} = & -v_0 - \alpha h - \gamma \frac{\partial h}{\partial x} + \mu \frac{\partial^2 h}{\partial x^2} + \nu \frac{\partial^2 h}{\partial y^2} + \lambda \frac{\partial^3 h}{\partial x^3} + \rho \frac{\partial^3 h}{\partial x \partial y^2} \\ & - D_{xx} \frac{\partial^4 h}{\partial x^4} - D_{xy} \frac{\partial^4 h}{\partial x^2 \partial y^2} - D_{yy} \frac{\partial^4 h}{\partial y^4} - K \left( \frac{\partial^4 h}{\partial x^4} + 2 \frac{\partial^4 h}{\partial x^2 \partial y^2} + \frac{\partial^4 h}{\partial y^4} \right) \\ & + \nu_x \left( \frac{\partial h}{\partial x} \right)^2 + \nu_y \left( \frac{\partial h}{\partial y} \right)^2 + \frac{\partial h}{\partial x} \Omega \left( \frac{\partial^2 h}{\partial x^2}, \frac{\partial^2 h}{\partial y^2}, \left( \frac{\partial h}{\partial x} \right)^2, \left( \frac{\partial h}{\partial y} \right)^2, \dots \right) + \dots \end{aligned} \quad (2.1)$$

which takes into account realistic coefficients corresponding to anisotropies, diffusion, beam orientation and others. Here,  $h(x, y, t)$  is the height function of the external atom layer and  $\alpha$  is the damping coefficient. The anisotropic coefficients are  $\gamma, \mu, \nu, \lambda, \rho, D_{xx}, D_{xy}, D_{yy}, \mu_x$ , and  $\mu_y$ .  $K$  represents the surface diffusion effects, which varies with temperature. Absorbing  $v_0$  and  $\gamma$  with the transformation  $h \rightarrow -v_0 t + h(x - \gamma t, y)$ , neglecting  $\lambda, \rho$  and  $\Omega$ , and for the case of isotropic energy distribution, Equation 2.1 turns into:

$$\begin{aligned} \frac{\partial h}{\partial t} = & -\alpha h + \frac{Fa}{2} \left( (2s^2 - c^2 - a_\mu^2 s^2 c^2) \frac{\partial^2 h}{\partial x^2} - c^2 \frac{\partial^2 h}{\partial y^2} \right) \\ & + \frac{Fa_\mu^2}{2} c \left( (3s^2 - c^2 - a_\mu^2 s^2 c^2) \left( \frac{\partial h}{\partial x} \right)^2 - c^2 \left( \frac{\partial h}{\partial y} \right)^2 \right) \\ & - \frac{Fa^3}{8a_\mu^2} \left( (c^2 - 4s^2 + 2a_\mu^2 s^2(c^2 - \frac{2}{3}s^2) + \frac{a_\mu^4}{3}s^4 c^2) \frac{\partial^4 h}{\partial x^4} + c^2 \frac{\partial^4 h}{\partial y^4} \right) \\ & - \frac{Fa^3}{4a_\mu^2} (c^2 - 2s^2 + a_\mu^2 s^2 c^2) \frac{\partial^4 h}{\partial x^2 \partial y^2} - K \left( \frac{\partial^4 h}{\partial x^4} + 2 \frac{\partial^4 h}{\partial x^2 \partial y^2} + \frac{\partial^4 h}{\partial y^4} \right) \end{aligned} \quad (2.2)$$

which turns out to be an anisotropic damped Kuramoto-Sivashinsky equation. One of

the simplified and dimensionless form of Equation 2.2 reads:

$$\begin{aligned}\frac{\partial \bar{h}}{\partial \tau} = & -\bar{\alpha} \bar{h} + \bar{\mu} \frac{\partial^2 \bar{h}}{\partial X^2} + \bar{\nu}_x \left( \frac{\partial \bar{h}}{\partial X} \right)^2 + \bar{\nu}_y \left( \frac{\partial \bar{h}}{\partial Y} \right)^2 \\ & - D_{XX} \frac{\partial^4 \bar{h}}{\partial X^4} + D_{XY} \frac{\partial^4 \bar{h}}{\partial X^2 \partial Y^2} + c^2 \frac{\partial^4 \bar{h}}{\partial Y^4} - \bar{K} \left( \frac{\partial^4 \bar{h}}{\partial X^4} + 2 \frac{\partial^4 \bar{h}}{\partial X^2 \partial Y^2} + \frac{\partial^4 \bar{h}}{\partial Y^4} \right)\end{aligned}\quad (2.3)$$

where:

$$\begin{aligned}X &= \frac{2a_\mu}{a} x & Y &= \frac{2a_\mu}{a} y & \tau &= \frac{2Fa_\mu^2}{a} t \\ c &= \cos \theta & s &= \sin \theta & a_\mu &= \frac{a}{\mu} \\ \bar{\alpha} &= \frac{a}{2Fa_\mu^2} \alpha & \bar{\mu} &= 2s^2 - c^2 - a_\mu^2 s^2 c^2 & \bar{h} &= \frac{a_\mu^2}{a} h \\ \bar{\nu} &= -c^2 & \bar{\nu}_x &= c \left( 3s^2 - c^2 - a_\mu^2 s^2 c^2 \right) & \bar{\nu}_y &= -c^3\end{aligned}$$

considering  $\theta$  the angle of incidence of the beam,  $a$  the penetration depth, and  $\mu$  the width of energy distribution.  $\tau$  is the dimensionless time dependency of the transient model, with  $X$  and  $Y$  as the dimensionless domain space coordinates. Furthermore:

$$\begin{aligned}D_{XX} &= \left( c^2 - 4s^2 + 2a_\mu^2 s^2 \left( c^2 - \frac{2}{3}s^2 \right) + \frac{a_\mu^4}{3} s^4 c^2 \right) \\ D_{XY} &= 2 \left( c^2 - 2s^2 + a_\mu^2 s^2 c^2 \right) \\ F &= \frac{J \epsilon p}{\sqrt{2\pi\mu}} \exp \left( -\frac{a_\mu^2 c^2}{2} \right) \\ \bar{K} &= \frac{8a_\mu^2}{Fa^3} K \\ K &= \frac{D_S \rho n_d}{N^2 k_B T} \exp \left( -\frac{\Delta E}{k_B T} \right)\end{aligned}$$

where  $J$  is the flux of bombarding ions,  $\epsilon$  the energy carried by the ions,  $p$  is a term that depends on the surface binding energy and scattering cross-section,  $D_S$  is the surface self-diffusivity,  $\rho$  is the surface free energy per unit of area,  $n_d$  is the density of diffusing atoms,  $N$  is the atomic density,  $k_B$  is the Boltzman constant,  $\Delta E$  is activation energy, and  $T$  the temperature.

For realistic values of the physical parameters:

$$\bar{K} \approx \frac{a_\mu^2 \times 0.54 \times 10^{16}}{T} \exp\left(-\frac{\Delta E \times 1.16 \times 10^4}{T}\right) \exp\left(-\frac{a_\mu^2 c^2}{2}\right)$$

Also, for  $a_\mu = 4$  and high temperatures (present throughout the simulations):

1. The coefficient of  $\partial^2 \bar{h} / \partial X^2$ ,  $\bar{\mu} = 2s^2 - c^2 - a_\mu^2 s^2 c^2$ , is negative for  $0 < \theta < 70.1^\circ$  ( $1.22 \text{ rad}$ ) and positive for  $70.1^\circ < \theta < 90^\circ$ ;
2. The coefficient of  $\partial^2 \bar{h} / \partial X \partial Y$ ,  $\bar{v} = -c^2$ , is negative for any  $\theta$  and smaller than  $\bar{\mu}$  for  $69.3^\circ$  ( $1.21 \text{ rad}$ )  $< \theta < 90^\circ$ ;
3. The coefficient of  $(\partial \bar{h} / \partial X)^2$ ,  $\bar{v}_x = c(3s^2 - c^2 - a_\mu^2 s^2 c^2)$ , is negative for  $0 < \theta < 65.3^\circ$  ( $1.14 \text{ rad}$ ) and positive for  $65.3^\circ < \theta < 90^\circ$ ;
4. The coefficient of  $(\partial \bar{h} / \partial Y)^2$ ,  $\bar{v}_y = c^3$  is negative for any  $\theta$ .

## 2.2 The target scheme

We propose the following second order in time Cranck-Nicolson semi-implicit scheme for solving Equation 2.3 with  $a_\mu = 4$ , high temperatures and  $< 65.3^\circ$  [18, 19]:

$$\frac{\bar{h}^{n+1} - \bar{h}^n}{\Delta \tau} = \Lambda_X \frac{\bar{h}^{n+1} + \bar{h}^n}{2} + \Lambda_Y \frac{\bar{h}^{n+1} + \bar{h}^n}{2} + f^{n+1/2}$$

The superscript  $(n+1)$  refers to the current time and  $(n)$  to the previous one. By including the factor  $1/2$  in the operators  $\Lambda_X^{n+1/2}$ , and  $\Lambda_Y^{n+1/2}$  we rewrite the target scheme as:

$$\frac{\bar{h}^{n+1} - \bar{h}^n}{\Delta \tau} = \Lambda_X (\bar{h}^{n+1} + \bar{h}^n) + \Lambda_Y (\bar{h}^{n+1} + \bar{h}^n) + f^{n+1/2}. \quad (2.4)$$

The operators  $\Lambda_X$ ,  $\Lambda_Y$  and the function  $f^{n+1/2}$  are defined as:

$$\begin{aligned}\Lambda_X &= \frac{1}{2} \left[ -\frac{\bar{\alpha}}{2} - (D_{XX} + K) \frac{\partial^4}{\partial X^4} \right] \\ \Lambda_Y &= \frac{1}{2} \left[ -\frac{\bar{\alpha}}{2} - K \frac{\partial^4}{\partial Y^4} \right] \\ f^{n+1/2} &= \frac{1}{2} \left[ \bar{\mu} \frac{\partial^2}{\partial X^2} - c^2 \frac{\partial^2}{\partial Y^2} + \bar{\nu}_X \left( \frac{\partial \bar{h}^{n+1}}{\partial X} + \frac{\partial \bar{h}^n}{\partial X} \right) \frac{\partial}{\partial X} - c^2 \left( \frac{\partial \bar{h}^{n+1}}{\partial Y} + \frac{\partial \bar{h}^n}{\partial Y} \right) \frac{\partial}{\partial Y} \right. \\ &\quad \left. + (D_{XY} - 2K) \frac{\partial^4}{\partial X^2 \partial Y^2} + c^2 \frac{\partial^4}{\partial Y^4} \right] (\bar{h}^{n+1} + \bar{h}^n)\end{aligned}$$

### 2.3 Internal iterations

Since the operators  $\Lambda_X^{n+1/2}$ ,  $\Lambda_Y^{n+1/2}$  and the function  $f^{n+1/2}$  contain terms in the new stage, we do internal iterations. Besides, internal iterations at each time step are required to secure the approximation for the nonlinearities taking part in the scheme of Equation 2.4. The iterations loop will continue until convergence is attained from monitoring the  $L_\infty$  norm. There is a trade-off related to the time step  $\Delta\tau$ : for a larger  $\Delta\tau$ , convergence will be impaired and the number of internal iterations will increase, while a smaller  $\Delta\tau$  will impact on a smaller number of iterations, but it will imply on a greater number of time steps. The internal iterations scheme reads:

$$\frac{\bar{h}^{n,m+1} - \bar{h}^n}{\Delta\tau} = \Lambda_X(\bar{h}^{n,m+1} + \bar{h}^n) + \Lambda_Y(\bar{h}^{n,m+1} + \bar{h}^n) + f^{n+1/2} \quad (2.5)$$

where the index  $(m)$  refers to the internal iteration number. The superscript  $(n, m+1)$  identifies the new iteration, while  $(n)$  are the values of the previous time step. The superscript  $(n+1)$  for the nonlinear term in the function  $f^{n+1/2}$  will be replaced by  $(n, m)$ , which stands for the values obtained from the previous iteration. The operators  $\Lambda_X^{n+1/2}$ ,  $\Lambda_Y^{n+1/2}$  and the

function  $f^{n+1/2}$  are redefined as:

$$\begin{aligned}\Lambda_X &= \frac{1}{2} \left[ -\frac{\bar{\alpha}}{2} - (D_{XX} + K) \frac{\partial^4}{\partial X^4} \right] \\ \Lambda_Y &= \frac{1}{2} \left[ -\frac{\bar{\alpha}}{2} - K \frac{\partial^4}{\partial Y^4} \right] \\ f^{n+1/2} &= \frac{1}{2} \left[ \bar{\mu} \frac{\partial^2}{\partial X^2} - c^2 \frac{\partial^2}{\partial Y^2} + \bar{\nu}_X \left( \frac{\partial \bar{h}^{n,m}}{\partial X} + \frac{\partial \bar{h}^n}{\partial X} \right) \frac{\partial}{\partial X} - c^3 \left( \frac{\partial \bar{h}^{n,m}}{\partial Y} + \frac{\partial \bar{h}^n}{\partial Y} \right) \frac{\partial}{\partial Y} \right. \\ &\quad \left. + (D_{XY} - 2K) \frac{\partial^4}{\partial X^2 \partial Y^2} + c^2 \frac{\partial^4}{\partial Y^4} \right] (\bar{h}^{n,m} + \bar{h}^n)\end{aligned}$$

The iterations proceed until the following criterion for the  $L_\infty$  norm is satisfied:

$$L_\infty = \frac{\max |\bar{h}^{n,m+1} - \bar{h}^{n,m}|}{\max |\bar{h}^{n,m+1}|} < \delta$$

in all points of the grid for a certain  $M$ . The last iteration gives the sought function  $\bar{h}$  in the new time:

$$\bar{h}^{n+1} \stackrel{\text{def}}{=} \bar{h}^{n,m+1}$$

## 2.4 The splitting scheme

The splitting of Equation 2.4 is made according to the Douglas second scheme [33, 34] (also known as “scheme of stabilizing correction”). This strategy was chosen to deal with the costly procedure of solving Equation 2.5; even though we are dealing with sparse matrices for the operators, the internal iterations makes the process to be repeated several times during each time step. The scheme is designed as follows:

$$\frac{\tilde{\bar{h}} - \bar{h}^n}{\Delta\tau} = \Lambda_X \tilde{\bar{h}} + \Lambda_Y \bar{h}^n + f^{n+1/2} + (\Lambda_X + \Lambda_Y) \bar{h}^n \quad (2.6)$$

$$\frac{\bar{h}^{n,m+1} - \tilde{\bar{h}}}{\Delta\tau} = \Lambda_Y (\bar{h}^{n,m+1} - \bar{h}^n) \quad (2.7)$$

Here,  $\tilde{\bar{h}}$  is the height function for the *half-time* step. In order to show that the splitting

represents the original scheme, we rewrite Eqs. (2.6) and (2.7) in the form:

$$(E - \Delta\tau \Lambda_X) \tilde{\bar{h}} = (E + \Delta\tau \Lambda_X) \bar{h}^n + 2\Delta\tau \Lambda_Y \bar{h}^n + \Delta\tau f^{n+1/2} \quad (2.8)$$

$$(E - \Delta\tau \Lambda_Y) \bar{h}^{n,m+1} = \tilde{\bar{h}} - \Delta\tau \Lambda_Y \bar{h}^n \quad (2.9)$$

where  $E$  is the unity operator. The intermediate variable  $\tilde{\bar{h}}$  is eliminated by applying the operator  $(E - \Delta t \Lambda_X)$  to Equation 2.9, and adding the result to Equation 2.8:

$$\begin{aligned} (E - \Delta\tau \Lambda_X)(E - \Delta\tau \Lambda_Y) \bar{h}^{n,m+1} &= (E + \Delta\tau \Lambda_X) \bar{h}^n + 2\Delta\tau \Lambda_Y \bar{h}^n + \Delta\tau f^{n+1/2} \\ &\quad - (E - \Delta\tau \Lambda_X) \Delta t \Lambda_Y \bar{h}^n \end{aligned}$$

This result may be rewritten as:

$$[E - \Delta\tau (\Lambda_X + \Lambda_Y) + \Delta t^2 \Lambda_X \Lambda_Y] \bar{h}^{n,m+1} = [E + \Delta\tau (\Lambda_X + \Lambda_Y) + \Delta t^2 \Lambda_X \Lambda_Y] \bar{h}^n + \Delta t f^{n+1/2}$$

or either:

$$(E + \Delta t^2 \Lambda_X \Lambda_Y) \frac{\bar{h}^{n,m+1} - \bar{h}^n}{\Delta t} = (\Lambda_X + \Lambda_Y) (\bar{h}^{n,m+1} + \bar{h}^n) + f^{n+1/2} \quad (2.10)$$

A comparison with Equation 2.4 shows that Equation 2.10 is actually equivalent to the first one except by the defined positive operator having a norm greater than one:

$$B \equiv E + \Delta\tau^2 \Lambda_X \Lambda_Y = E + \mathcal{O}(\Delta t^2)$$

which acts on the term  $(\bar{h}^{n,k+1} - \bar{h}^n)/\Delta\tau$ . This means that this operator does not change the steady state solution. Furthermore, since  $\|B\| > 1$ , the scheme given by Equations 2.6-2.7 is more stable than the target one (Equation 2.4).

## 2.5 Spatial discretization

In order to approximate the derivatives of the scheme's differential equation, a Crank-Nicolson semi-implicit finite difference method was employed, as previously mentioned.

This is a second-order central difference method, where the new and old matrices of the surface height are already present at the explained scheme. In this section, the derivatives approximation are displayed.

We make a Taylor development of a function  $f$  in the points of a uniform grid, as follows:

$$\begin{aligned} f_{i-2} &= f_i - 2\Delta x f' + \frac{4\Delta x^2}{2!} f'' - \frac{8\Delta x^3}{3!} f''' + \frac{16\Delta x^4}{4!} f'''' - \mathcal{O}\left(\frac{32\Delta x^5}{5!}\right) \\ f_{i-1} &= f_i - \Delta x f' + \frac{\Delta x^2}{2!} f'' - \frac{\Delta x^3}{3!} f''' + \frac{\Delta x^4}{4!} f'''' - \mathcal{O}\left(\frac{\Delta x^5}{5!}\right) \\ f_{i+1} &= f_i + \Delta x f' + \frac{\Delta x^2}{2!} f'' + \frac{\Delta x^3}{3!} f''' + \frac{\Delta x^4}{4!} f'''' + \mathcal{O}\left(\frac{\Delta x^5}{5!}\right) \\ f_{i+2} &= f_i + 2\Delta x f' + \frac{4\Delta x^2}{2!} f'' + \frac{8\Delta x^3}{3!} f''' + \frac{16\Delta x^4}{4!} f'''' + \mathcal{O}\left(\frac{32\Delta x^5}{5!}\right) \end{aligned}$$

This system can be cast in the form:

$$\begin{pmatrix} -2\Delta x & \frac{4\Delta x^2}{2!} & -\frac{8\Delta x^3}{3!} & \frac{16\Delta x^4}{4!} \\ -\Delta x & \frac{\Delta x^2}{2!} & -\frac{\Delta x^3}{3!} & \frac{\Delta x^4}{4!} \\ \Delta x & \frac{\Delta x^2}{2!} & \frac{\Delta x^3}{3!} & \frac{\Delta x^4}{4!} \\ 2\Delta x & \frac{4\Delta x^2}{2!} & \frac{8\Delta x^3}{3!} & \frac{16\Delta x^4}{4!} \end{pmatrix} \begin{pmatrix} f' \\ f'' \\ f''' \\ f'''' \end{pmatrix} = \begin{pmatrix} f_{i-2} - f_i + \mathcal{O}\left(\frac{32\Delta x^5}{5!}\right) \\ f_{i-1} - f_i + \mathcal{O}\left(\frac{\Delta x^5}{5!}\right) \\ f_{i+1} - f_i - \mathcal{O}\left(\frac{\Delta x^5}{5!}\right) \\ f_{i+2} - f_i - \mathcal{O}\left(\frac{32\Delta x^5}{5!}\right) \end{pmatrix}$$

Considering  $f$  as the function  $h$  in a bidimensional domain, we can define the derivatives by truncating the Taylor's development and arranging the equations. The first derivative with second order accuracy can be written as:

$$\begin{aligned} \frac{\partial h_{i,j}}{\partial X} &= \frac{h_{i+1,j} - h_{i-1,j}}{2\Delta X} \\ \frac{\partial h_{i,j}}{\partial Y} &= \frac{h_{i,j+1} - h_{i,j-1}}{2\Delta Y} \end{aligned}$$

Second derivative with second order accuracy:

$$\frac{\partial^2 h_{i,j}}{\partial X^2} = \frac{h_{i+1,j} - 2h_{i,j} + h_{i-1,j}}{\Delta X^2}$$

$$\frac{\partial^2 h_{i,j}}{\partial Y^2} = \frac{h_{i,j+1} - 2h_{i,j} + h_{i,j-1}}{\Delta Y^2}$$

Fourth derivative with second order accuracy:

$$\frac{\partial^4 h_{i,j}}{\partial X^4} = \frac{h_{i+2,j} - 4h_{i+1,j} + 6h_{i,j} - 4h_{i-1,j} + h_{i-2,j}}{\Delta X^4}$$

$$\frac{\partial^4 h_{i,j}}{\partial Y^4} = \frac{h_{i,j+2} - 4h_{i,j+1} + 6h_{i,j} - 4h_{i,j-1} + h_{i,j-2}}{\Delta Y^4}$$

$$\begin{aligned} \frac{\partial^4 h_{i,j}}{\partial X^2 \partial Y^2} = & \frac{1}{\Delta X^2 \Delta Y^2} \left( h_{i+1,j+1} - 2h_{i+1,j} + h_{i+1,j-1} - 2(h_{i+1,j} - 2h_{i,j} + h_{i-1,j}) \right. \\ & \left. + h_{i+1,j-1} - 2h_{i,j-1} + h_{i-1,j-1} \right) \end{aligned}$$

## 2.6 Periodic Boundary conditions

The boundary condition for the system was chosen to be periodic (PBC), which is less strict than the typical Dirichlet or Neumann conditions. Borrowing the crystal's structure concept of *unit cell*, which is representative of a certain volume of the material, the PBC allows us to treat a domain that would also act as a unit cell for a two-dimensional surface, with *images* being repeated all around the domain. The following expanded matrix of the surface height sheds light on the matter:

$$\begin{array}{cccccc}
& h_{nn} & h_{n1} & h_{n2} & \dots & h_{n(n-1)} & h_{nn} & h_{n1} \\
h_{1n} & \left( \begin{array}{ccccc} h_{11} & h_{12} & \dots & h_{1(n-1)} & h_{1n} \\ h_{21} & h_{22} & & h_{2(n-1)} & h_{2n} \\ \vdots & & \ddots & & \vdots \\ h_{(n-1)1} & h_{(n-1)2} & & h_{(n-1)(n-1)} & h_{n(n-1)} \\ h_{nn} & h_{n1} & h_{n2} & \dots & h_{n(n-1)} & h_{nn} \end{array} \right) & h_{11} \\
h_{2n} & & & & & & h_{21} \\
h_{(n-1)n} & & & & & & h_{(n-1)1} \\
h_{nn} & & & & & & h_{n1} \\
\hline
h_{1n} & h_{11} & h_{12} & \dots & h_{1(n-1)} & h_{1n} & h_{11}
\end{array}$$

Inside the parenthesis lies the system's domain, while the neighboring elements belong to the images. Therefore, when we compute the derivative approximation by finite differences in points near the border of the domain, we will be using elements from the images to perform the calculations, which are, in fact, elements from the opposite side of the domain. This idea is reminiscent of stages or overworld maps from some video games, such as *Pac-Man*, where objects passing through one side of the domain (unit cell) would re-appear on the opposite side maintaining its properties.

## 2.7 Linear Stability Analysis

Linear stability analysis is employed to study the system's behavior when submitted to small perturbations, revealing whether the initial equilibrium point is stable or not. If an exponential growth is observed, such point is linearly unstable; on the other hand, if a exponential decay towards a steady state is found, that point is classified as linearly stable. For small perturbations, we may eliminate the non-linear terms from the governing equation,

making the analytical analysis much easier. Equation 2.3 will take the form:

$$\begin{aligned}\frac{\partial \bar{h}}{\partial \tau} &= -\bar{\alpha} \bar{h} + \bar{\mu} \frac{\partial^2 \bar{h}}{\partial X^2} - c^2 \frac{\partial^2 \bar{h}}{\partial Y^2} - D_{XX} \frac{\partial^4 \bar{h}}{\partial X^4} + D_{XY} \frac{\partial^4 \bar{h}}{\partial X^2 \partial Y^2} + c^2 \frac{\partial^4 \bar{h}}{\partial Y^4} \\ &\quad - \bar{K} \left( \frac{\partial^4 \bar{h}}{\partial X^4} + 2 \frac{\partial^4 \bar{h}}{\partial X^2 Y^2} + \frac{\partial^4 \bar{h}}{\partial Y^4} \right)\end{aligned}\quad (2.11)$$

Considering  $\bar{K} > 1$ , a value of  $\theta$  for  $|\bar{\mu}| > |\bar{v}|$ , and a perturbation  $\bar{h}_p$  from the equilibrium state  $\bar{h}_o$ , we may write Equation 2.11 in Fourier transform:

$$\begin{aligned}\bar{h}(X, Y, t) &= \sum_k \bar{h}_k e^{i(q_x X + q_y Y)} e^{\sigma_\tau t} \\ \sigma_\tau \bar{h} &= [-\bar{\alpha} + (-\bar{\mu} q_x^2) + (-\bar{v} q_y^2) - D_{XX} q_x^4 + D_{XY} q_x^2 q_y^2 + D_{YY} q_y^4 - \bar{K} (q_x^2 + q_y^2)^2] \bar{h}\end{aligned}$$

where  $\vec{q}$  are the spatial modes ( $|q| = \sqrt{q_x^2 + q_y^2}$ ). The decomposition in Fourier modes is reasonable because the basis of trigonometric functions is appropriate to periodic structures. Since  $\bar{v} = -c^3$  is negative for any  $\theta$ , and  $\bar{\mu}$  is negative for  $0 < \theta < 70.1^\circ$ , we operate with the modulus  $|\bar{\mu}|$  and  $|\bar{v}|$ . The anisotropic coefficients  $D_{XX}$ ,  $D_{XY}$  and  $D_{YY}$  can be hidden for an easier manipulation of the equation, observing that  $\bar{K}$  multiplies the same derivatives.

$$\sigma_\tau = -\bar{\alpha} + |\bar{\mu}| q_x^2 + |\bar{v}| q_y^2 - \bar{K} (q_x^2 + q_y^2)^2 \quad (2.12)$$

This is an evolution equation for the amplitude of the mode  $\vec{q}$ , where the eigenvalue  $\sigma_\tau$  is a growth rate. In Equation 2.12 we may consider  $q^2 = q_x^2 + q_y^2$ . Also, if we define the critical wavenumber as  $q_c^2 = \frac{|\bar{\mu}|}{2\bar{K}}$ , the following expression is obtained:

$$\begin{aligned}\sigma_\tau &= (-\bar{\alpha} + |\bar{\mu}| q^2 - \bar{K} q^4) - (|\bar{\mu}| - |\bar{v}|) q_y^2 \\ &= \epsilon - \bar{K} (q^2 - q_c^2)^2 - (|\bar{\mu}| - |\bar{v}|) q_y^2\end{aligned}$$

where  $\epsilon = \frac{\bar{\mu}^2}{4\bar{K}} - \bar{\alpha}$ . On decreasing  $\bar{\alpha}$  bellow  $\frac{\bar{\mu}^2}{4\bar{K}}$ , a positive  $\epsilon$  value is obtained. From this moment on, spatial modes with  $\vec{q} = \pm q_c \vec{1}_x$  become unstable, while distancing from such values we remain in the stable domain.

$$\sigma_\tau = \epsilon - \bar{K} (q_x^2 - q_c^2)^2 \quad [q_y = 0] \rightarrow q_x = q_c$$

Reducing  $\bar{\alpha}$  even further, the unstable domain for  $\vec{1}_x$  modes expands. For  $\bar{\alpha} = \frac{\bar{v}^2}{4\bar{K}}$  and changing modes orientation up to  $\vec{1}_y$ , we can find that modes with  $\vec{q} = \pm\sqrt{\frac{\bar{v}}{2\bar{K}}}\vec{1}_y$  become first unstable in this direction. The calculus is performed as follows:

$$\begin{aligned}\sigma_\tau &= \frac{\bar{\mu}^2 - \bar{v}^2}{4\bar{K}} - \bar{K}(q^2 - q_c^2)^2 - (|\bar{\mu}| - |\bar{v}|)q_y^2 \\ &= \frac{\bar{\mu}^2}{4\bar{K}} - \frac{\bar{v}^2}{4\bar{K}} - \bar{k}q_y^4 + q_y^2|\bar{v}| - \frac{\bar{\mu}^2}{4\bar{K}} + q_y^2|\bar{\mu}| - q_y^2|\bar{v}| \\ &= -\frac{\bar{v}^2}{4\bar{K}} - q_y^2(\bar{K}q_y^2 - |\bar{v}|) \rightarrow q_y = \pm\sqrt{\frac{\bar{v}}{2\bar{K}}}\end{aligned}$$

From the previous analysis, we can conclude that for  $\bar{\alpha} < \frac{\bar{v}^2}{4\bar{K}}$ , modes for all orientations will become unstable. However, it must be noticed that the maximum growth rate is limited at  $q_c\vec{1}_x$ , since the term  $\bar{K}(q^2 - q_c^2)^2$  acts as a wave filter.

The developed linear stability analysis does not take into account the anisotropy of the system nor weakly nonlinear effects. A more robust analysis (which includes a convolution integral obtained from the nonlinear terms) reveals that these structures may be replaced by the fastest hexagonal pattern, whose modes are of equal amplitude but have different wavevectors in order to deal with the anisotropy [35].

### 3 VERIFICATION AND STABILITY

#### 3.1 Code Verification

Computer predictions of the explored physical events should always have their accuracy and validity questioned, specially without a reliable source at hand to compare the numerical results of the simulations. In order to grasp the level of reliability related to a computer prediction of a complex event, verification and validation (V&V) techniques have arisen. Verification denotes the process of determining if a computational model, originated as a discretization of a mathematical model, and the code by which it is implemented, can undergo the task of representing the mathematical model of the physical event with sufficient accuracy. Validation, on the other hand, is related to the process of determining if the developed mathematical model of a physical event truly represents this event with sufficient accuracy [36].

Simply put, verification is related to solving the chosen equations correctly, and validation focus on choosing the right equations to describe the event. The main aspects of verification are code verification, which tries to ensure at a maximum degree that there are no bugs or inconsistencies in the solution algorithm, and solution verification, which quantifies the numerical errors from the simulations (e.g., discretization error and round-off error) [37].

One test possibility for code verification is the Comparison Method, in which the code is compared to an established code to solve similar problems. Comparing the results for a same test case, the user's code would be evaluated with an acceptance criterion based on the maximum difference in the solutions. However, its main downside consists on the difficulty of finding a comparable code, which is the present case [38]. Even if such code exists, and the test is successful, the verification won't be fully secured, since there is the possibility that both codes present the same mistake.

Another technique widely used and more rigorous than the latter is the Method of Exact Solutions (MES). This method compares the numerical results from the developed code with the exact solution from the mathematical model; if the difference between the results exceeds a certain criterion, the code fails the test, and an implementation mistake is pointed as the possible culprit. Despite its effectiveness, the MES is bounded by the availability of analytical solutions, which become harder to be acquired as the geometry and physics of the problem grow in sophistication, and also by the difficulty of implementation of these

solutions [39].

### 3.2 The Method of Manufactured Solutions

The Method of Manufactured Solutions (MMS) arises as an easier alternative to the MES. In face of the challenge to find an exact solution to the governing equations, the MMS proposes the construction of an artificial solution: the idea is to solve the problem backwards, creating a manufactured solution to a system of partial differential equations. Since the proposed function is unlikely to solve the equations exactly, a residual term is expected. Utilizing this residue as a source term on the code, the modified equation is then solved to recover a numerical solution. The latter is then compared with the results from the artificial function and their agreement analyzed.

Code verification by the use of artificial functions and grid convergence was initially studied by Roache and Steinberg [40], for the purpose of verifying a set of elliptic partial differential equations through symbolic manipulation. Schematically, the MMS for order of accuracy verification can be divided into the following steps:

1. Determine the governing equations and their structure
2. Select the function for the artificial solution
3. Substitute the manufactured solution in the governing equations, differentiating with symbolic manipulation
4. For multiple meshes with different grid spacing, solve the modified governing equations with the addition of the source term from Step 3
5. Comparing the numerical solutions from Step 4 with the exact solution from the manufactured function, calculate the global discretization error
6. Acquire the observed order of accuracy after testing with different grids

In terms of the proposed problem, we take all the members of the anisotropic Kuramoto-Sivashinski equation and consider the following differential equation:

$$F(\bar{h}) = 0 \quad (3.1)$$

where  $\bar{h}$  is the second order tensor that describes the surface height and satisfies the equation. Due to the lack of an analytical solution, we propose a manufactured function  $\bar{h}_m$  which will produce a residual  $f$  if applied to Eq. 3.1. This term can be seen as an additional forcing function, leading to a modified operator with this new source

$$\bar{F}(s) \equiv F(s) - f \quad (3.2)$$

For the previous equation,  $\bar{F}(\bar{h}_m)$  equals 0 and  $\bar{F}(\bar{h})$  equals  $-f$ . With this new approach to the problem, we must find an approximate numerical solution  $\bar{h}_k$  for the discretized domain so that  $\bar{F}(\bar{h}_k) = 0$  or  $F(\bar{h}_k) = f$ . The source term is a minimal intrusion to the code's formulation. For Eq. 3.2, the manufactured function will be the exact analytical solution that exercises all of the differential terms from Eq. 3.1, if well constructed. Considering that the code's numerical formulations guarantees an approximation error bound by a constant multiple of best-case interpolation error [39], the new numerical solution  $\bar{h}_k$  will be expected to agree with the manufactured solution  $\bar{F}(\bar{h}_m)$ , limited only by iterative errors and rounding.

### 3.2.1 Generating a manufactured solution

In consonance with the guidelines for the manufactured solution construction by Roache [38], an artificial solution was developed considering spatio-temporal variations of a surface:

$$\bar{h}_m = h_o + h_{xy} \sin\left(\frac{a_x \pi x}{L}\right) \cos\left(\frac{a_y \pi y}{L}\right) e^{bt}$$

The parameter values employed in the manufactured solution and in the differential equation are present on Table 1. Although the artificial solution does not need to be realistic for code verification, the chosen values were coherent with the studied simulations. All tests were run in a quadratic domain with  $L = 256$ , and a time step of  $\Delta t = 0.1$ .

Table 1: Parameter values for the MMS

<b>MS Parameters</b>	<b>Value</b>	<b>KS Parameters</b>	<b>Value</b>
$h_o$	0	$\bar{K}$	5
$h_{xy}$	$10^{-4}$	$a_\mu$	4
$a_x$	2	$\theta$	$30^\circ$
$a_y$	2	$\bar{\alpha}$	0.15
$b$	-1/200		

### 3.2.2 Discretization error and order of accuracy

The global discretization error can be examined by the  $L_2$  norm:

$$L_2 = \left( \frac{\sum_{i=1}^N |\bar{h}_{i,k}^n - \bar{h}_{i,m}^n|^2}{N} \right)^{1/2}$$

where  $N$  is the total number of mesh nodes, and the index  $i$  stands for each one of them. This norm analyzes how far from the analytical solution is the numerical after each iteration, and it is expected to decrease by refining the mesh.

Since we have a second-order scheme, the formal order of accuracy is two. The observed order of accuracy of the code can be acquired from the global discretization error for meshes with different grid spacing, and can be described by the following relation:

$$p = \frac{\ln \left( \frac{L_2^{MB}}{L_2^{MA}} \right)}{\ln(r)}$$

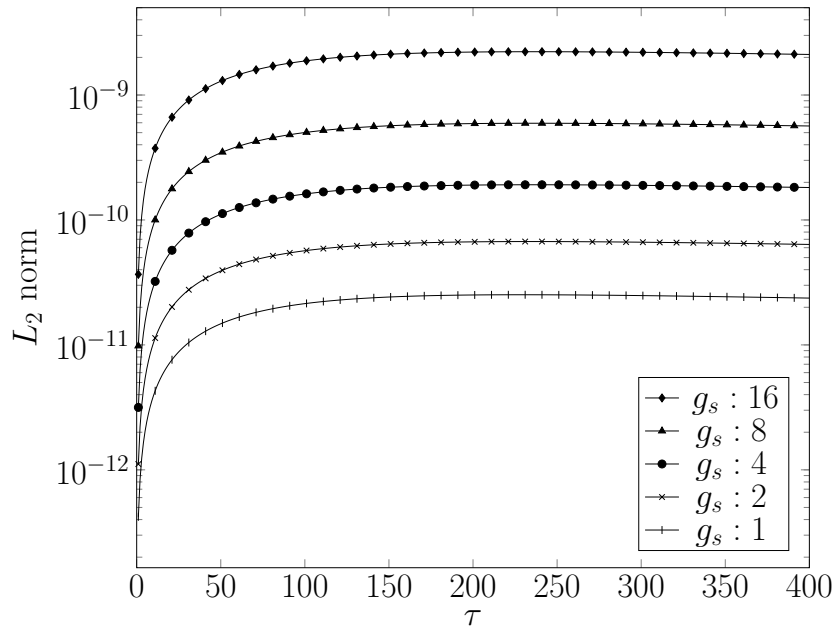
where  $L_2^{MA}$  and  $L_2^{MB}$  are the  $L_2$  norm for meshes A and B respectively, and  $r$  is the ratio of the grid spacing ( $g_s$ ) of mesh B to A. The meshes employed for the present tests with their number of nodes and grid spacing are shown in Table 2.

Table 2: Meshes employed for code verification by MMS

<b>Mesh</b>	<b>Number of nodes</b>	<b>Grid spacing, <math>g_s</math></b>
Mesh A	256 x 256	1
Mesh B	128 x 128	2
Mesh C	64 x 64	4
Mesh D	32 x 32	8
Mesh E	16 x 16	16

### 3.3 Verification results

Figure 9 and Figure 10 display how the spatial grid-refinement affects the global discretization error. The error trends toward second-order convergence with respect to grid spacing for coarser meshes. However, as the grid gets more refined, the error stands between first and second-order convergence.

Figure 9: Evolution in time of the  $L_2$  norm comparing different grid spacing.

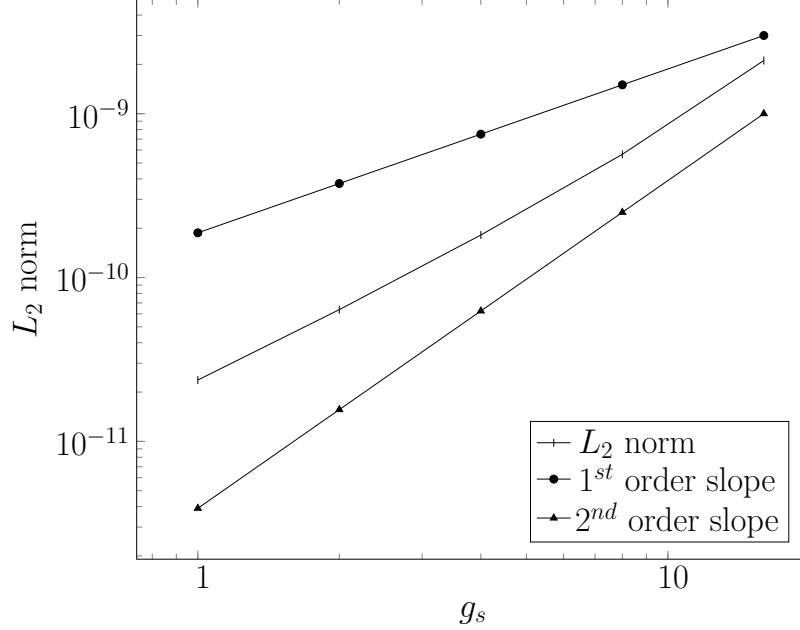


Figure 10:  $L_2$  norm of the surface height for the manufactured solution. First and second order error lines are also displayed for comparison.

The manufactured solution was unstable for the analyzed differential equation, which grows rapidly in time until its saturation, dominating the result over the source term. For this reason, we limited the range of analysis to a stable region for the artificial function, where the numerical solution converges with the analytical solution. As we will later discuss, this region corresponds to a stage before the emergence of hexagonal modes.

### 3.4 Scheme stability

Besides verification, another important issue that concerns the simulations is the time and mesh size selection, since we must maintain the semi-implicit scheme stable. Here, we study the time step and grid spacing variation effect regarding the pattern evolution, which is translated by the  $L_1$  norm curve. The computational effort was also measured, which is related to the number of internal iterations when comparing results for a same grid spacing.

1. Case 1:  $\Delta X = 2$ ,  $64 \times 64$  points in a domain  $128 \times 128$
2. Case 2:  $\Delta X = 1$ ,  $128 \times 128$  points in a domain  $128 \times 128$

Both cases start with a monomodal initial pattern  $q_o \vec{1}_x$ , presenting four wavelengths in the domain. The critical wavelength (related to critical wavenumber  $q_c$ ) is approximately

18: if the system presents this wavelength, each wave would be represented by 9 points for Case 1 and by 18 points for Case 2. The parameters adopted for the tests are displayed in Table 3.

Table 3: Parameters value and description for scheme stability tests

Parameter	Value	Description
$\bar{\alpha}$	0.15	damping coefficient
$\bar{K}$	5	surface diffusion effects
$\theta$	30°	beam's angle of incidence
$a_\mu$	4	penetration depth/width of energy distribution

During the simulations, we monitored the pattern's evolution by the  $L_1$  norm rate of change in time, which indicates how fast the structure is changing between the current and previous time step, normalized by the spatial average of the modulus of the surface height. This norm rate of variation is denoted as:

$$L_{1,t} = \frac{1}{\Delta\tau} \frac{\sum_{ij} |\bar{h}_{ij}^{n+1} - \bar{h}_{ij}^n|}{\sum_{ij} |\bar{h}^{n+1}|} \quad (3.3)$$

We assumed a pattern as stationary if the criterion  $L_{1,t} < 10^{-7}$  was reached for the temporal evolution. On the other hand, the simulation would be stopped if the  $L_1$  curve clearly demonstrated a behavior converging to a fixed value (or oscillating around it). The advantage of following this parameter is its capability of capturing some effects of the phase dynamics. For example, even if the morphology and the surface height are steady, the structure may continue to move sideways, which would affect the  $L_1$  rate of variation. Even though  $L_{1,t}$  is a rate of change and not the  $L_1$  norm, we will refer  $L_{1,t}$  just as  $L_1$  for the sake of simplicity.

Returning to the scheme stability, Figure 11 and Figure 12 compare the structure evolution through the  $L_1$  parameter to observe when the results would diverge for an increasing time step.

### 3.4.1 Case 1: $\Delta X = 2$ , $64 \times 64$ points in a domain $128 \times 128$

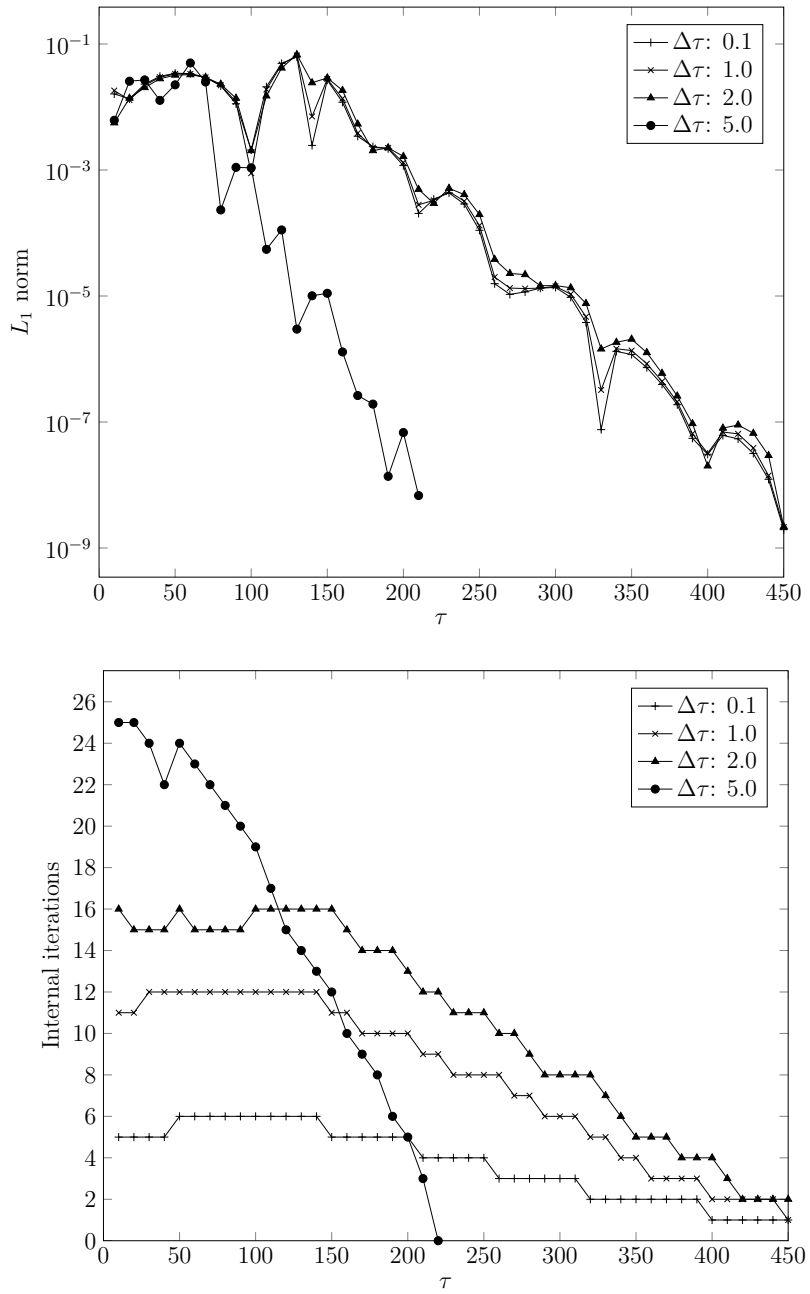


Figure 11:  $L_1$  norm rate of variation and internal iterations for  $\Delta X = 2$

### 3.4.2 Case 2: $\Delta X = 1$ , $128 \times 128$ points in a domain $128 \times 128$

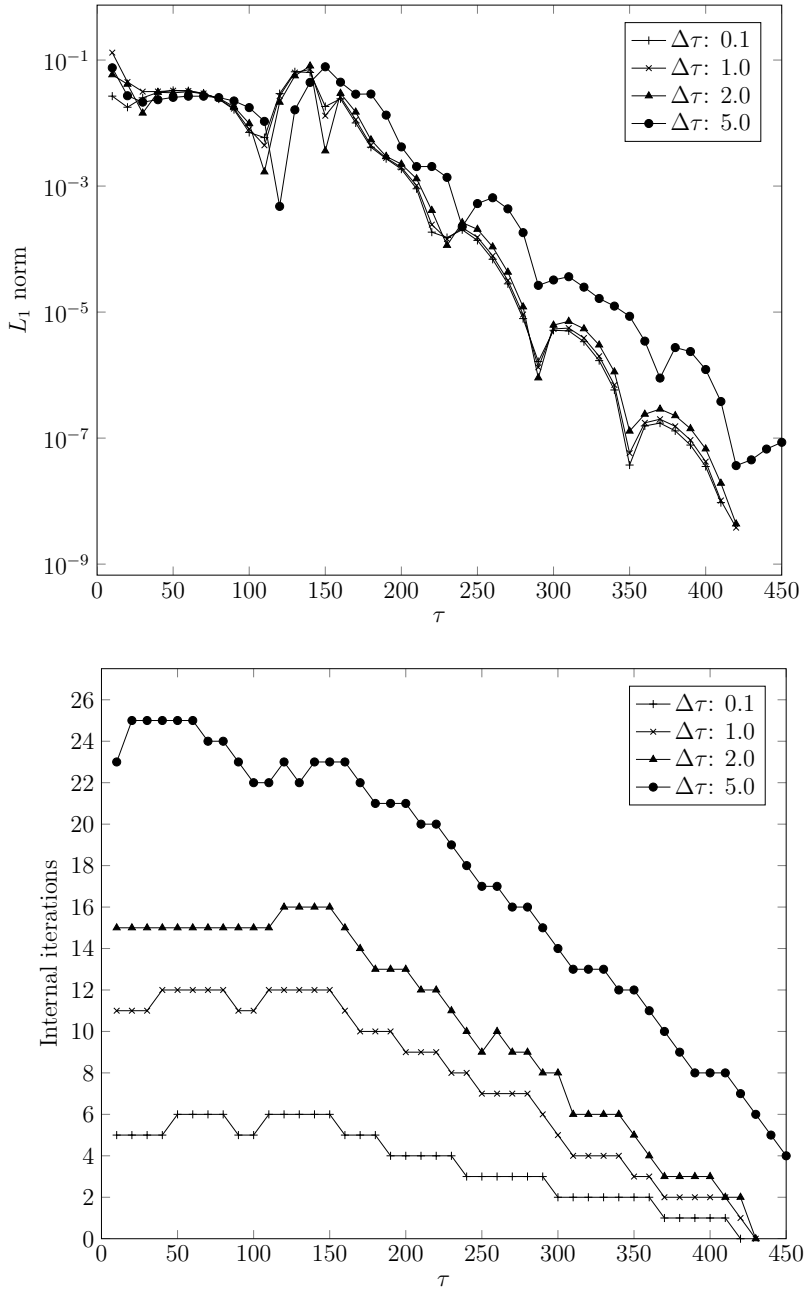


Figure 12:  $L_1$  norm rate of variation and internal iterations for  $\Delta X = 1$

### 3.4.3 Scheme stability discussion

From Figure 11 (Case 1) we observe slight deviations in the  $L_1$  norm evolution for  $\Delta\tau = 2$  when comparing to inferior time steps values, while  $\Delta\tau = 5$  diverges completely from the others. Regarding Figure 12 (Case 2), the divergence for  $\Delta\tau = 5$  is also clear, but it's more coherent with the smaller time steps than Case 1, as expected from a more refined mesh. This time,  $\Delta\tau = 2$  is more consistent with the smaller ones, and would be accepted for the simulations. Even so, we decided to operate with  $\Delta\tau = 1.0$  for  $\Delta X = 1$ , which is a more conservative approach.

## 4 PRELIMINARY RESULTS

### 4.1 Anisotropic DKS evolution on preexisting patterns

In the present chapter, we show the first simulation results for cases with  $\tilde{K} = 5$  and  $\theta = 0.5236$  ( $30^\circ$ ), using a mesh consisting of  $256 \times 256$  points, and a dimensionless grid spacing of  $\Delta = 2$ . These are preliminary results regarding the evolution of the anisotropic DKS on preexisting patterns and on random initial patterns. The seven cases that will appear in our discussion, in respect to the wavenumber of the initial pattern and number of wavelengths present in the starting domain, are the following :

1. Initial pattern with  $\vec{q} = q_0 \vec{1}_X$ , 14 wavelengths ( $q_0 = 1.7181 \cdot 10^{-1}$ )
2. Initial pattern with  $\vec{q} = q_0 \vec{1}_X$ , 2 wavelengths ( $q_0 = 2.4544 \cdot 10^{-2}$ )
3. Initial pattern with  $\vec{q} = q_0 \vec{1}_Y$ , 2 wavelengths ( $q_0 = 2.4544 \cdot 10^{-2}$ )
4. Initial pattern with  $\vec{q} = q_0 \vec{1}_Y$ , 21 wavelengths ( $q_0 = 2.5771 \cdot 10^{-1}$ )
5. Initial pattern with random values, ranging from 0 to 0.1
6. Test: Random initial pattern, discarding the nonlinear contribution
7. Spatial resolution test, 18 points per critical wavelength:

Initial pattern with  $\vec{q} = q_0 \vec{1}_X$ , 2 wavelengths

The first five cases analyze the influence of the initial pattern on the evolution of the structure, the sixth is a test case for the linear terms, and the final case repeats the second one with a higher spatial resolution. This last simulation is an attempt to understand if the remaining defects from case 2 stationary structure were related to the low number of points per wavelength.

An important observation must be made concerning the time step. For cases 1 - 6, we kept  $\Delta\tau = 0.1$ , which was a very conservative approach and lower than it could be, since previous tests revealed that for a spatial resolution of 9 or 18 points per wavelength, time steps up to  $\Delta\tau = 2$  would not significantly affect the stability. Some of those simulations took almost two weeks in our computers, and it was not satisfactory. Therefore, after the preliminary results, we adopted  $\Delta\tau = 1$ , and optimized the code, conducting to a great reduction in the

simulations duration: they were reduced in approximately 10 times, leading to runs in the order of a day for the present cases. Compiled *Matlab* would be a possible solution to make the code even faster.

#### 4.2 Parameters definition

All cases in this chapter ran with the same parameter values, except for the absence of nonlinear terms in case 6, and for the smaller grid spacing in case 7. The total number of time steps ( $n\tau$ ) is not predetermined, since we used the  $L_1$  norm to control the length of the simulations. Table 4 contains these parameters, with their values and descriptions.

Table 4: Parameters used for the preliminary simulations

Parameter	Value	Description
L	512	domain side
np	256	nodes per mesh side
$\bar{\alpha}$	0.15	damping coefficient
$\bar{K}$	5	surface diffusion effects
$\Delta X, \Delta Y$	2	grid spacing
$\theta$	$30^\circ$	angle of incidence of the beam
$\Delta\tau$	0.1	time step
$n\tau$	-	number of time steps
$a_\mu$	4	penetration depth/width of energy distribution
T	500	Temperature (K)
$\Delta E$	1.25	activation energy (eV)
J	10	flux of bombarding ions (ions nm $^{-2}$ s $^{-1}$ )
$\epsilon$	500	energy carried by the ions (eV)

Before proceeding, there are some important remarks to be made about the chosen values:

- The value for  $\bar{\alpha}$  was chosen inside the range  $\frac{\bar{v}^2}{4(\bar{K} + D_{YY})} < \bar{\alpha} < \frac{\bar{\mu}^2}{4(\bar{K} + D_{XX})}$
- $\frac{\bar{v}^2}{4(\bar{K} + D_{YY})} = 2.45 \cdot 10^{-2}$  ,  $\frac{\bar{\mu}^2}{4(\bar{K} + D_{XX})} = 1.97 \cdot 10^{-1}$

- $q_c^2 = \frac{|\bar{\mu}|}{2(\bar{K} + D_{XX})} \rightarrow \lambda_{cx} = 18.04$  (28.33 wavelenghts in the system)
- $\frac{|\bar{v}|}{2(\bar{K} + D_{YY})} \rightarrow \lambda_{cy} = 24.60$  (20.73 wavelenghts in the system)

Supposing a system with the critical wavenumber  $q_c$ , each wavelength would be represented by approximately 9 points in a grid with 256 nodes per mesh side. Although it is not clear from start whether the number of wavelengths in the structure will be near the critical value for the direction  $\vec{l}_X$  or not, we still use  $q_c$  as a guide when defining the grid spacing (together with the stability tests).

### 4.3 Simulation results

#### 4.3.1 [Case 1] Initial pattern with $\vec{q} = q_0 \vec{l}_X$ , 14 wavelengths

For the first simulation, the initial pattern was a monomodal structure with a wavenumber  $q_0 = 1.7181 \cdot 10^{-1}$  in the  $\vec{l}_X$  direction, which is located outside the stable domain. New modes in the  $\vec{l}_X$  direction grow quickly, and the wavelength is split in approximately two, leading to a wavenumber with almost the critical value (the system presents a structure with 27 wavelengths). Figure 13 shows the time evolution of the  $L_1$  norm rate of change, internal iterations, and maximum height modulus  $|\bar{h}_n|$  for this case.

From the  $L_1$  curve, we follow a smooth pattern transition when doubling the number of wavelengths, which happens around  $\tau = 25$ , and gently changing the height values from the initial maximum modulus 0.1 (positive) up to 0.4 (negative). The wave amplitude goes initially from (0;0.1) to (-0.4;0) in the steady state, which is also consistent with the physical phenomenon of surface erosion. The internal iterations reach a maximum of six during the initial time steps and keep falling as the steady state gets closer, attaining a minimum value of two iterations for each time step.

The pattern time evolution is shown from Figure 14 up to Figure 18. For each state, the Fast Fourier Transform (FFT) is also displayed, in order to comprehend the dynamics in terms of the modes. Here, we can observe the growth of new harmonics and the decay of the initial one, while maintaining the 1D structure. Even though the  $L_1$  decay may suggest that the steady state was reached, we later questioned if hexagonal modes would emerge in case the simulation continued. In fact, the 1D pattern obtained is stationary, since the continuation of this test led to  $L_1$  values well bellow  $10^{-7}$ , without changing the structure.

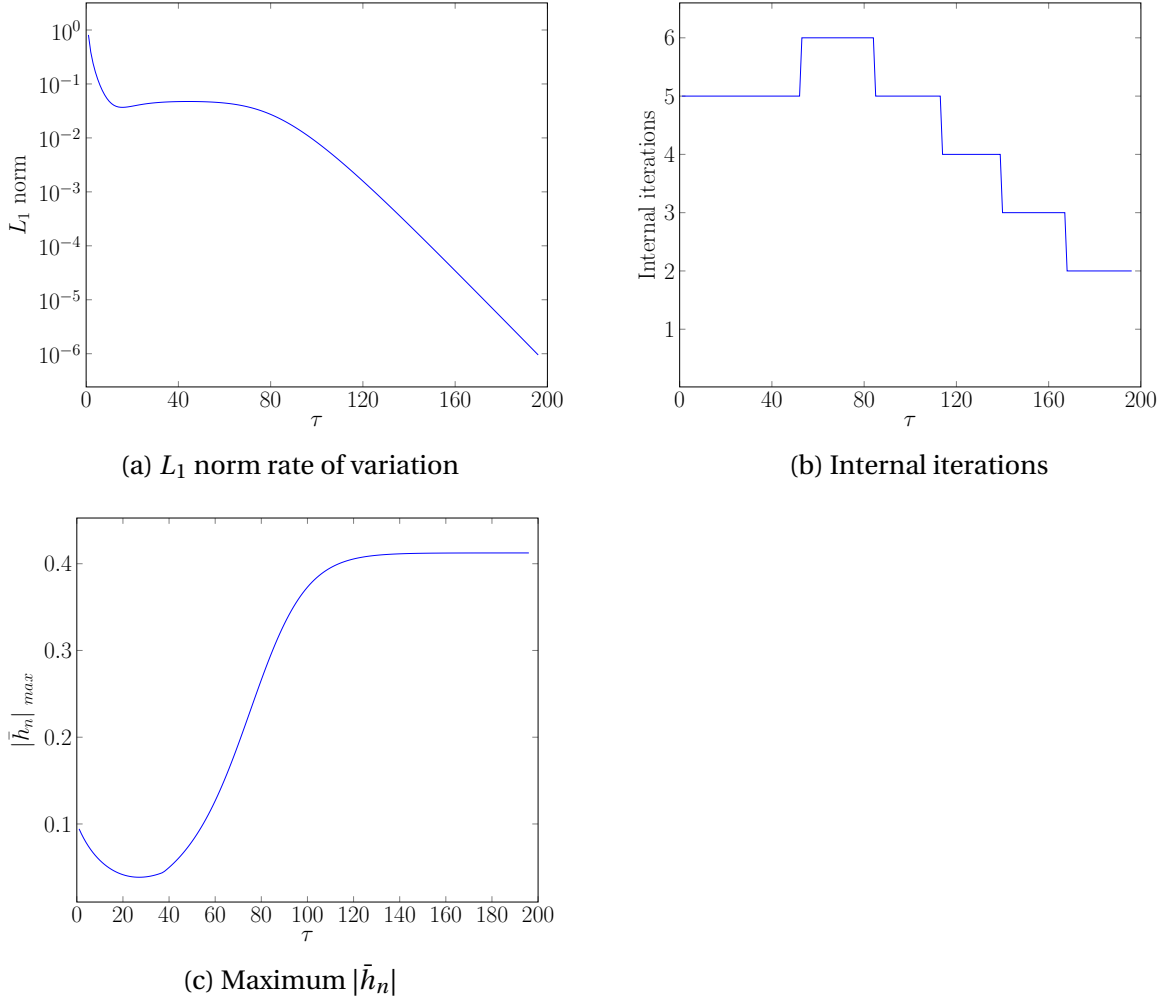


Figure 13:  $L_1$  norm, internal iterations and maximum values for  $\bar{h}_n$  as a function of time  $\tau$ , for an initial pattern with  $\vec{q} = q_0 \vec{1}_X$  (outside the stable domain),  $\Delta\tau = 0.1$ ,  $\Delta X = \Delta Y = 2$ , on a  $256 \times 256$  nodes domain.

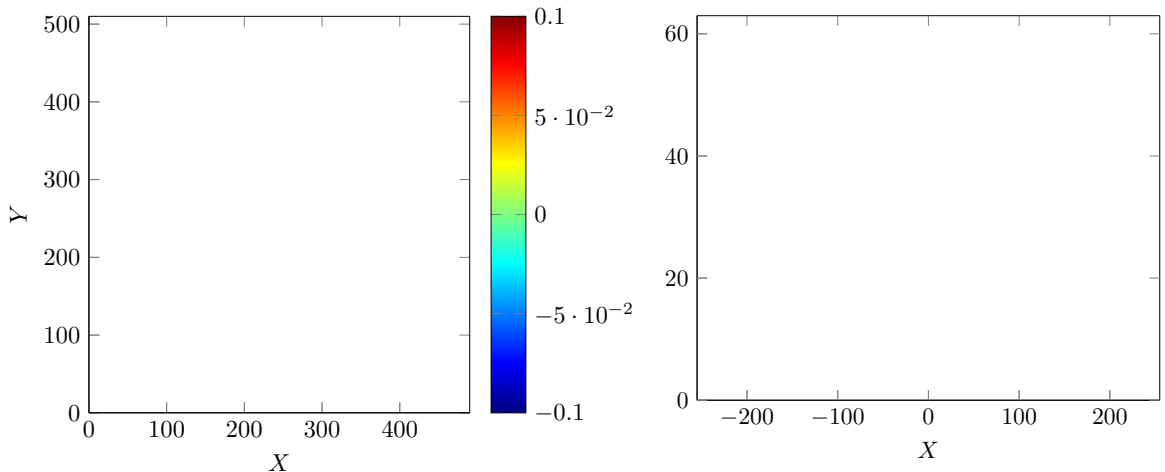


Figure 14: Surface height values  $\bar{h}_n$  and their respective Fourier Transform for  $\tau = 0$  (initial monomodal pattern with  $\vec{q} = q_0 \vec{1}_X$ ).

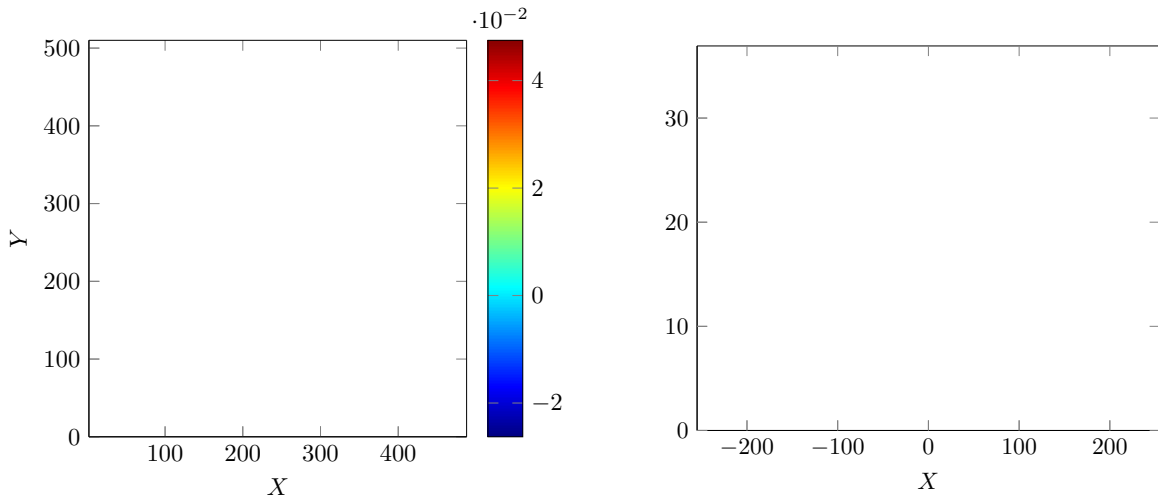


Figure 15: Surface height values  $\bar{h}_n$  and their respective Fourier Transform for  $\tau = 15$ .

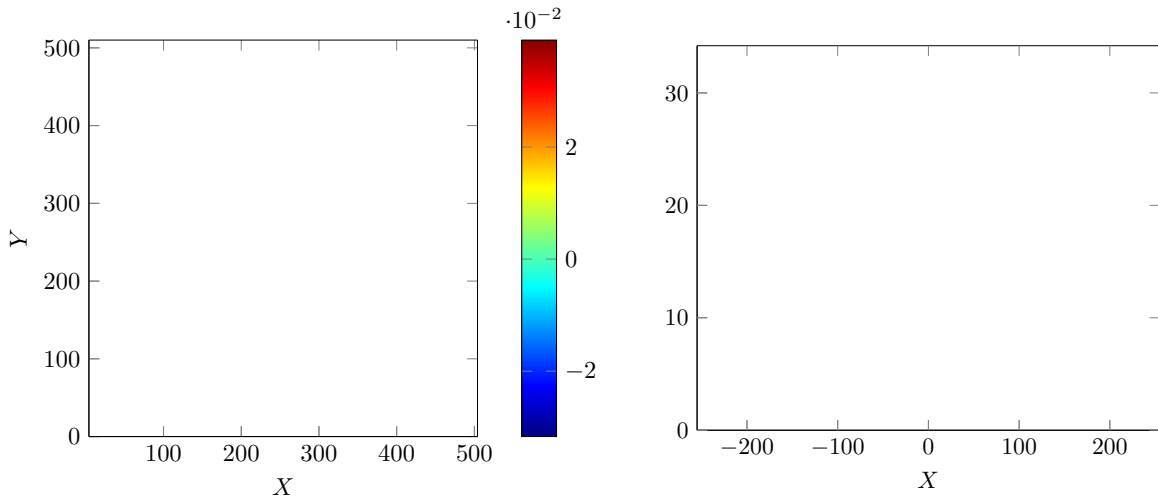


Figure 16: Surface height values  $\bar{h}_n$  and their respective Fourier Transform for  $\tau = 30$ .

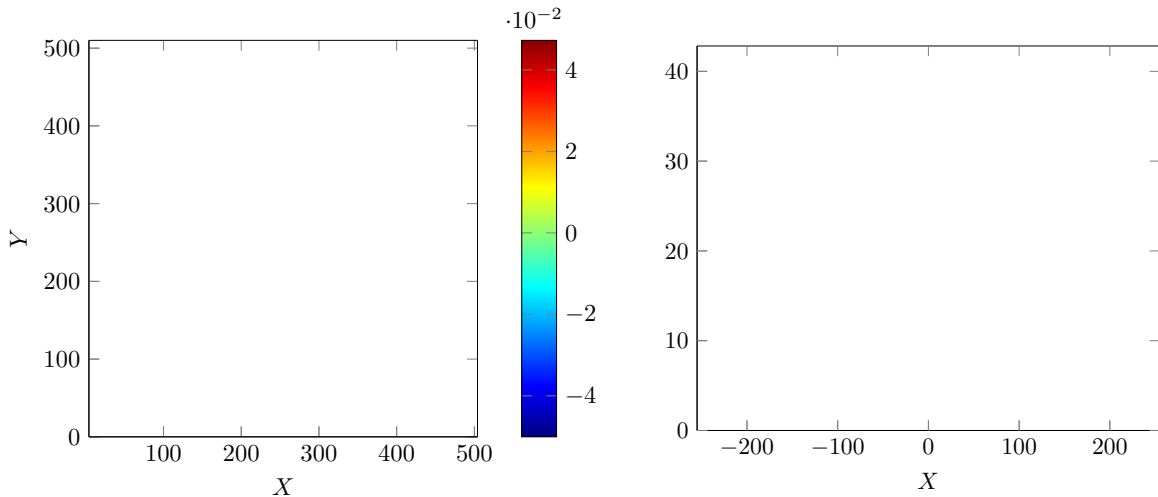


Figure 17: Surface height values  $\bar{h}_n$  and their respective Fourier Transform for  $\tau = 40$ .

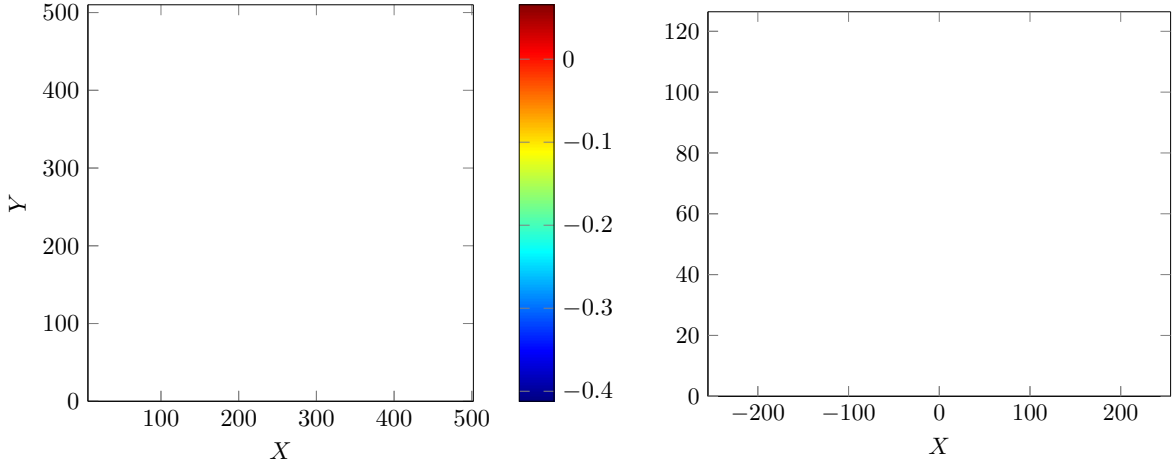


Figure 18: Surface height values  $\bar{h}_n$  and their respective Fourier Transform for  $\tau = 150$ . Each wavelength from the initial pattern was approximately split in two with the decay and growth of new harmonics. The steady state maintains the 1D structure.

#### 4.3.2 [Case 2] Initial pattern with $\vec{q} = q_0 \vec{1}_X$ , 2 wavelengths

This time, the initial pattern consists of a 1D structure with a wavenumber  $q_0 = 2.4544 \cdot 10^{-2}$  in the  $\vec{1}_X$  direction, situated inside the stable domain. Figure 19 presents the time evolution of the  $L_1$  norm, internal iterations, and maximum height modulus  $|\bar{h}_n|$  for this case, with a zoom into the initial regimes to display how the structure diminishes and rises. The initial behavior corresponds to the linearly stable solution, when  $\sigma_T < 0$  and the nonlinear effects are still not significant.

From Figure 20 to Figure 25 we can observe the transition from the initial pattern up to the stationary state, alongside the FFT for the central part of the domain. The pattern maintains its 1D initial morphology until  $\tau = 150$ , while exponentially reducing its amplitude. Then, the structure destabilizes, generating a 1D pattern with a wavenumber near  $q_c$ , just as Case 1. However, this is only a transitory state: around  $\tau = 700$ , we can clearly see the emergence of hexagonal modes by the ascension of  $|\bar{h}_n|$ . From this moment on, a nanohole pattern is structured, removing the majority of its defects up to  $\tau = 40,000$ . After this point, a well ordered hexagonal pattern is obtained, but some defects remain slowly moving around the structure, and the system is unable to remove them, as shown by Figure 25.

This result is also physically consistent with the sputtering phenomenon, as the height decay is expected from the removal of surface atoms, alongside the rearrangement of the surface morphology. Besides, nanohole formation is one of the organized patterns achieved by ion beam sputtering, as discussed in Chapter 1.

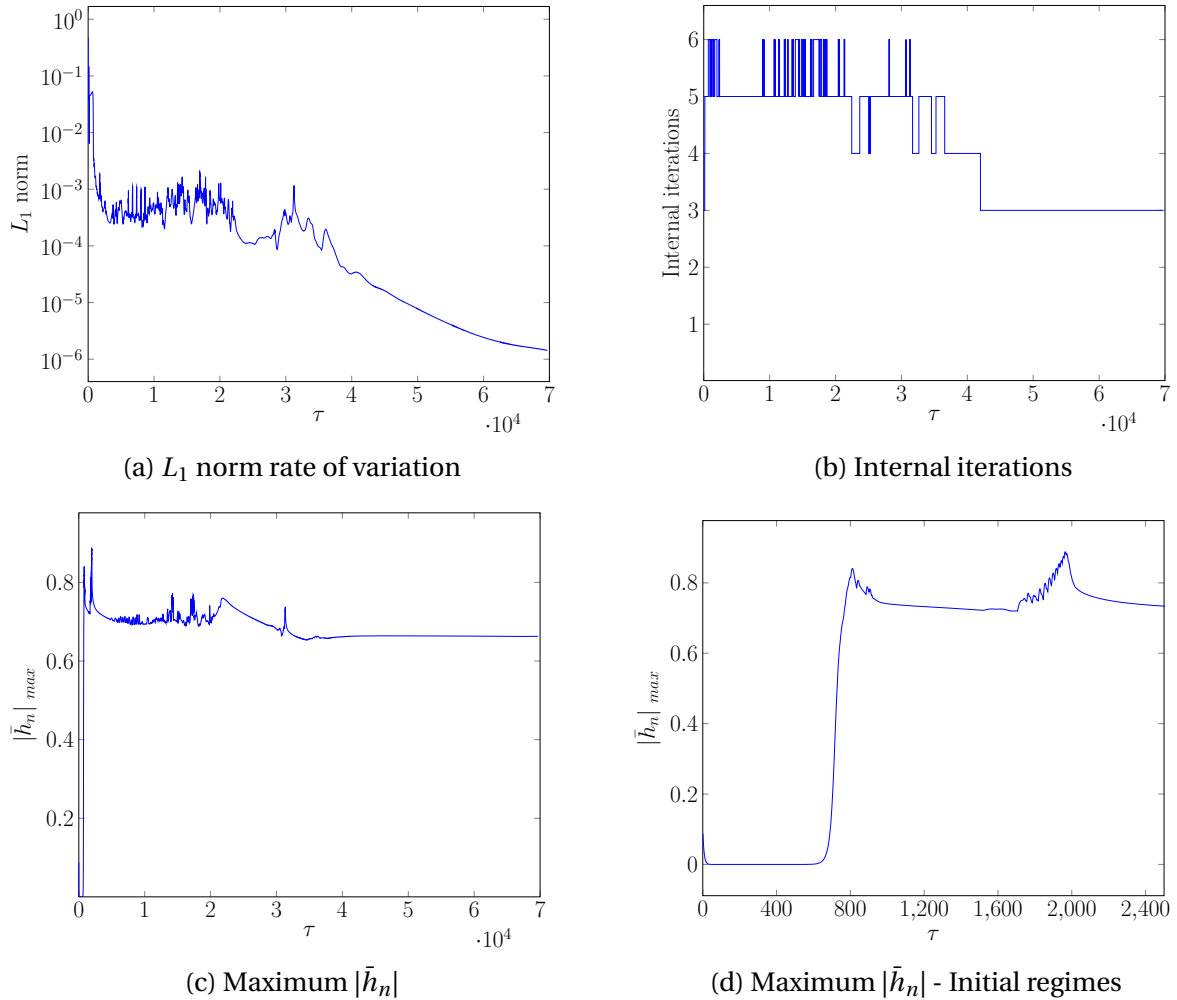


Figure 19:  $L_1$  norm, internal iterations and maximum values for  $\bar{h}_n$  as a function of time  $\tau$ , for an initial pattern with  $\vec{q} = q_0 \vec{1}_X$  (inside the stable domain),  $\Delta\tau = 0.1$ ,  $\Delta X = \Delta Y = 2$ , on a  $256 \times 256$  nodes domain.

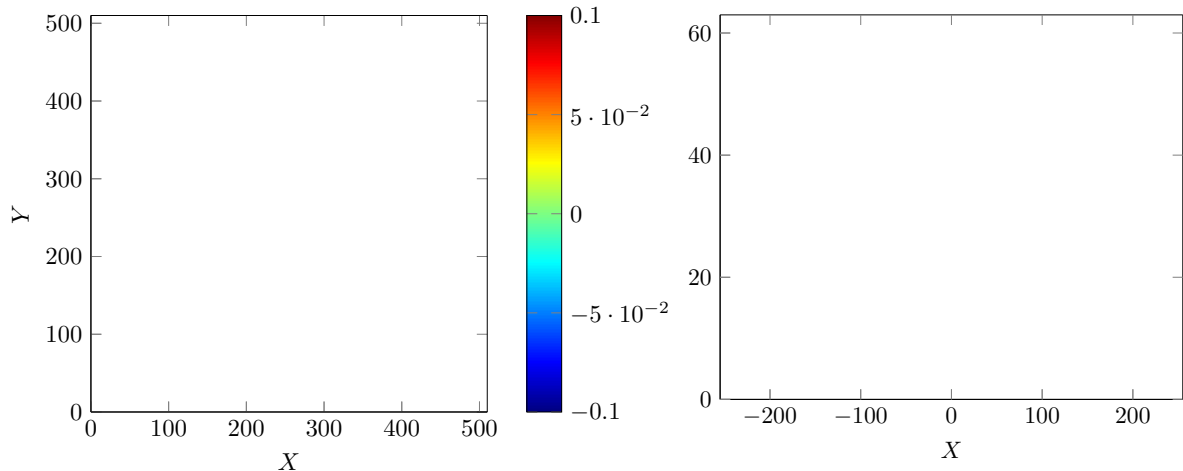


Figure 20: Surface height values  $\bar{h}_n$  and their respective Fourier Transform for  $\tau = 0$  (initial monomodal pattern with  $\vec{q} = q_0 \vec{1}_X$ ).

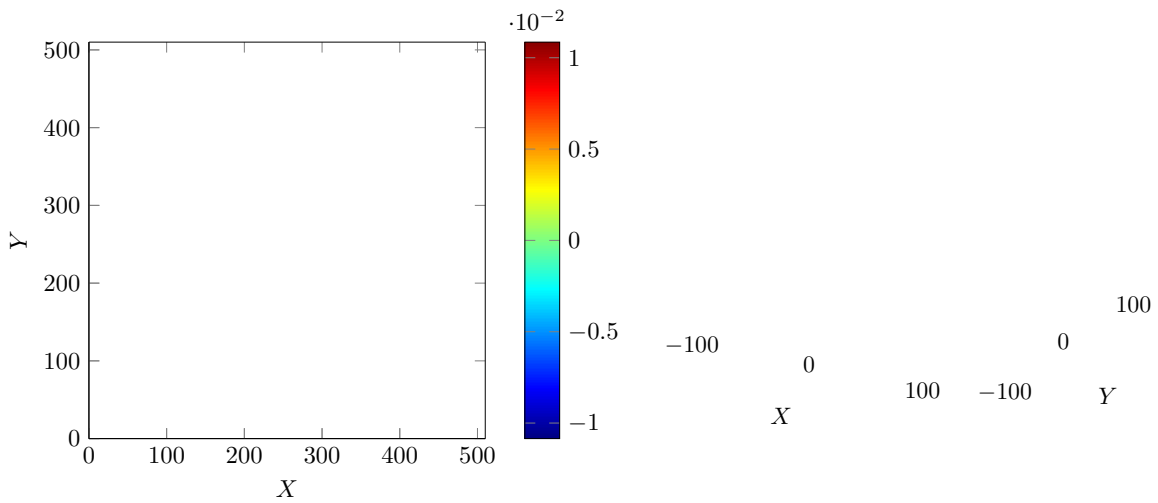


Figure 21: Surface height values  $\bar{h}_n$  and their respective Fourier Transform for  $\tau = 15$ .

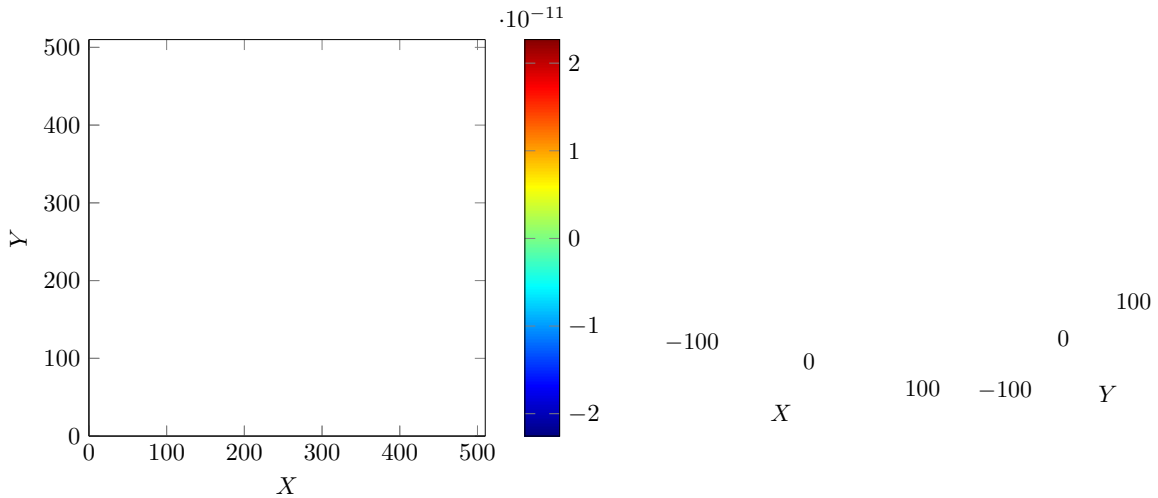


Figure 22: Surface height values  $\bar{h}_n$  and their respective Fourier Transform for  $\tau = 150$ .

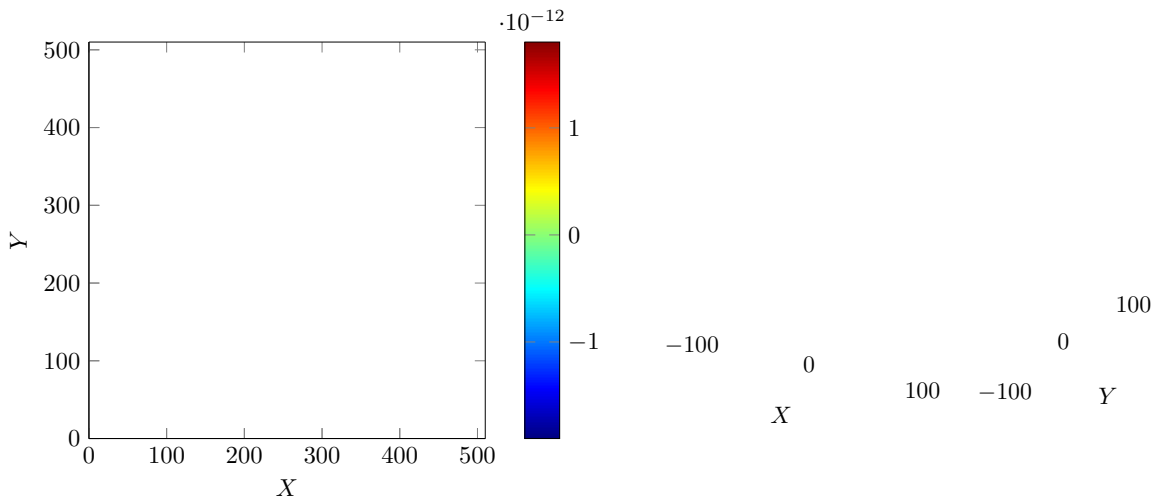


Figure 23: Surface height values  $\bar{h}_n$  and their respective Fourier Transform for  $\tau = 200$ .

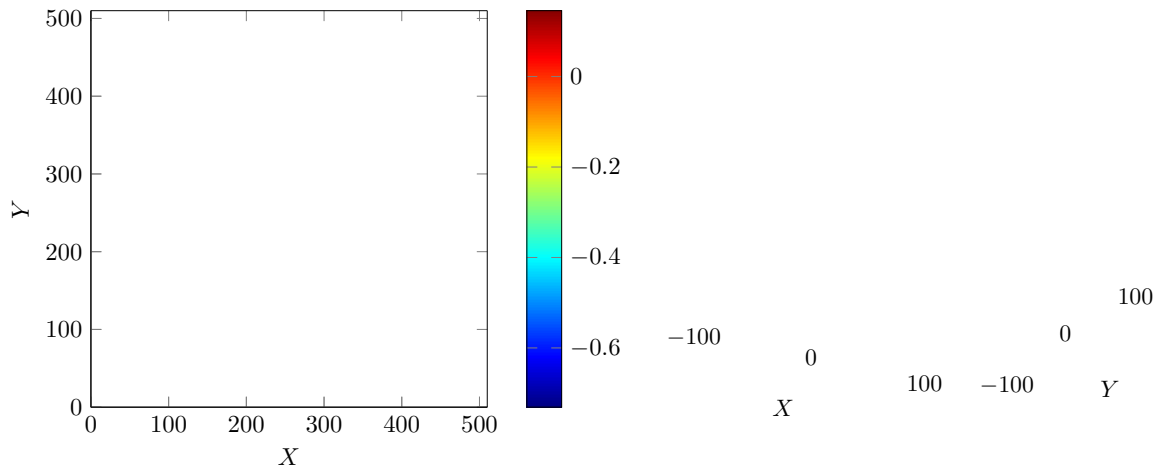


Figure 24: Surface height values  $\bar{h}_n$  and their respective Fourier Transform for  $\tau = 1250$ .

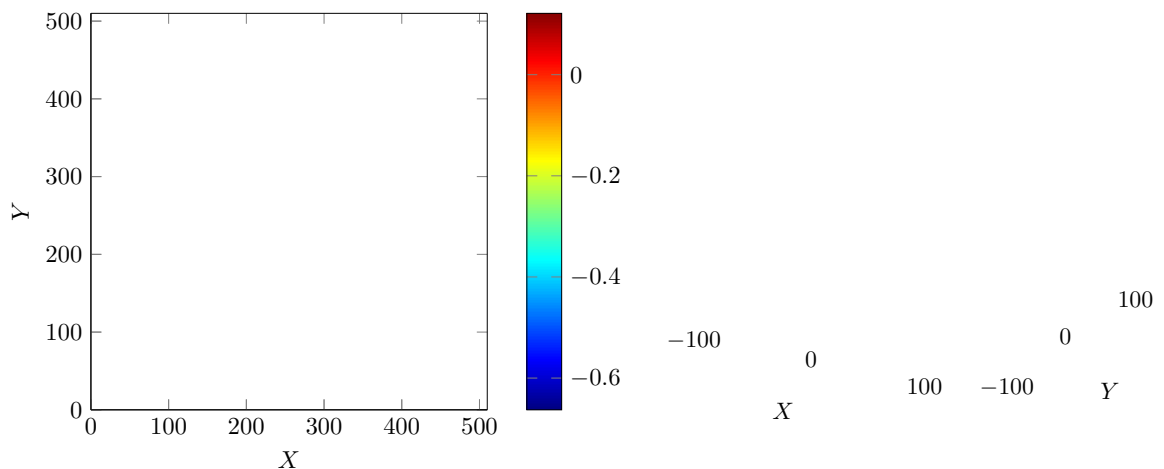


Figure 25: Surface height values  $\bar{h}_n$  and their respective Fourier Transform for  $\tau = 70000$ . A well ordered nanohole pattern is obtained, but some defects remain in the structure, slowly and continuously moving in time.

### 4.3.3 [Case 3] Initial pattern with $\vec{q} = q_0 \vec{1}_Y$ , 2 wavelengths

The initial pattern for the present case is a monomodal  $\vec{1}_Y$  surface, possessing the same number of wavelengths as Case 2 for the sake of comparison ( $q_0 = 2.4544 \cdot 10^{-2}$ ). This wavenumber also lies in the linearly stable domain, so we expect a similar behavior of the dynamics during the first stage. Figure 26 contains the time evolution of the  $L_1$  norm, internal iterations, and maximum height modulus  $|\bar{h}_n|$  for the third simulation; these results are similar to the ones obtained in Case 2. If we zoomed in the initial regimes, it would be possible to see the 1D structure diminishing in height before the emergence of hexagonal modes.

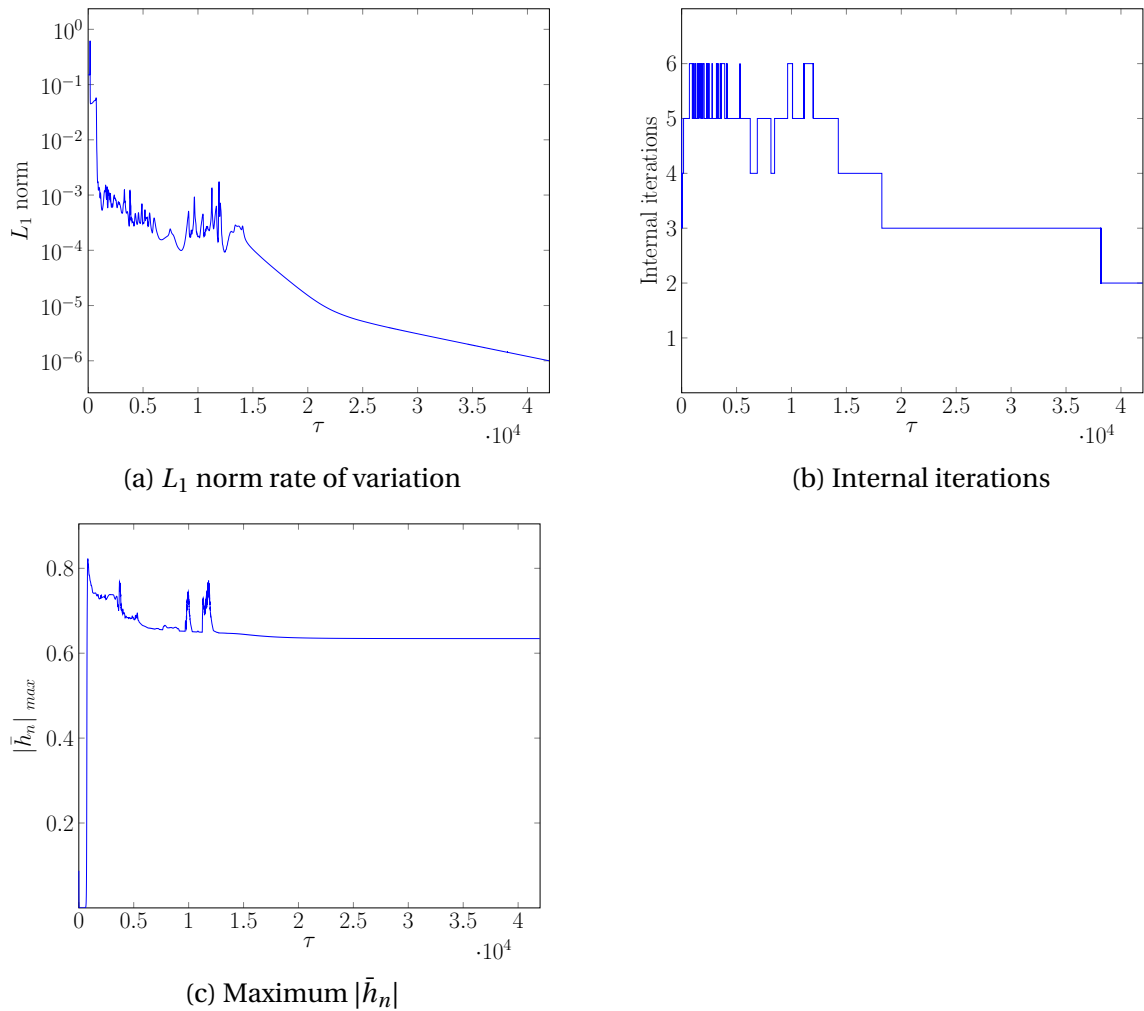


Figure 26:  $L_1$  norm, internal iterations and maximum values for  $\bar{h}_n$  as a function of time  $\tau$ , for an initial pattern with  $\vec{q} = q_0 \vec{1}_Y$  (inside the stable domain),  $\Delta\tau = 0.1$ ,  $\Delta X = \Delta Y = 2$ , on a  $256 \times 256$  nodes domain.

From Figure 27 to Figure 32 it is possible to follow the hexagonal modes taking over the system from the 1D initial  $\vec{l}_Y$  structure up to the steady state. However, Case 3 does not display the formation of a 1D pattern with  $\vec{q} \sim q_c \vec{l}_X$ , as in Case 2. Between  $\tau = 150$  and 200, the monomodal  $\vec{l}_Y$  direction surface disappears, and new ripples start to proliferate in the domain. Figure 30 shows that these ripples quickly lose their orientation towards  $\vec{l}_X$ , and in Figure 31 we already have the formation of nanoholes. The steady state (Figure 32) consists of a well ordered defectless nanohole pattern. Therefore, the system was able to rearrange itself and remove all the defects, which was not possible for Case 2.

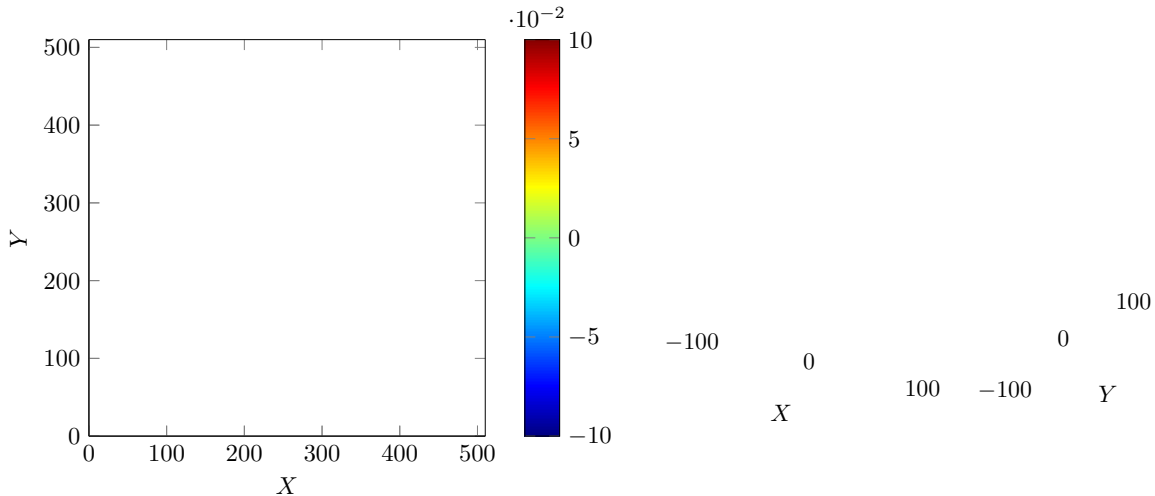


Figure 27: Surface height values  $\bar{h}_n$  and their respective Fourier Transform for  $\tau = 0$  (initial monomodal pattern with  $\vec{q} = q_o \vec{l}_Y$ ).

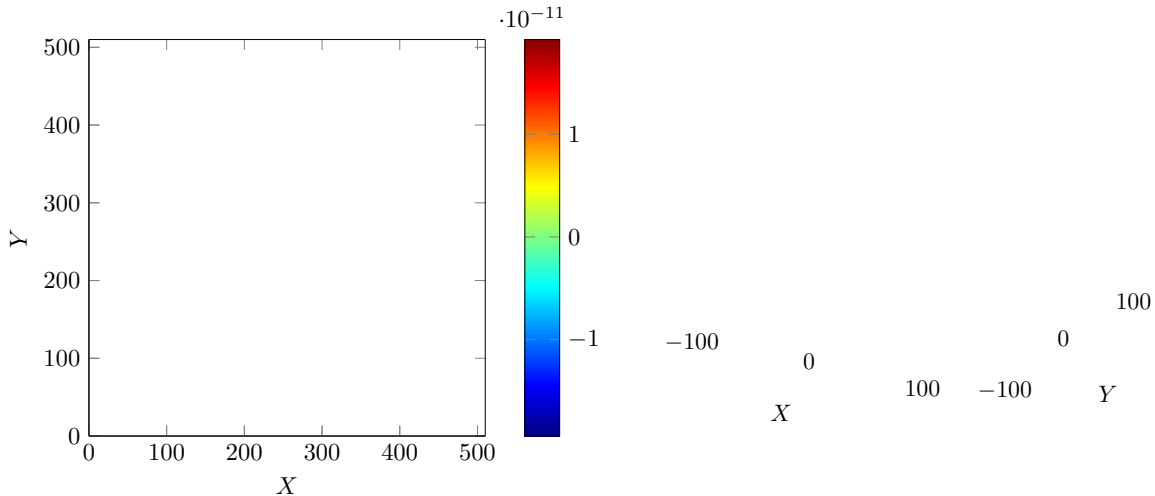


Figure 28: Surface height values  $\bar{h}_n$  and their respective Fourier Transform for  $\tau = 150$ .

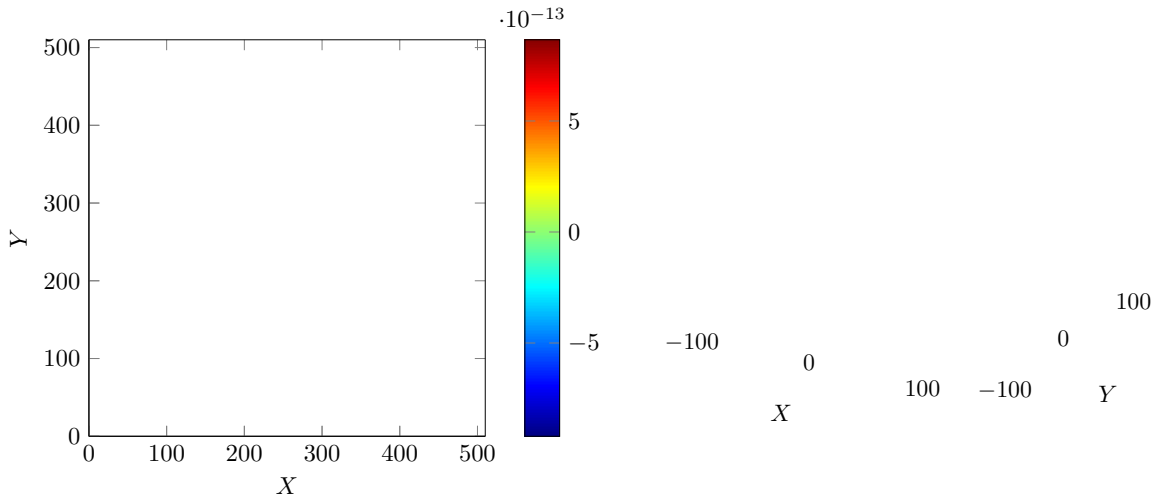


Figure 29: Surface height values  $\bar{h}_n$  and their respective Fourier Transform for  $\tau = 200$ .

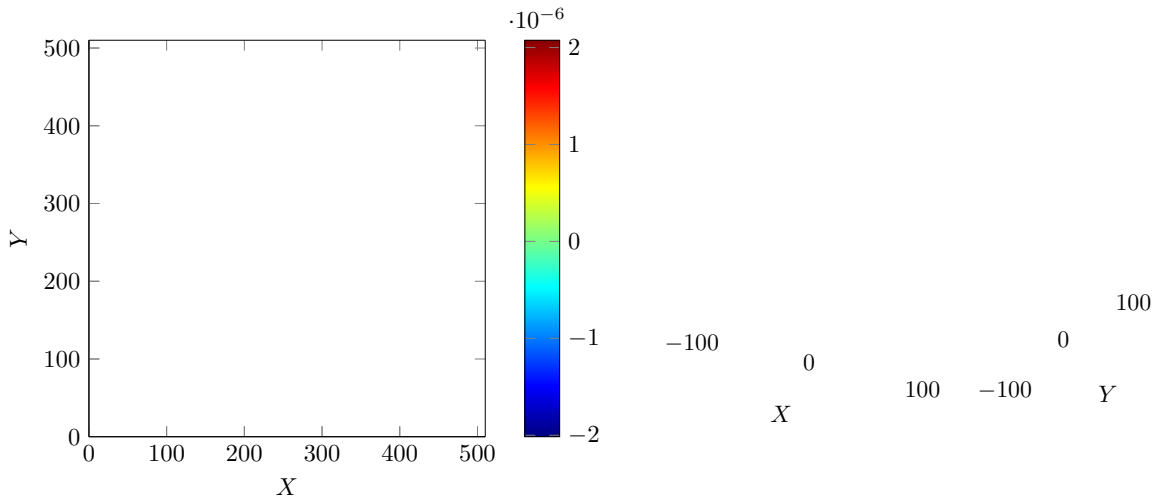


Figure 30: Surface height values  $\bar{h}_n$  and their respective Fourier Transform for  $\tau = 500$ .

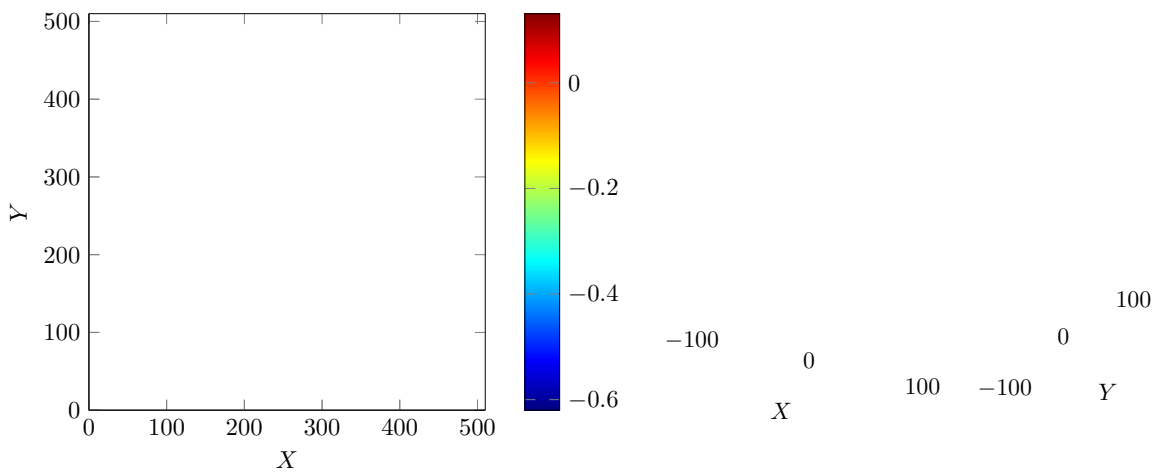


Figure 31: Surface height values  $\bar{h}_n$  and their respective Fourier Transform for  $\tau = 750$ .

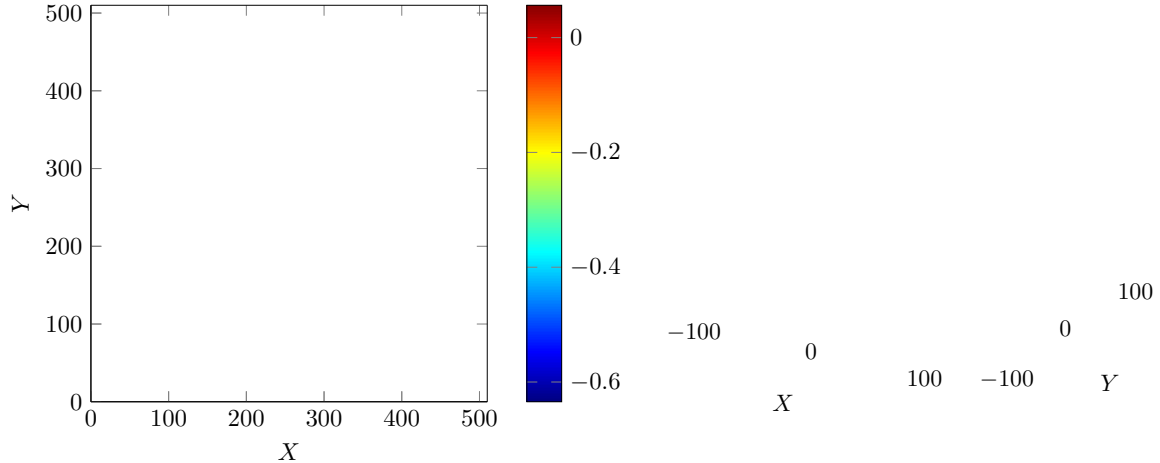


Figure 32: Surface height values  $\bar{h}_n$  and their respective Fourier Transform for  $\tau = 40000$ . A nanohole defectless pattern is obtained in the steady state.

#### 4.3.4 [Case 4] Initial pattern with $\vec{q} = q_0 \vec{1}_Y$ , 21 wavelengths

The fourth simulation was also made on a monomodal  $\vec{1}_Y$  preexisting pattern, but it contained 21 wavelengths in the domain ( $q_0 = 2.5771 \cdot 10^{-1}$ ). Since  $\alpha > \frac{\nu^2}{4(\bar{K} + D_{YY})}$ , we remain in the linearly stable domain for this  $\vec{q} = q_0 \vec{1}_Y$  initial morphology. Figure 33 contains the time evolution of the  $L_1$  norm rate of change, internal iterations, and maximum height modulus  $|\bar{h}_n|$  for Case 4. Those results do not present any alarming differences in relation to the last case, besides proving that increasing the wavenumber for  $\vec{1}_Y$  of the start pattern does not interfere significantly in the system dynamics.

Between Figure 34 and Figure 39, the nanostructuring, from the monomodal state, of a defectless hexagonal pattern can be followed. In comparison with Case 3, here we observe that the 1D monomodal pattern stay intact almost up to  $\tau = 200$  Figure 36, when the nanohole pattern clearly commence to take over.

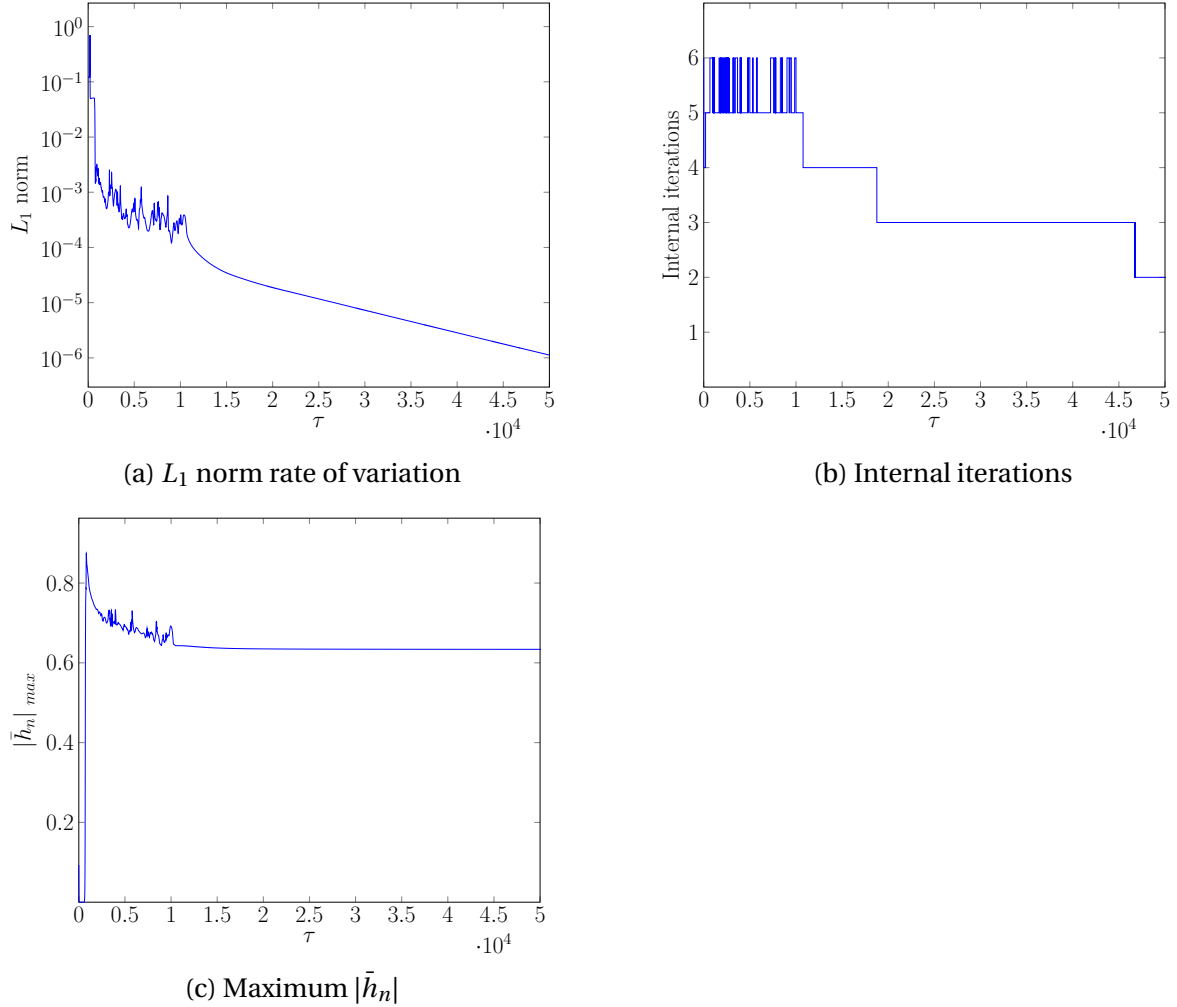


Figure 33:  $L_1$  norm, internal iterations and maximum values for  $\bar{h}_n$  as a function of time  $\tau$ , for an initial pattern with  $\vec{q} = q_0 \vec{1}_Y$  (inside the stable domain),  $\Delta\tau = 0.1$ ,  $\Delta X = \Delta Y = 2$ , on a  $256 \times 256$  nodes domain.

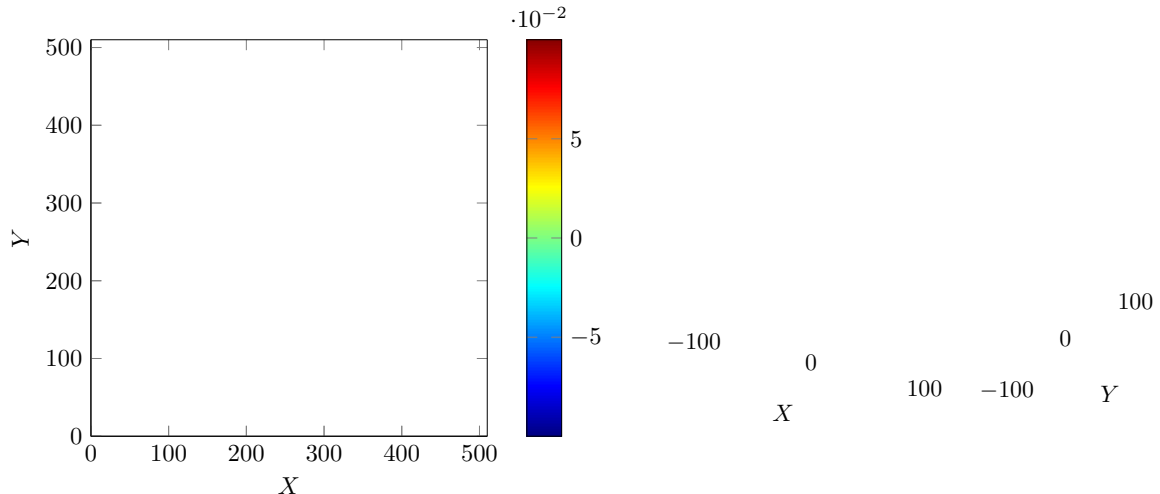


Figure 34: Surface height values  $\bar{h}_n$  and their respective Fourier Transform for  $\tau = 0$  (initial monomodal pattern with  $\vec{q} = q_0 \vec{1}_Y$ ).

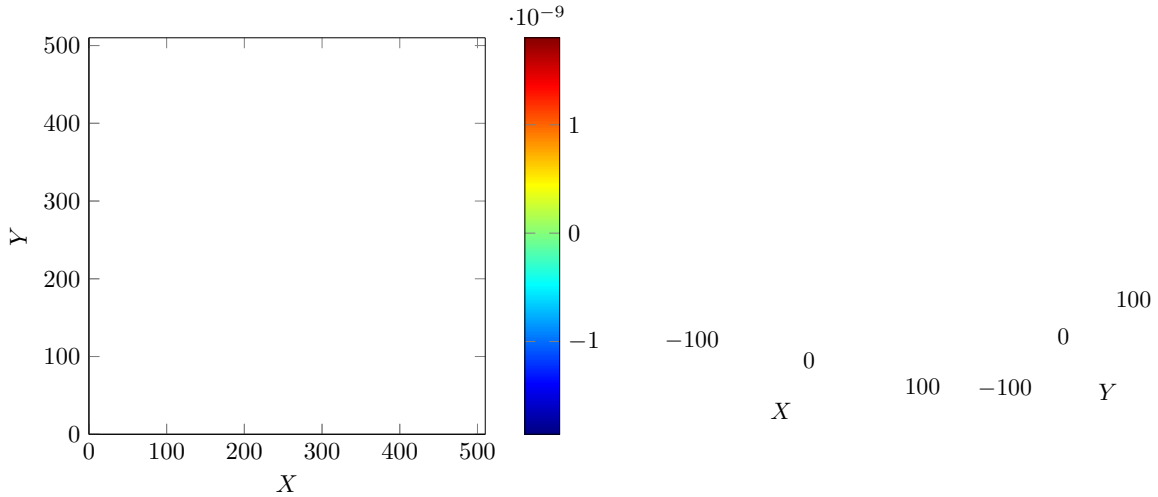


Figure 35: Surface height values  $\bar{h}_n$  and their respective Fourier Transform for  $\tau = 150$ .

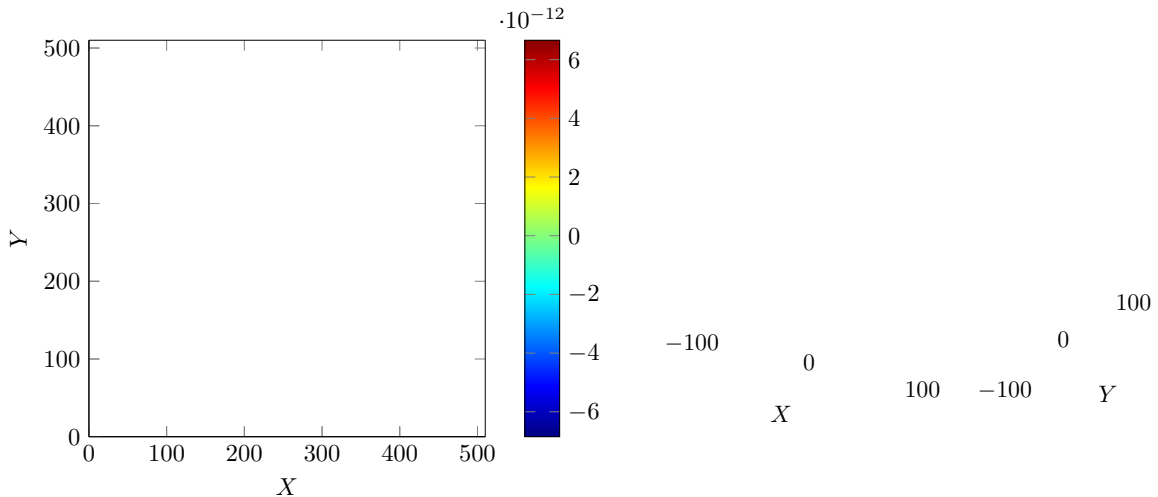


Figure 36: Surface height values  $\bar{h}_n$  and their respective Fourier Transform for  $\tau = 200$ .

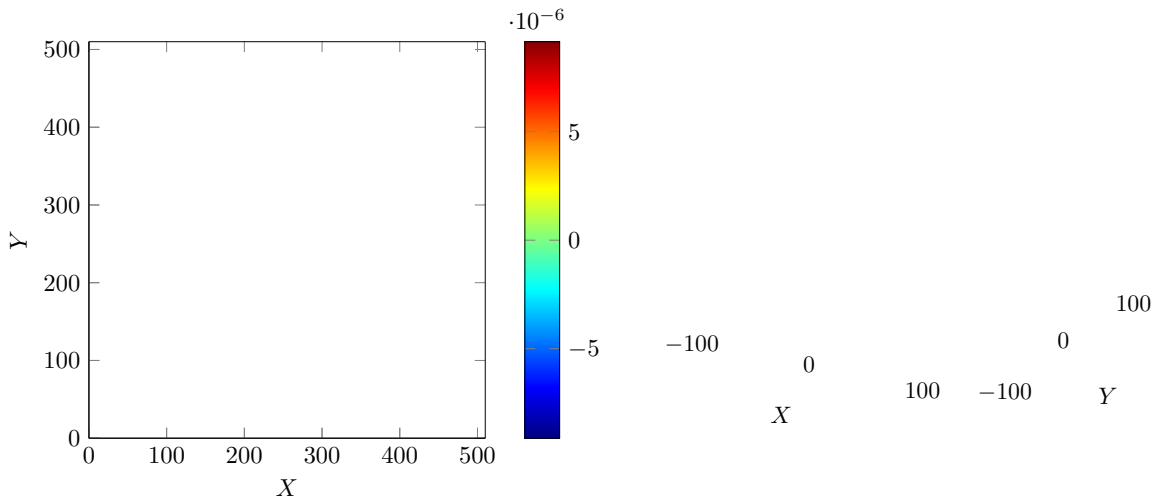


Figure 37: Surface height values  $\bar{h}_n$  and their respective Fourier Transform for  $\tau = 500$ .

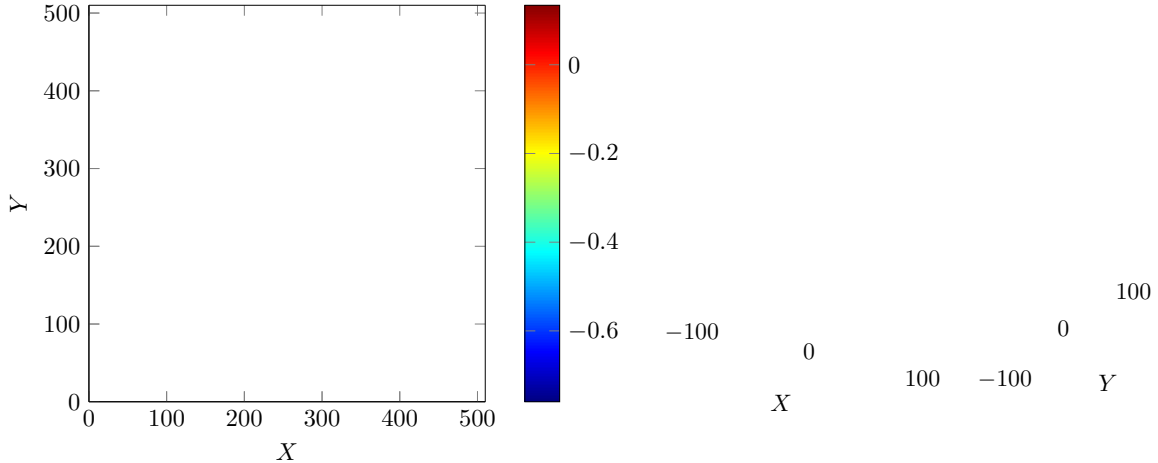


Figure 38: Surface height values  $\bar{h}_n$  and their respective Fourier Transform for  $\tau = 750$ .

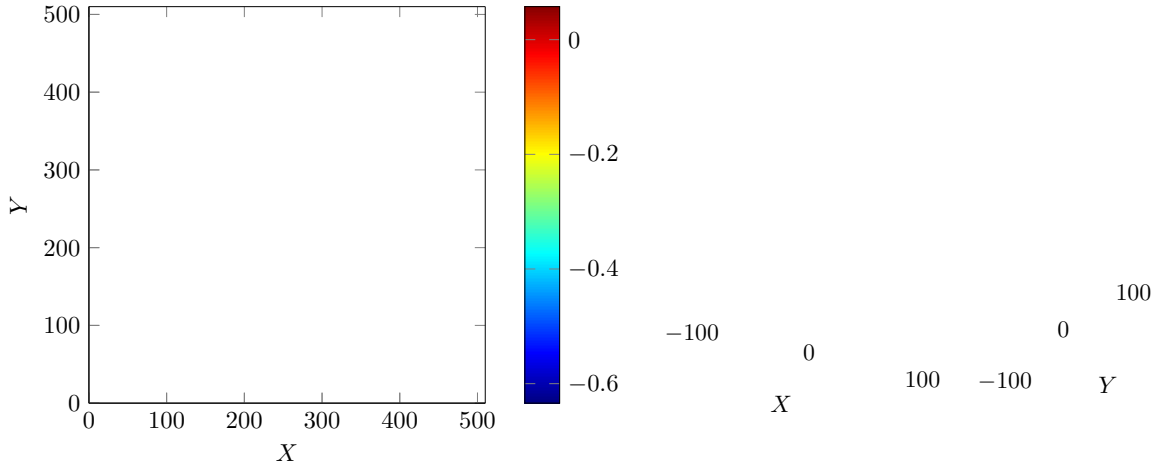


Figure 39: Surface height values  $\bar{h}_n$  and their respective Fourier Transform for  $\tau = 40000$ . A nanohole defectless pattern is obtained in the steady state.

#### 4.3.5 [Case 5] Initial pattern with random values, ranging from 0 to 0.1

A random initial pattern was also studied, aiming to compare the results with those obtained in preexisting monomodal patterns. Figure 40 contains the time evolution of the  $L_1$  norm, internal iterations, and maximum height modulus  $|\bar{h}_n|$  for the random case. It is interesting to have a close look at the initial regimes of the  $L_1$  norm rate of variation: the unpredictability of the nonlinear effects is evident, and it is worth noting how they conduct to the reorganization of the system towards a well ordered structure.

Figure 41 up to Figure 46 illustrate some major changes in the transient structure,

from the initial condition to the steady state pattern formation. A hexagonal 2D weakly anisotropic structure grows rapidly from the random values; however, the defects take longer to be accommodated. From the  $L_1$  norm and the maximum height modulus, it is expected that around  $\tau = 20,000$  the hexagonal structure will be clear of defects, just as the pattern shown by  $\tau = 49,200$ . For each state, the FFT for the central part of the domain is also displayed, in order to observe the growth and arrangements of the modes that lead to the hexagonal pattern. The FFT for Figure 46 is plotted from a top view, displaying the presence of perfect hexagonal modes.

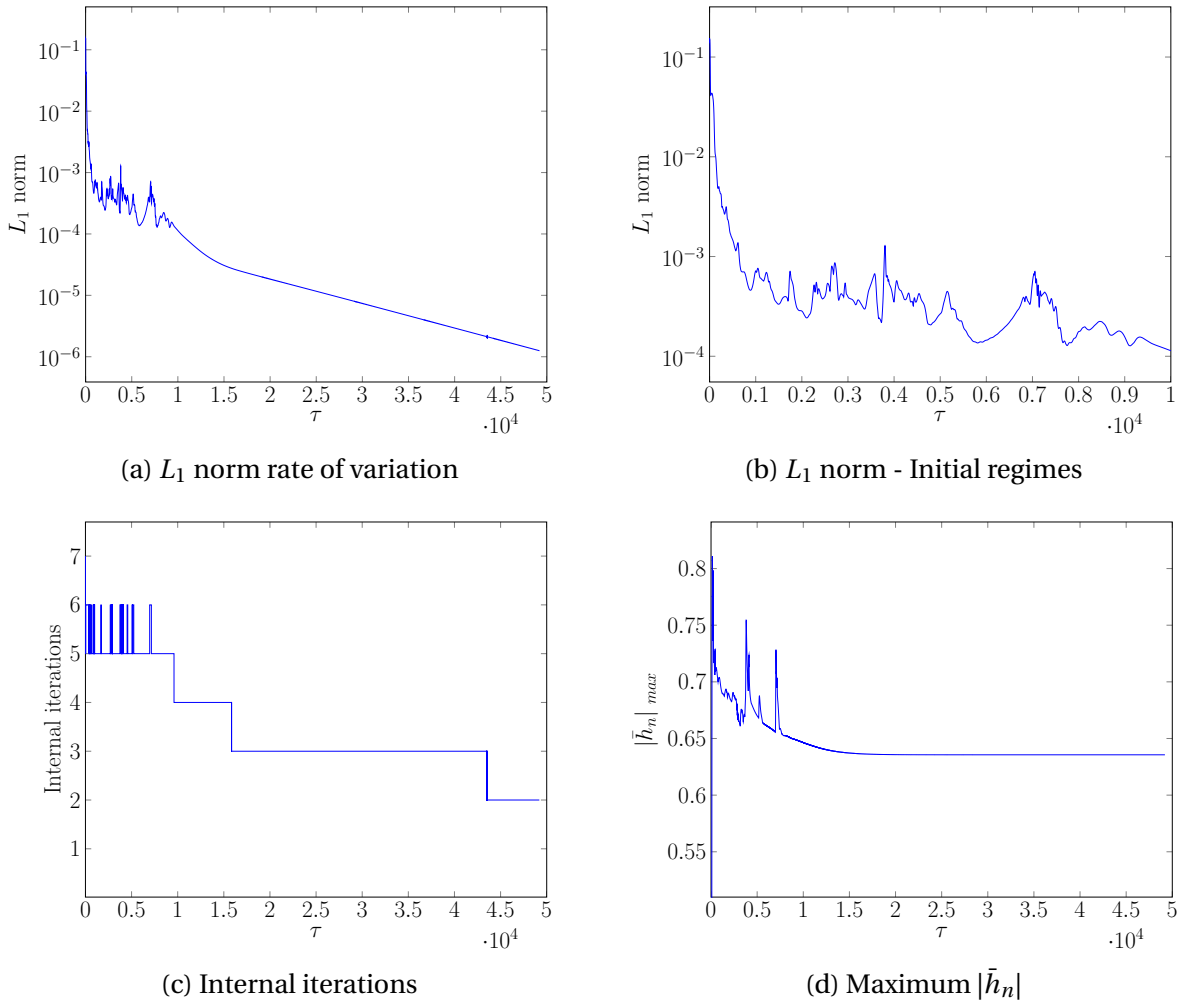


Figure 40:  $L_1$  norm, internal iterations and maximum values for  $\bar{h}_n$  as a function of time  $\tau$ , for a random initial pattern,  $\Delta\tau = 0.1$ ,  $\Delta X = \Delta Y = 2$ , on a  $256 \times 256$  nodes domain.

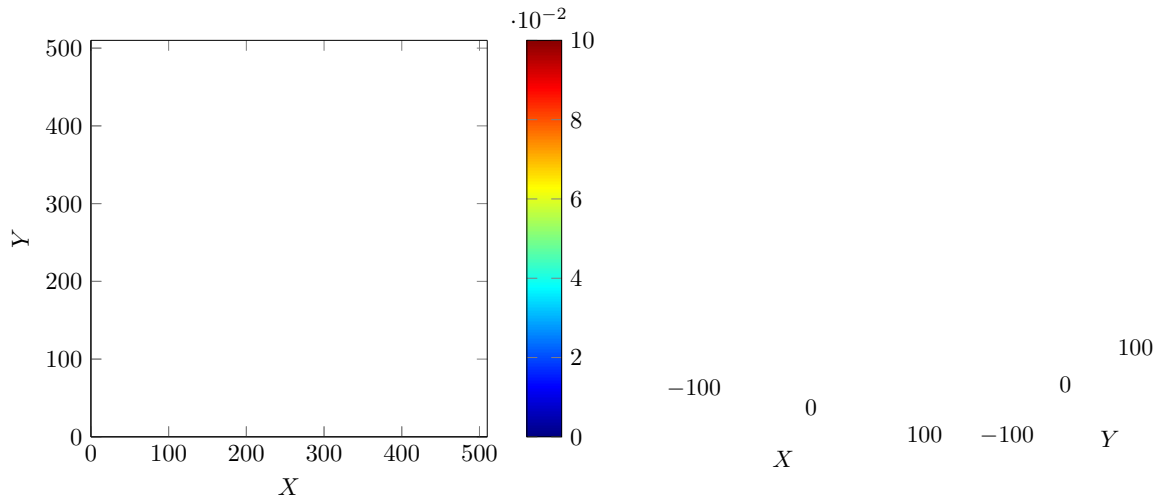


Figure 41: Surface height values  $\bar{h}_n$  and their respective Fourier Transform for  $\tau = 0$  (random initial pattern).

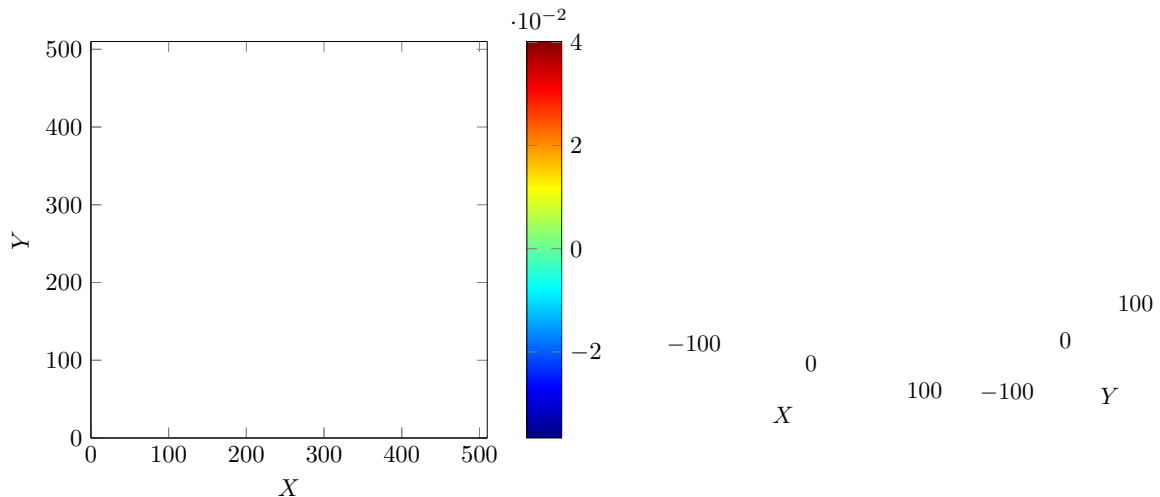


Figure 42: Surface height values  $\bar{h}_n$  and their respective Fourier Transform for  $\tau = 15$ .

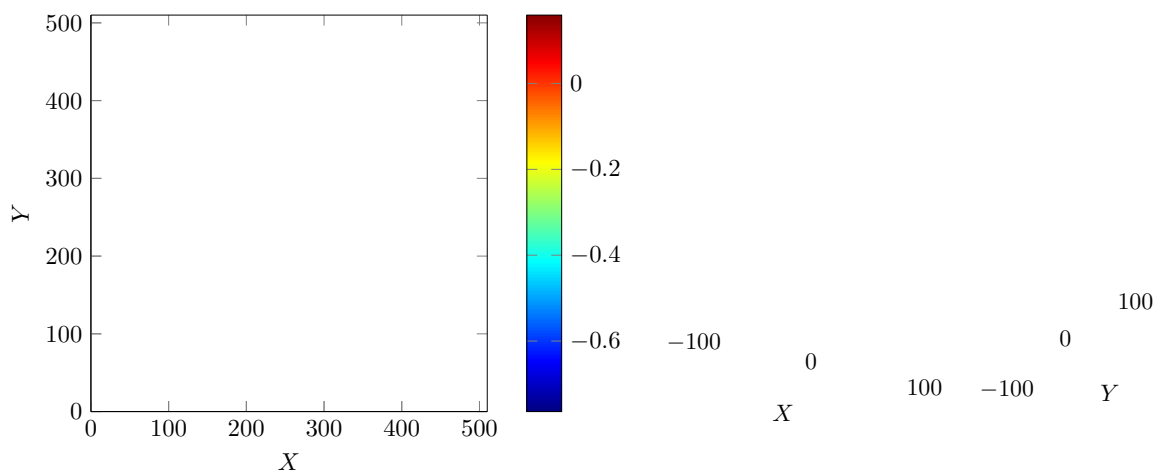


Figure 43: Surface height values  $\bar{h}_n$  and their respective Fourier Transform for  $\tau = 200$ .

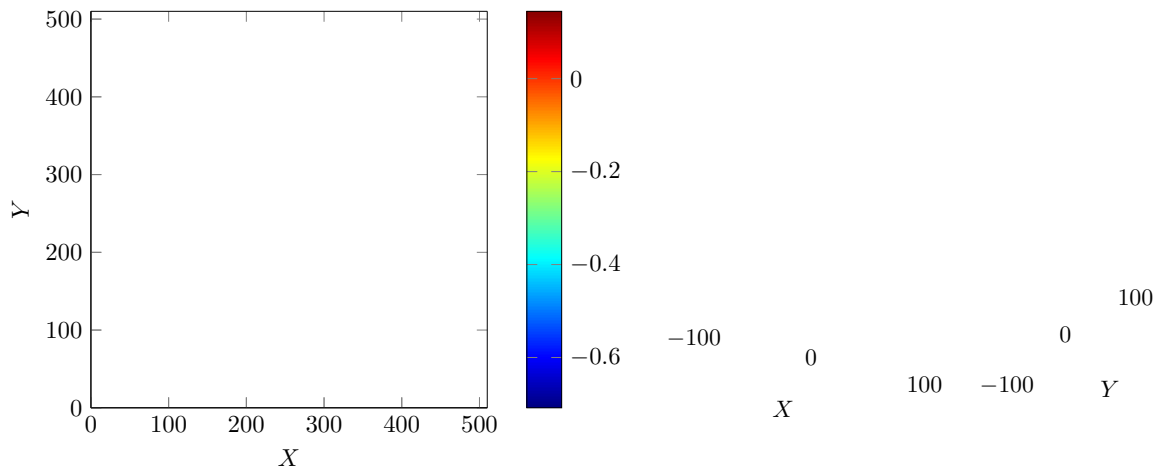


Figure 44: Surface height values  $\bar{h}_n$  and their respective Fourier Transform for  $\tau = 400$ .

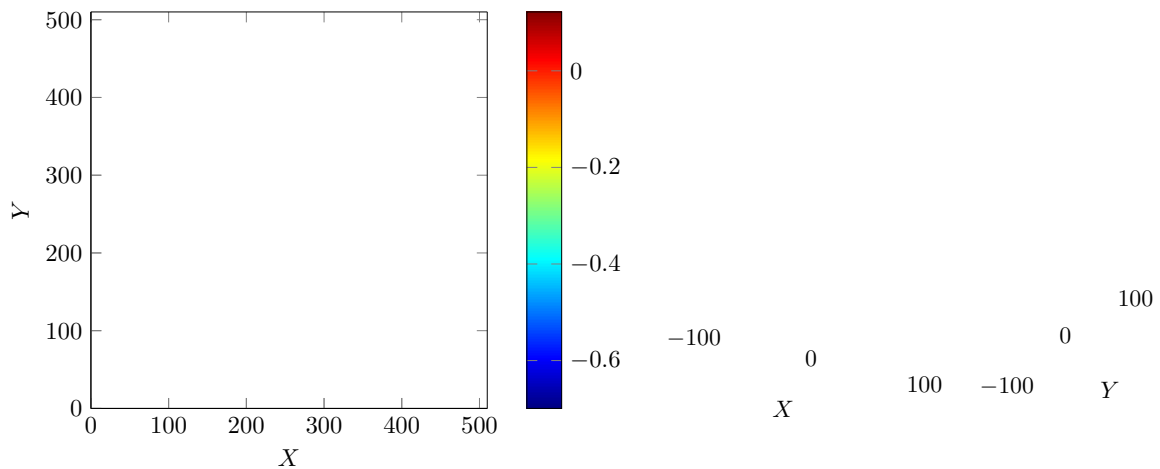


Figure 45: Surface height values  $\bar{h}_n$  and their respective Fourier Transform for  $\tau = 1000$ .

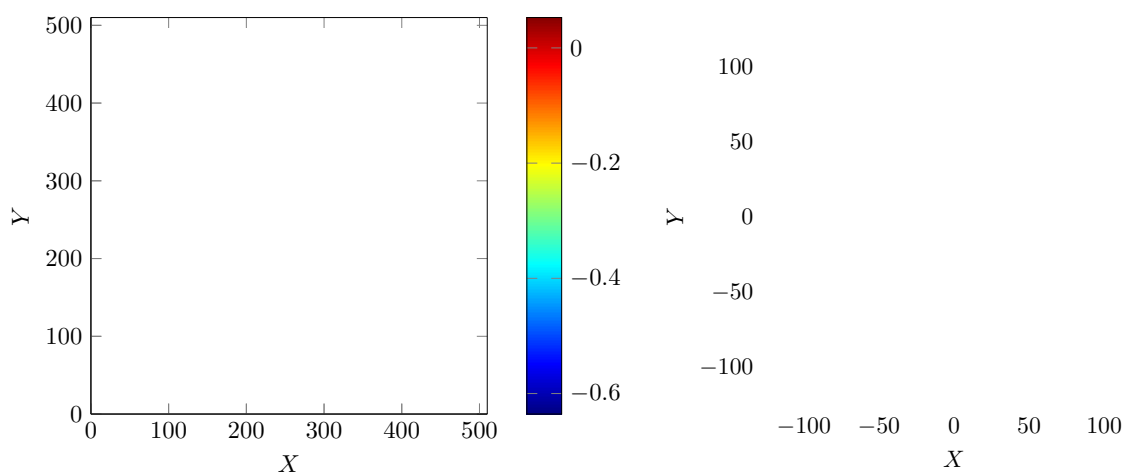


Figure 46: Surface height values  $\bar{h}_n$  and their respective Fourier Transform for  $\tau = 49200$ . A nanohole defectless pattern is obtained in the steady state.

#### 4.3.6 [Case 6] Test: Random initial pattern, discarding the nonlinear contribution

A test case was run eliminating the nonlinear contribution to the anisotropic DKS equation. Here, we turned off the two coefficients related to the nonlinear terms and analyzed the evolution of the system in a random initial pattern. Figure 47 presents the time evolution of the  $L_1$  norm rate of variation, internal iterations, and maximum height modulus  $|\bar{h}_n|$ , and from Figure 48 to Figure 51 we can follow the morphology development. Without the stabilization by nonlinear terms, the height values keep continuously growing and changing with a disorganized nonsteady cellular-like structure. The maximum height modulus presents a exponential behavior in time, which is plotted as linear with the logarithmic  $y - axis$ .

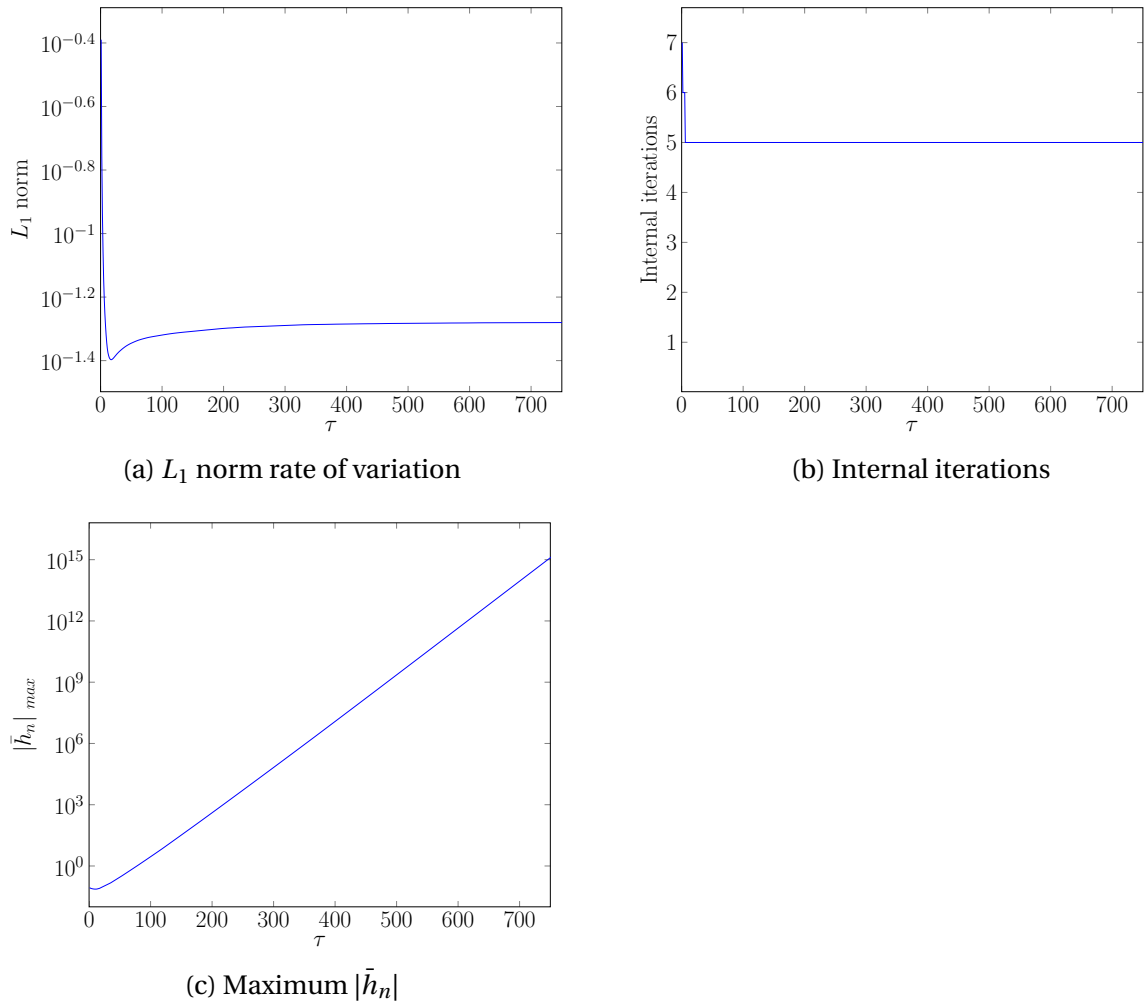


Figure 47:  $L_1$  norm, internal iterations and maximum values for  $\bar{h}_n$  as a function of time  $\tau$ , for a random initial pattern,  $\Delta\tau = 0.1$ ,  $\Delta X = \Delta Y = 2$ , on a  $256 \times 256$  nodes domain. Nonlinear coefficients are discarded.

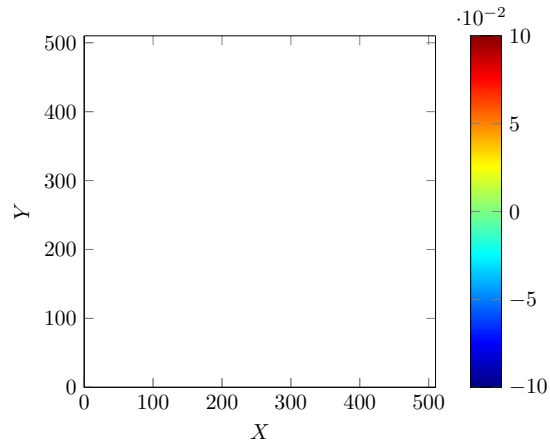


Figure 48: Surface height value  $\bar{h}_n$  for  $\tau = 0$ .

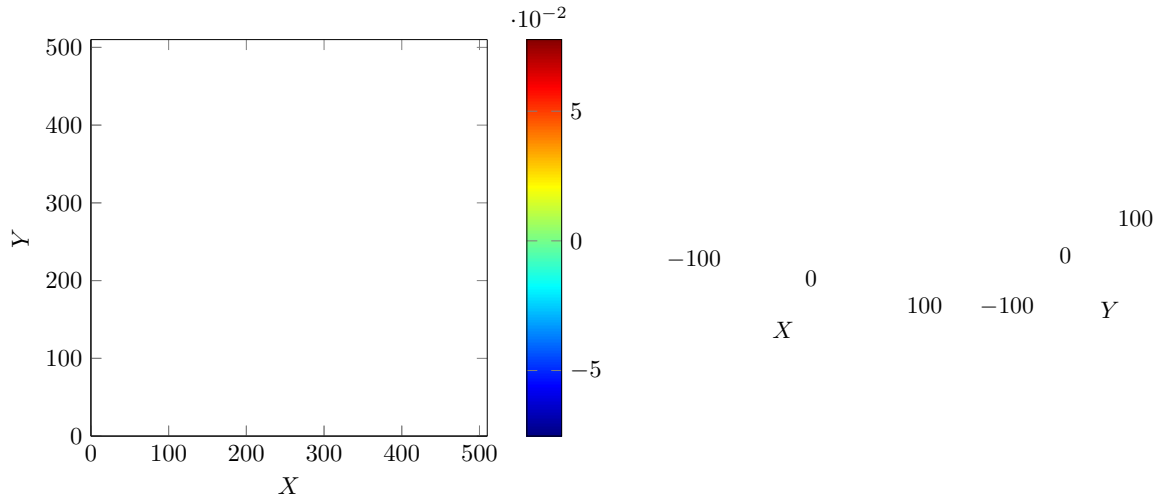


Figure 49: Surface height values  $\bar{h}_n$  and their respective Fourier Transform for  $\tau = 15$ .

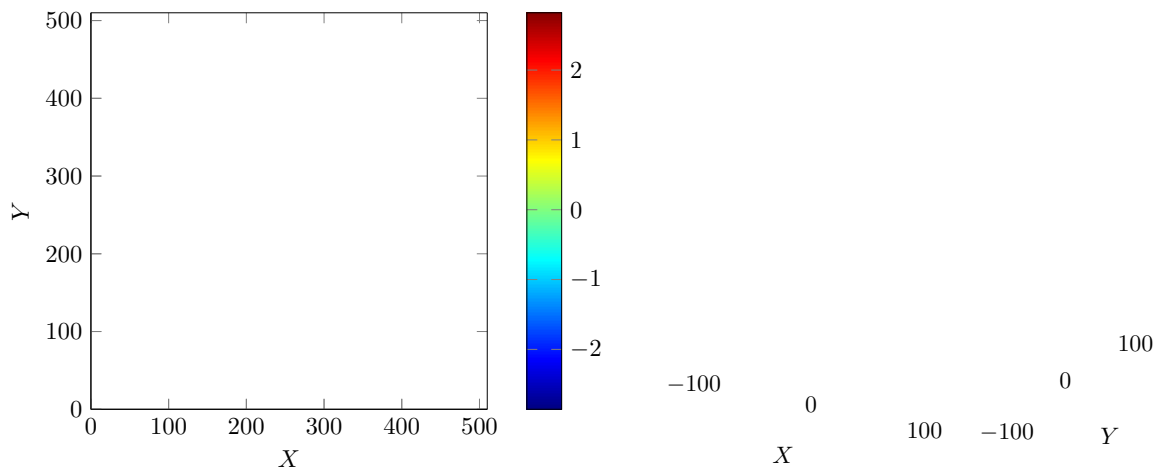


Figure 50: Surface height values  $\bar{h}_n$  and their respective Fourier Transform for  $\tau = 100$ .

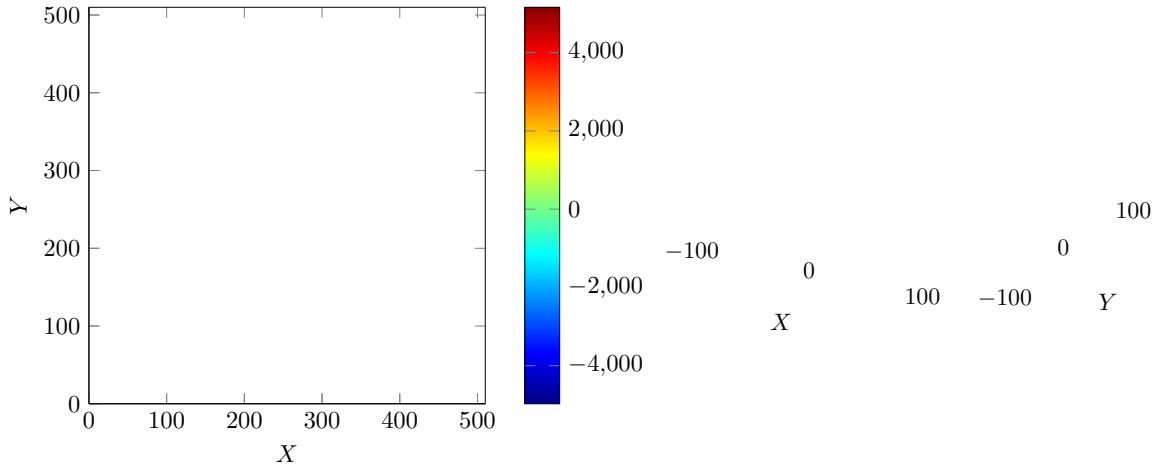


Figure 51: Surface height values  $\tilde{h}_n$  and their respective Fourier Transform for  $\tau = 250$ .

#### 4.3.7 [Case 7] Spatial resolution test, 18 points per critical wavelength:

Initial pattern with  $\vec{q} = q_0 \vec{1}_X$ , 2 wavelengths

The seventh simulation uses the same initial pattern as Case 2, but increases the number of points per critical wavelength to 18 ( $\Delta X = \Delta Y = 1.0$ ). Although the stability tests have not accused the spatial resolution of Case 2 as a potential problem, we insisted in the matter with this final test. Our aim was to study if the remaining defects of Case 2 had any relation to the spatial resolution. Figure 52 contains the usual information about evolution in time of the  $L_1$  norm rate of variation, internal iterations, and maximum height modulus, while between Figure 53 and Figure 58 we have the surface morphology in time, alongside the FFT for each state.

Our first perception was that the spatial resolution really mattered this time, since we got results astonishingly different from Case 2, with a defectless final nanohole pattern. However, this conclusion was a mistake, and it was owing to the initial conditions. Although both cases start with 2 wavelengths with a monomodal  $\vec{1}_X$  pattern, the wavenumber for Case 7 was slightly different than each was in Case 2. Thereafter, we repeated the simulation with  $q_0 = 2.4544 \cdot 10^{-2}$ , just like Case 2, and the exact same results were obtained. The sensibility towards the initial condition is the key to understand such distinct results.

Even though the results of Case 7 are related to an initial pattern with a wavenumber marginally different from Case 2, we still acquired an interesting material to analyze. From  $\tau =$

0 to  $\tau = 400$ , it is possible to follow the nanostructuration of a 1D pattern with a wavenumber near  $q_c$ , as we have seen for Case 1. Based on the  $L_1$  curve and on the maximum height modulus, one could think that a steady state was already reached around  $\tau = 2,000$ , since  $\bar{h}_n$  stabilized in a minimum of -0.42, and the pattern calmed down (see the continuous and pronounced fall of  $L_1$ ). Nonetheless, after  $\tau = 2,000$ , the hexagonal modes emerge, and the 1D structure destabilizes, as seen in Figure 57 for  $\tau = 2,500$ . The  $L_1$  curve rapidly ascends to its peek and then falls down, as the structure reorganizes and stabilizes with the new hexagonal pattern. A defectless nanohole pattern is attained for the steady state, with a minimum height frozen at -0.8.

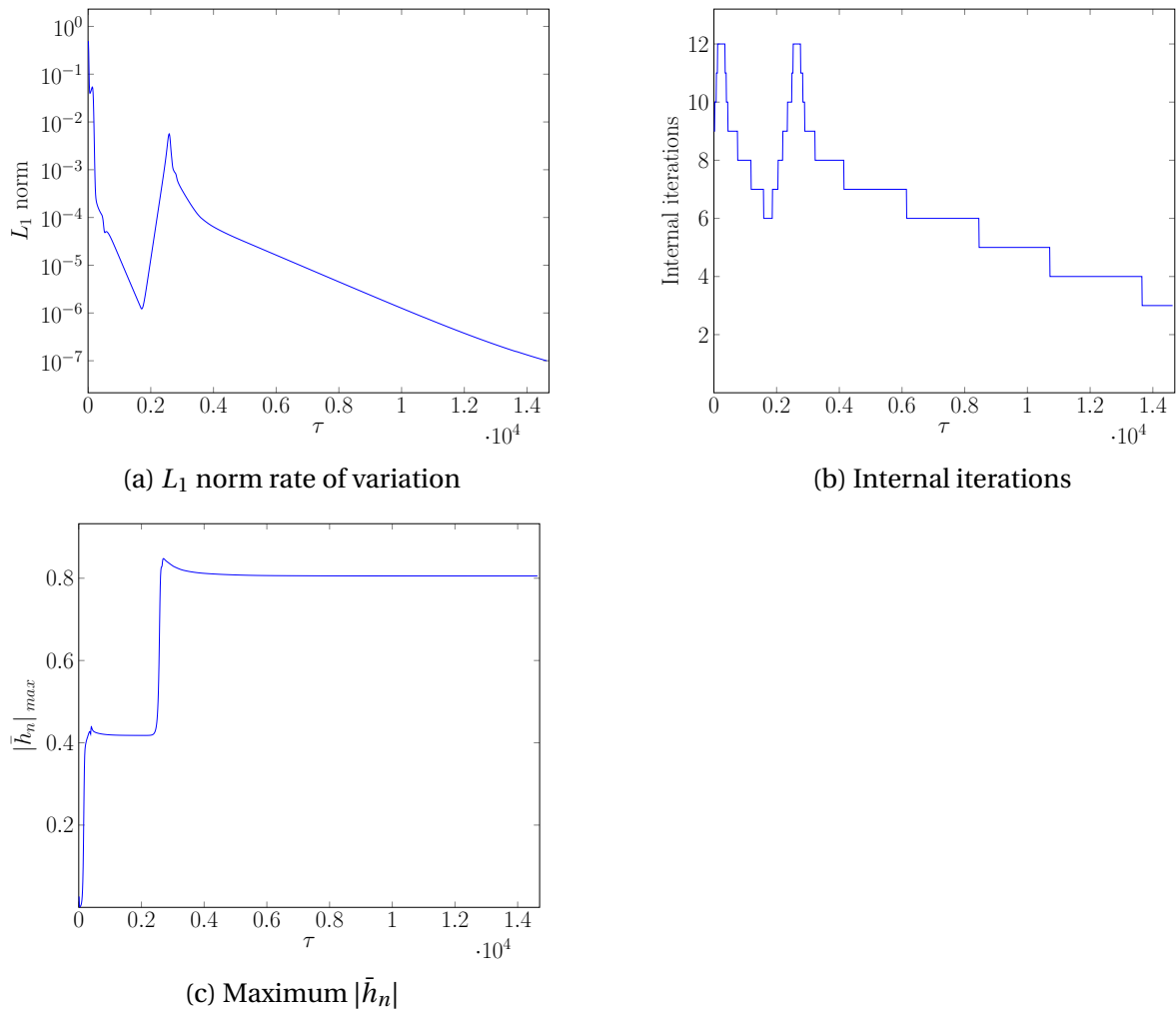


Figure 52:  $L_1$  norm, internal iterations and maximum values for  $\bar{h}_n$  as a function of time  $\tau$ , for an initial pattern with  $\vec{q} = q_0 \vec{1}_X$  (inside the stable domain),  $\Delta\tau = 0.1$ ,  $\Delta X = \Delta Y = 1$ , on a  $512 \times 512$  nodes domain

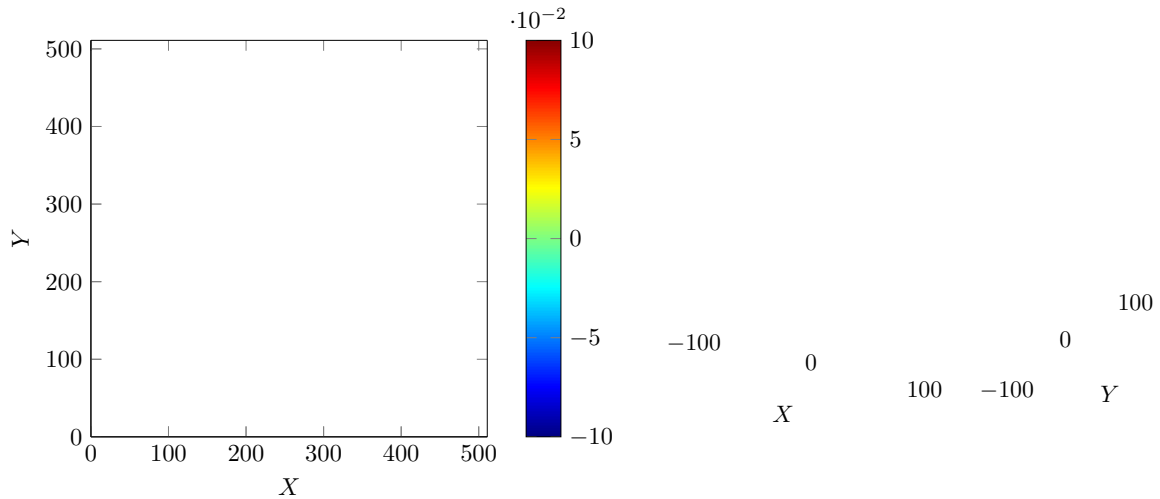


Figure 53: Surface height values  $\bar{h}_n$  and their respective Fourier Transform for  $\tau = 0$  (initial monomodal pattern with  $\vec{q} = q_o \vec{1}_X$ ).

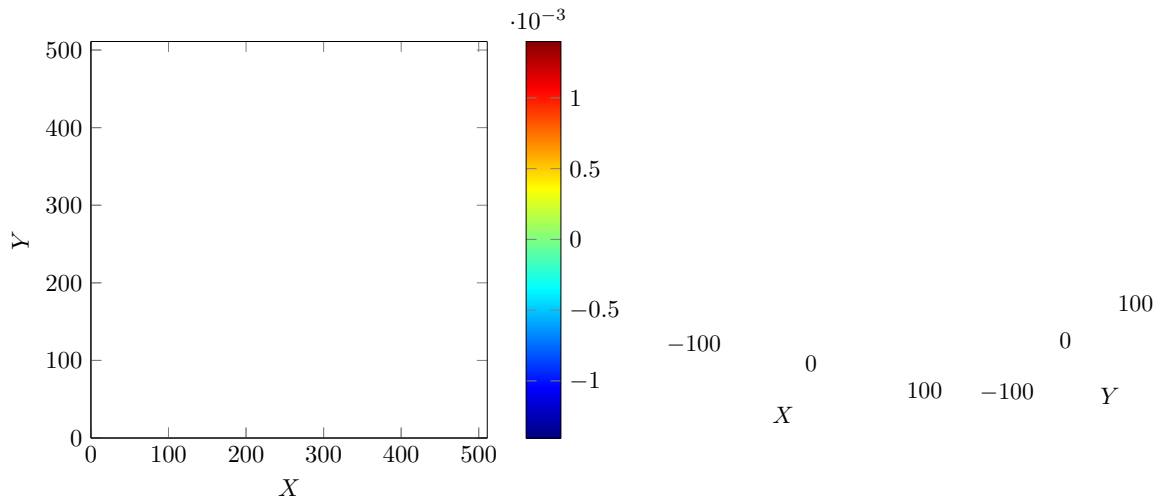


Figure 54: Surface height values  $\bar{h}_n$  and their respective Fourier Transform for  $\tau = 30$ .

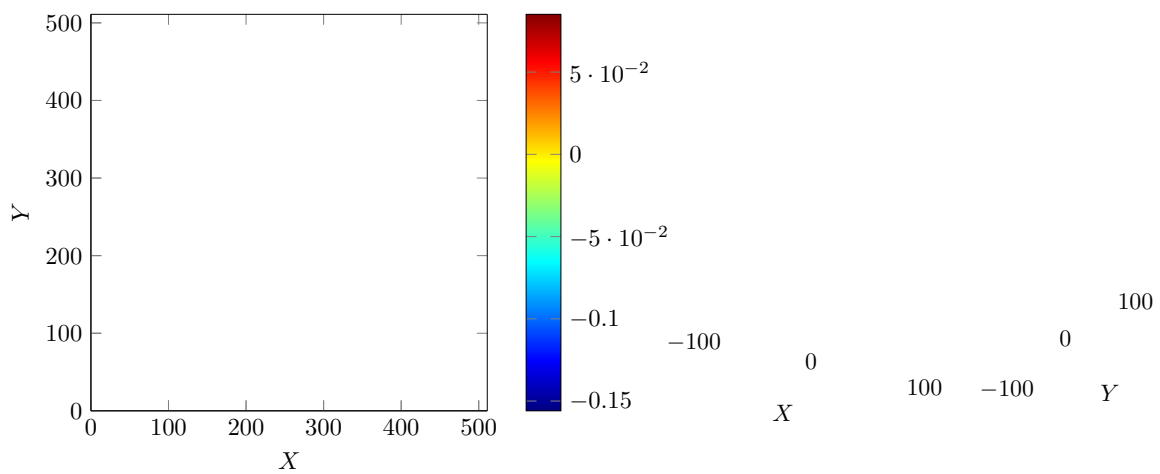


Figure 55: Surface height values  $\bar{h}_n$  and their respective Fourier Transform for  $\tau = 150$ .

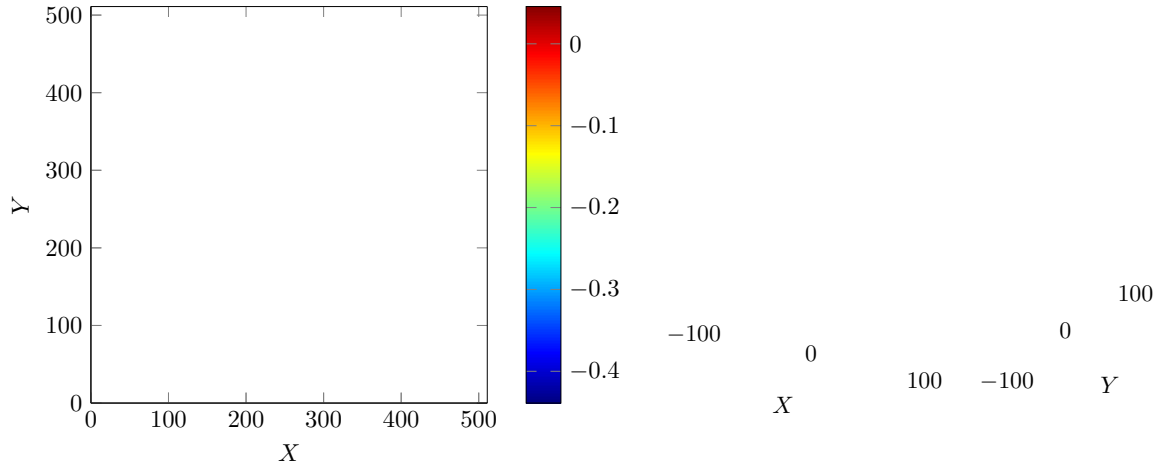


Figure 56: Surface height values  $\bar{h}_n$  and their respective Fourier Transform for  $\tau = 400$ .

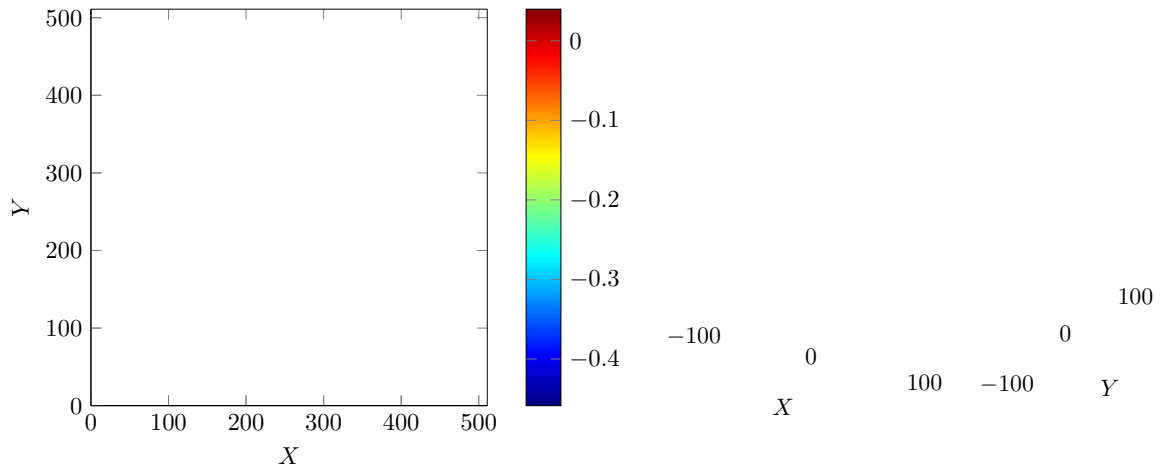


Figure 57: Surface height values  $\bar{h}_n$  and their respective Fourier Transform for  $\tau = 2500$ .

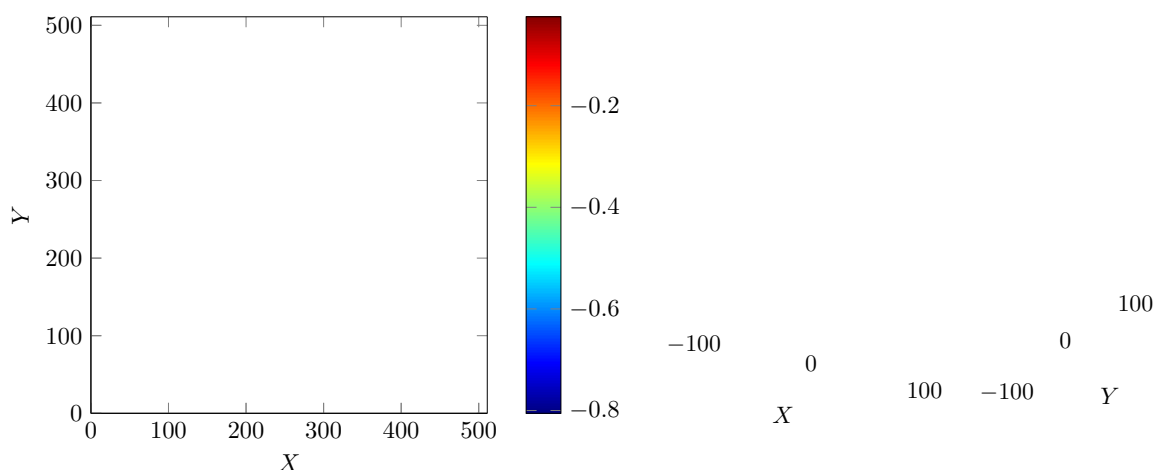


Figure 58: Surface height values  $\bar{h}_n$  and their respective Fourier Transform for  $\tau = 14630$ . A nanohole defectless pattern is obtained in the steady state.

## 5 ADVANCED RESULTS

### 5.1 The damping term effect

As previously mentioned, the damping term is a controversial one: while it is an interesting addition to the KS equation in order to obtain stationary patterns, the physical meaning is not sufficiently clear up to this moment. The present study adopts the aforementioned time splitting finite-difference method to acquire solutions for the two-dimensional DKS equation under 3 circumstances:  $\alpha = 0$ ,  $\alpha = 0.05$ , and  $\alpha = 0.15$ . The mesh consisted of  $512 \times 512$  points with a harmonic monomodal initial pattern in the  $\vec{I}_x$  direction ( $\vec{q} = q_0 \vec{I}_x$ ), a small amplitude of 0.1, and parameters  $\theta$ ,  $K$  and  $a_\mu$  as found in Table 4. Recapping the results from the linear stability analysis, a value of  $\lambda_c = 18$  was calculated for the critical wavelength, corresponding to the maximum growth rate in the  $\vec{I}_x$  direction. In this sense, each wavelength of the final pattern was estimated to be represented by 18 points.

According to the previous work of Paniconi and Elder [41], three distinct solutions in the late time limit might be expected for the DKS equation, depending on the parameter  $\alpha$ : periodic large hexagonal morphology for higher values, an oscillatory or breathing hexagonal state for middle values, and a spatiotemporal chaotic state for lower values. However, since the present endeavor considers realistic coefficients related to the physics of sputtering, the same range of  $\alpha$  values employed by Paniconi and Elder would not produce the same effects. Besides, in opposition to Paniconi and Elder, our study deals with an anisotropic DKS equation. Thereafter, during the first moments, linear effects lead to the selection of a well defined ripple direction; then, once nonlinear effects take over the system, cellular structures will develop (clearly seen on the  $\alpha = 0.15$  case).

The undamped solution is shown in Figure 59, when  $\alpha = 0$ . The initial condition presented a wavenumber  $q_o = 1.7181 \cdot 10^{-1}$  (14 wavelengths in the system). A disordered chaotic cellular structure is obtained for late time, with large variations of cell size and shape, as displayed in Figure 59a for  $\tau = 11803$ . From the  $L_1$  curve (Figure 59b), we can see that the chaotic pattern is reached within  $\tau = 500$ . While a steady state isn't reached for the analyzed period, it is clear that the evolution dynamics are much slower during late time.

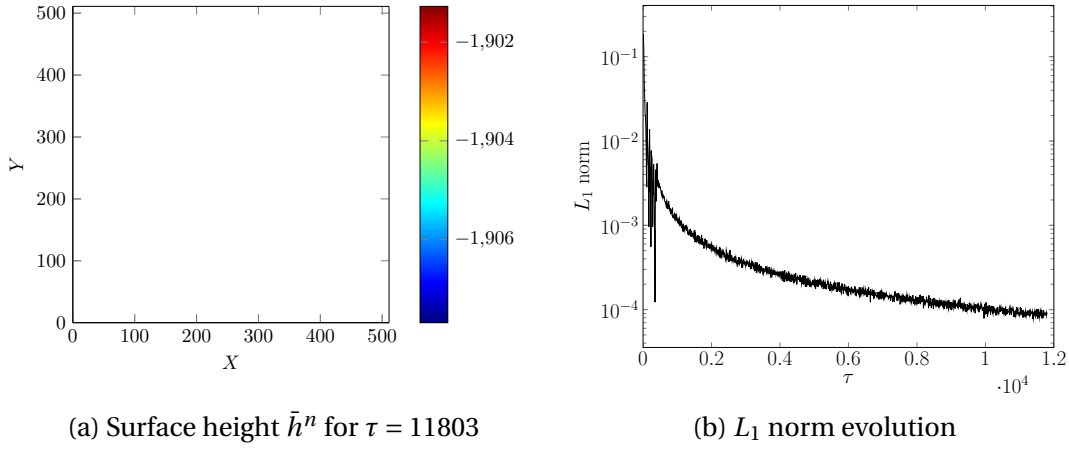


Figure 59: Numerical solution for a 2D anisotropic DKS equation - Spatiotemporal chaotic pattern,  $\alpha = 0$

Figure 60 reveals the numerical solution for  $\alpha = 0.05$ . The initial condition was the same from the previous case ( $q_o = 1.7181 \cdot 10^{-1}$ ). A spatiotemporal chaotic cellular structure is obtained for late time, which can be seen in Figure 59a for  $\tau = 11,750$ . In comparison with the undamped structure, the late time pattern for  $\alpha = 0.05$  is much more organized, with a smaller variation of cell sizes and shapes, with some of them approaching the  $\lambda_c$  width. The  $L_1$  norm evolution (Figure 60b) shows that a strongly oscillatory state is reached by  $\tau = 2,000$ , where  $L_1$  starts fluctuating around  $L_1 = 0.02$ . These intense dynamics differ from the undamped case: even though the structure is more organized, it keeps changing at a constant rate for an undefined period of time.

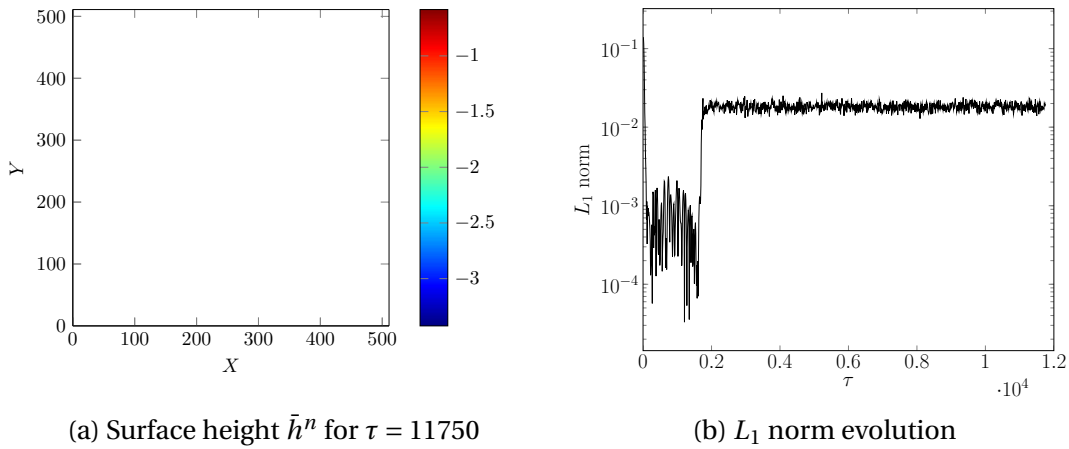


Figure 60: Numerical solution for a 2D anisotropic DKS equation - Chaotic semi-organized oscillatory behavior,  $\alpha = 0.05$

For higher values of  $\alpha$ , e.g.  $\alpha = 0.15$ , a defect-free hexagonal structure can be obtained, as displayed by Figure 61. A smaller wavenumber  $q_o = 2.4544 \cdot 10^{-2}$  was employed for the initial condition, since our previous studies revealed that an 1D structure with wavelength similar to  $\lambda_c$  would prevail for  $q_o = 1.7181 \cdot 10^{-1}$  even in late time. Figure 61b shows that at first the  $L_1$  norm has a continuous decline, which represents the stabilization of an 1D structure with  $\vec{q} \sim \vec{q}_c$ . Even though this pattern seems to be approaching a steady state, hexagonal modes emerge when  $\tau$  is approaching  $\tau = 2,000$ , leading to a fast growth of  $L_1$ , and to the formation of a new structure. Posteriorly,  $L_1$  reaches a peak, and the structure initiates its final stabilization, quickly removing defects and descending up to the stationary state, which is illustrated by Figure 61a for  $\tau = 14,630$ .

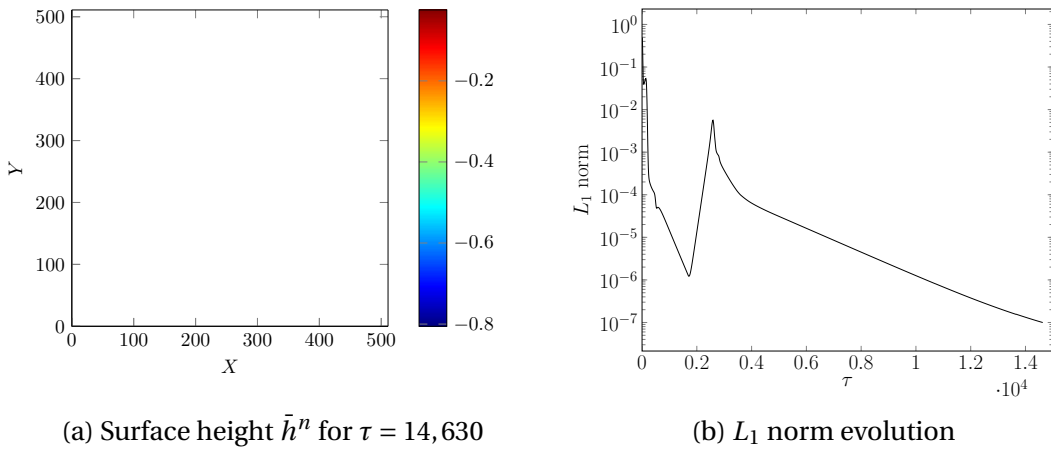


Figure 61: Numerical solution for a 2D anisotropic DKS equation - Stationary hexagonal structure,  $\alpha = 0.15$

Comparing the structure evolution for  $\alpha = 0.15$  and  $\alpha = 0.05$ , we confirm the coincident time for the emergence of the hexagonal modes, close to  $\tau = 2000$ . For  $\alpha = 0.15$ , the damping effect is sufficient for an ordered and quick reorganization of the structure after a  $L_1$  peak, while for  $\alpha = 0.05$  the damping is not high enough to allow the nanostructure to reorganize itself into a perfectly ordered hexagonal state, and it keeps chaotically oscillating around the peak  $L_1$  value. Another observation concerning the obtained height values must be pointed out. All of them are negative, being consistent with the erosive phenomenon. However, for  $\alpha = 0$ , the mean height of the surface falls continuously with time, while maintaining the distance  $\bar{h}_{dif}$  between the minimum and maximum points around  $\bar{h}_{dif} = 6.4$ . For  $\alpha = 0.05$  the mean height remains approximately constant, around -0.5 and -3.5 ( $\bar{h}_{dif} \sim 3.0$ ), for an undefined time. Finally, for the steady state obtained with a damping  $\alpha = 0.15$ , the

maximum and minimum height values were, respectively, -0.03 and -0.81 ( $\bar{h}_{dif} = 0.78$ ).

The practical significance of those results is that the acquired structures might depend on the duration of the irradiation. For a short time-duration sputtering in a system with  $\alpha = 0.15$ , we observe only the formation of ripples, while hexagons may emerge for a longer duration of the experiment. In contrast, for a system with  $\alpha = 0$  or 0.05, the final structure will depend on time, since it keeps changing with the irradiation duration.

## 5.2 Anisotropy and angle of incidence

The weakly nonlinear analysis developed by Walgraef [42] investigated the parameters involved in the relative anisotropy of the resulting patterns, through the Fourier transform and adiabatic elimination. The relative anisotropy is studied by  $A = \frac{\Delta}{\bar{K}q_c^4}$ , where  $q_c$  is the critical wavenumber obtained from our previous linear stability analysis, and  $\Delta = \frac{3}{4}(|\bar{\mu}| - |\bar{v}|)q_c^2$ . Figure 62 plots the relative anisotropy  $A$  versus  $\theta$  for  $\bar{K} = 5$  and  $a_\mu = 4$ . From the plot we observe that  $A$  for  $\theta = 0.5236$  ( $30^\circ$ ) is approximately 1.15, which was the value used up to this moment. The following results investigate the effect of varying the angle of incidence in the resulting pattern, motivated by this behavior of the relative anisotropy.

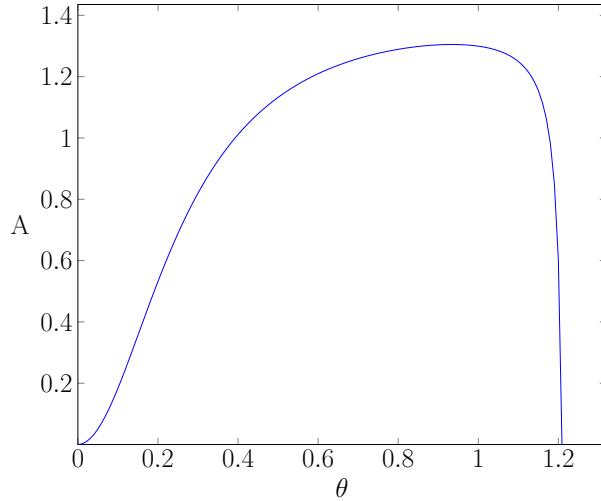


Figure 62: Relative anisotropy  $A$  versus  $\theta$  for  $\bar{K} = 5$  and  $a_\mu = 4$

One region we are particularly interested is near  $\theta = 1.2$ , since  $v_x$  and  $v_y$  may present opposite signs with similar modulus. This observation implies that there will be one direction for the unstable modes where the nonlinear terms will compensate each other, as studied in the work of Rost and Krug [17]. For this simulation, we defined a  $\theta$  value of 1.1549 ( $66.17^\circ$ ),

which means that we will have the following anisotropy coefficients:  $\nu_x = 0.0658$  and  $\nu_y = -0.0659$ .

Before showing the results for our case related to the sputtering model, we would like to show a reproduction of the results from Rost and Krug. More clearly, we have introduced their same parameters in our code to compare the numerical results, which is an opportunity to present another proof of reliability for the numerical method employed in the present endeavor. The equation reproduced was the following:

$$\frac{\partial \bar{h}}{\partial \tau} = -\frac{\partial^2 h}{\partial X^2} - \alpha \frac{\partial^2 h}{\partial Y^2} + \frac{1}{2} \left[ \left( \frac{\partial h}{\partial X} \right)^2 + \beta \left( \frac{\partial h}{\partial Y} \right)^2 \right] - \left( \frac{\partial^4 h}{\partial X^4} + 2 \frac{\partial^4 h}{\partial X^2 \partial Y^2} + \frac{\partial^4 h}{\partial Y^4} \right) \quad (5.1)$$

Rost and Krug studied this equation evolution when  $\alpha = 1$  and  $\beta = -1$ . In this situation, the cancellation of the two nonlinearities can break down the stabilization mechanism. Figure 63 shows their result for a system of size  $500 \times 500$  starting from a random initial condition. Several parallel ridges nucleate and grow from the random background, spreading over the system. Solving Equation 5.1 with our semi-implicit splitting scheme, we obtained the results shown by Figure 64 ( $L_1$  rate of variation per time) and Figure 65.

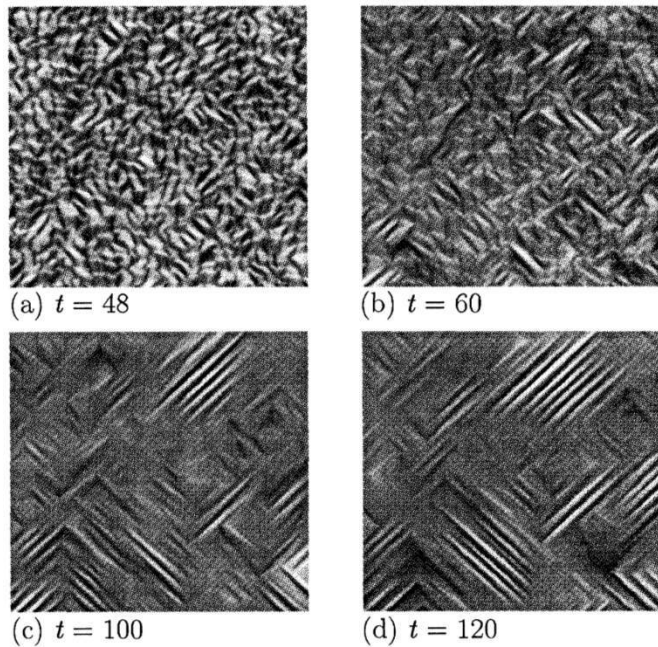


Figure 63: Numerical result of Eq. 5.1 obtained by Rost and Krug (1995) [17]. The parameters were  $\alpha = 1$  and  $\beta = -1$  in order to cancel the nonlinearities. Parallel ridges nucleate and coalesce, taking over the system.

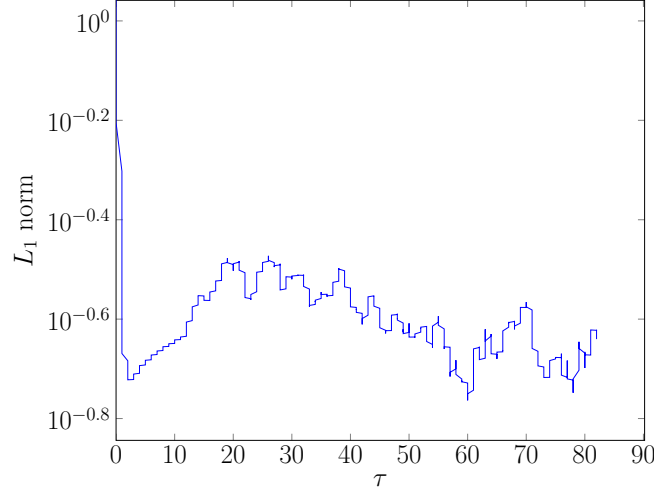


Figure 64:  $L_1$  norm rate of variation per time for the reproduction of the results from Rost and Krug with the semi-implicit time splitting scheme.

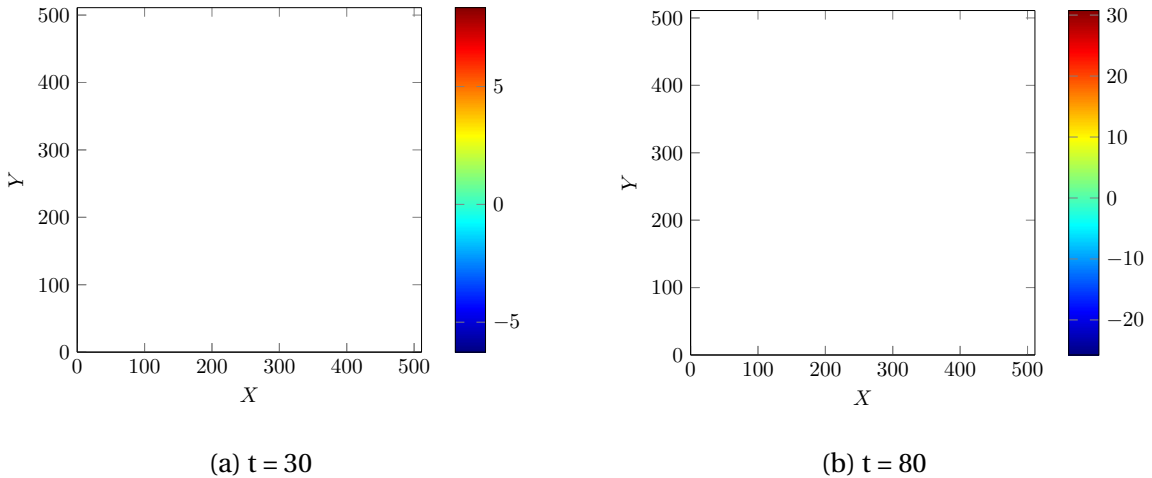


Figure 65: System of size  $512 \times 512$ , showing the evolution in time of Equation 5.1 with  $\Delta\tau = 0.01$ ,  $\alpha = 1$  and  $\beta = -1$ . The numerical results obtained through the semi-implicit time splitting reveals the nucleation and growth of parallel ridges.

As expected, the coalescence of parallel ridges were also present in our results, providing here another proof of reliability for the implemented scheme. We now proceed to the simulation of Equation 2.3 with  $\theta = 66.17^\circ$ , with the parameters informed by Table 5. The damping coefficient was chosen as  $\alpha = 0.1$  because of undesirable effects brought to the dynamics for this range of  $\theta$  by higher values of  $\alpha$  (heavy damping may lead to the disappearance of the structure with continuous decay of the mean height modulus).

Figure 66 and Figure 67 display the result from the  $\theta = 66.17^\circ$  simulation. In fact, the nonlinearities compensate each other when the system chooses the  $\vec{I}_x$  direction for the unstable modes. The nanostructure obtained for  $\tau = 180$  is still irregular in terms of the ripple

Table 5: Parameters for the  $66.17^\circ$  simulation

Parameter	Values	Description
L	256	domain side
$\bar{\alpha}$	0.10	damping coefficient
$\bar{K}$	5	surface diffusion effects
$\Delta X, \Delta Y$	1	space step
$\theta$	$66.17^\circ$	angle of incidence of the beam
$\Delta\tau$	0.001	time step
$a_\mu$	4	penetration depth/width of energy distribution

behavior, but the direction of preference is clear. There are approximately 23 wavelengths in the domain, which is less than the critical number of wavelengths from the linear stability analysis. In this case, we did not obtain a stationary structure, since the irregular ripple behavior keeps moving, although the pattern's preferred direction remains the same. This is sensed by the  $L_1$  rate of change in time, as it stabilizes around  $1 \times 10^{-1.8}$ , when the structure reaches a configuration similar to  $\tau = 180$  without ceasing the ripples' movement.

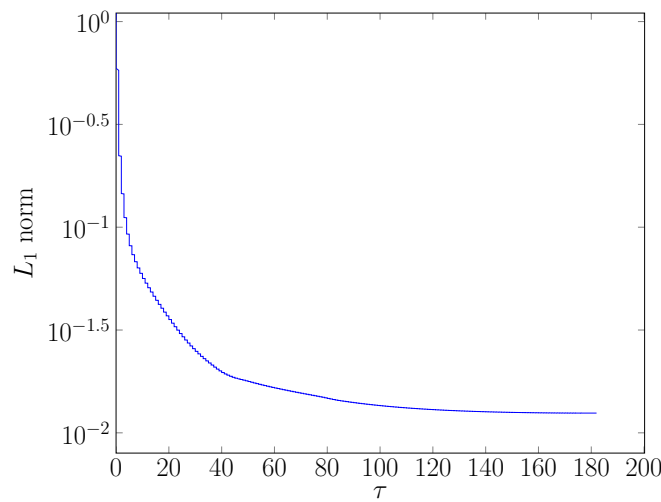


Figure 66:  $L_1$  norm rate of change per time for  $\theta = 66.17^\circ$ . Movements in the structure remain until the end, without reaching a stationary state.

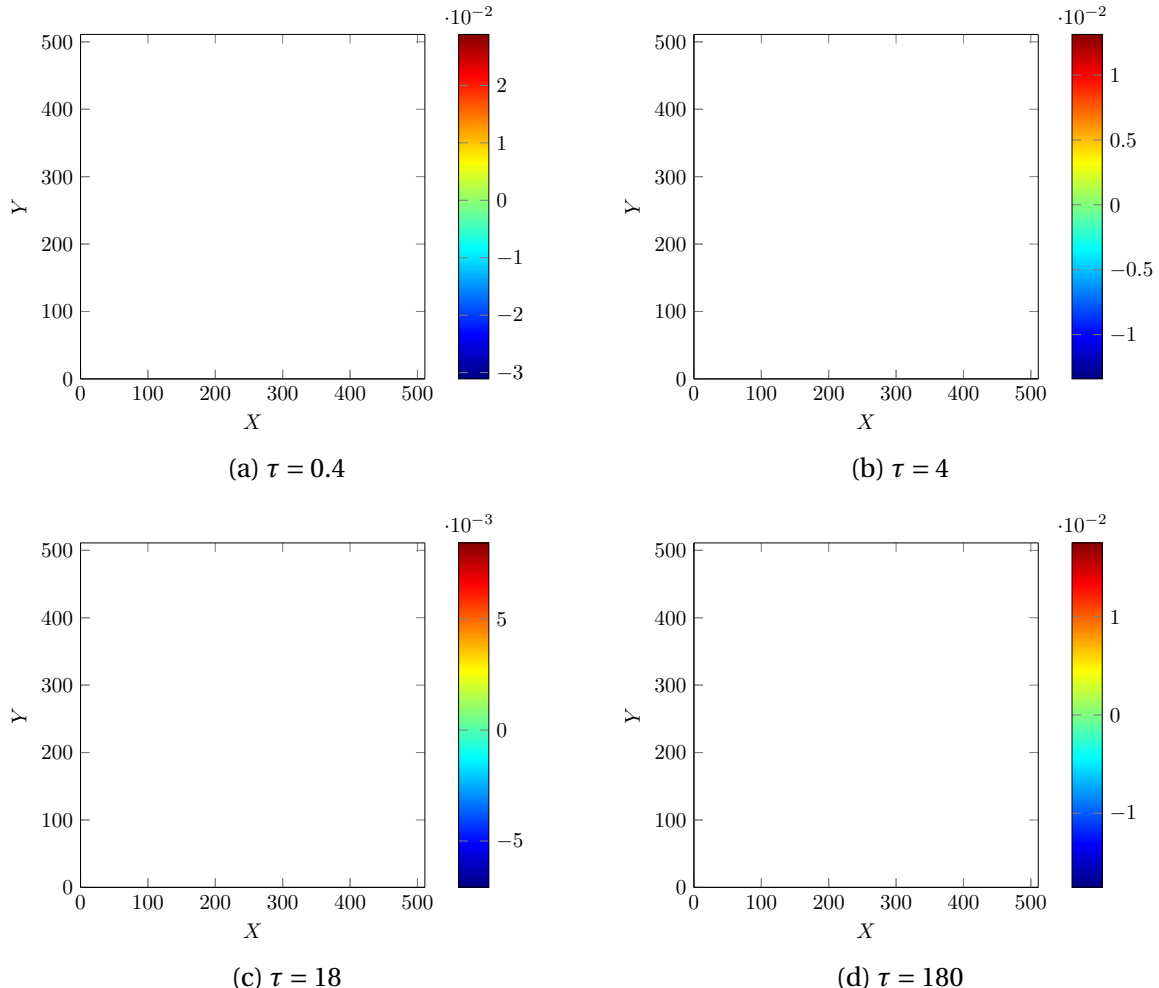


Figure 67: Simulation results for a system  $512 \times 512$  with an angle  $\theta = 66.17^\circ$ . The nonlinearities cancel each other and a well defined direction arises from the unstable mode. This is made clear by the selection of the  $\vec{1}_x$  direction for  $\tau = 180$ .

Next, the anisotropy investigation due to angle variations moves toward higher values for the relative anisotropy. Here we conducted simulations for  $\theta = 40^\circ$ , aiming to find the possible differences that could be introduced in the structure by the anisotropy, in relation to the previous studied  $\theta = 30^\circ$  cases. Therefore, the employed parameters were the same as those used throughout Chapter 3, except for the angle of incidence. The initial condition for the following case was a monomodal pattern with  $\vec{q} = q_0 \vec{1}_Y$  ( $q_0 = 2.5771 \cdot 10^{-2}$ ), which presented the same final morphology as the one obtained from a random initial profile.

Figure 68 suggests that the stationary state is reached as the  $L_1$  rate of change decreases in the late time until the stop criterion is reached ( $L_1 = 1 \cdot 10^{-7}$ ). The hexagonal modes emerge around  $\tau = 500$ , and they start to reorganize in structure, as seen in Figure 69 (a). A defectless pattern is obtained from this nonequilibrium dynamics, clearly shown by Figure 69 (b). A clean

spectrum of the most relevant modes (central part) acquired by the Fast Fourier Transform is displayed by Figure 69 (d). However, the final pattern is different from the  $\theta = 30^\circ$  case: here, the anisotropy effects lead to a diagonal connection between the cellular structure, resembling diagonal chains. This morphology is evident in the zoomed image from Figure 69 (c).

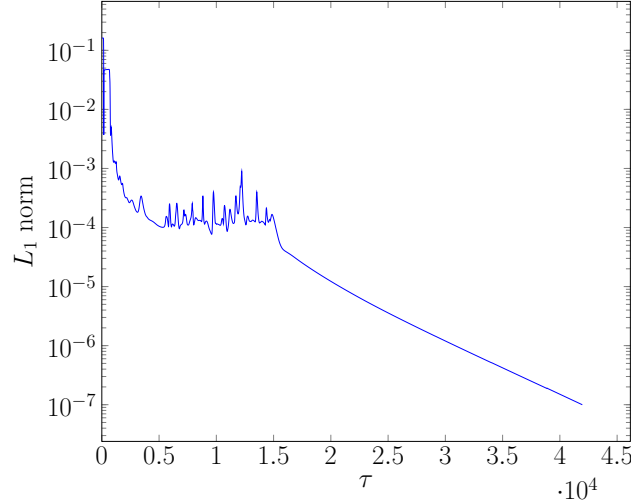


Figure 68:  $L_1$  norm rate of change per time for  $\theta = 40^\circ$ . Hexagonal modes emerge around  $\tau = 500$  and the stationary state criteria is met at  $\tau = 41,960$ .

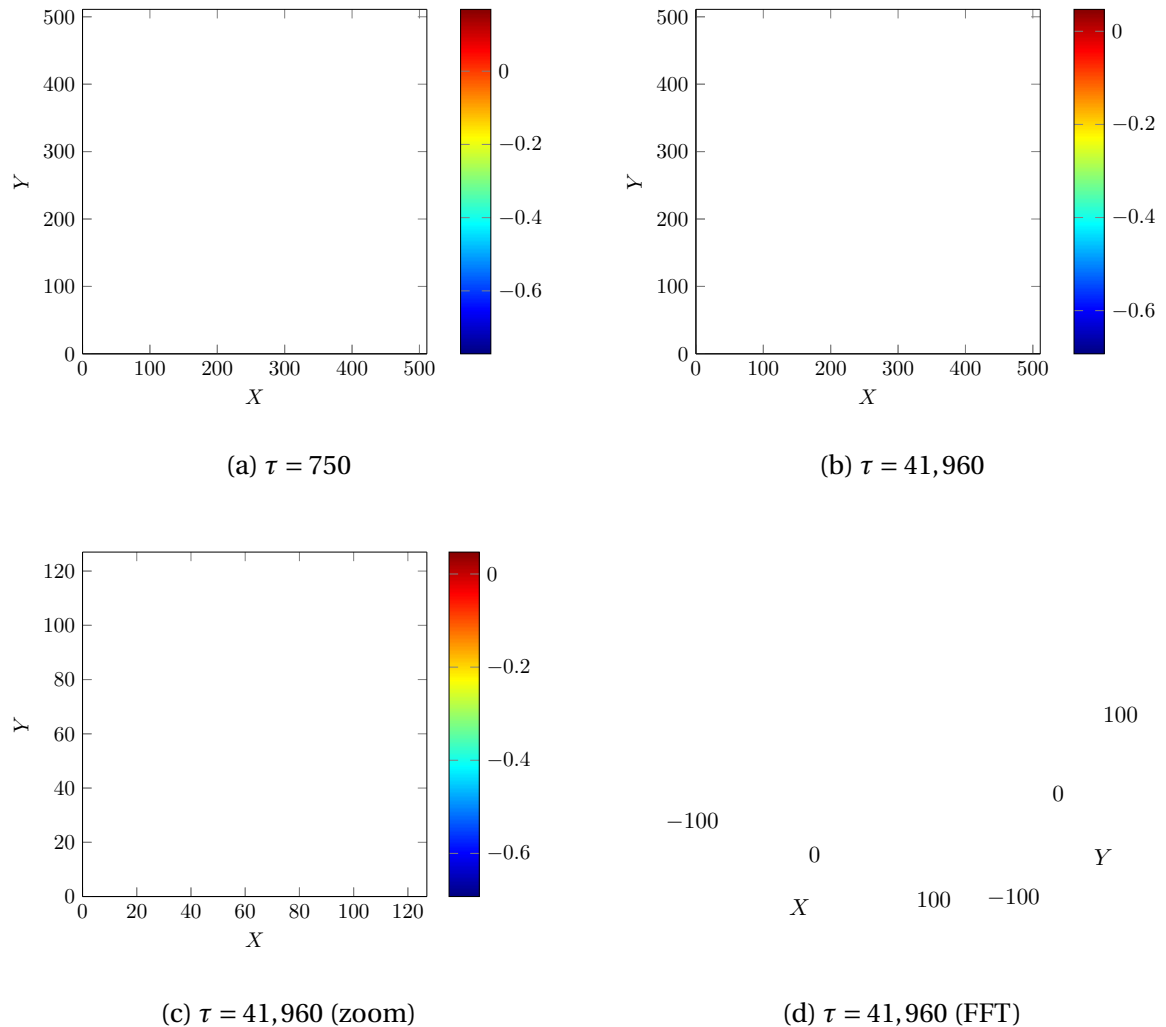


Figure 69: Simulation results for a system  $512 \times 512$  with an angle  $\theta = 40^\circ$ . Hexagonal modes emerge and reorganize the structure. The final pattern displays the cells connected in the diagonal, like chains.

## CONCLUSION

In the present work we have developed a finite-difference time splitting scheme to solve an anisotropic damped Kuramoto-Sivashinsky equation, which comes from the continuum theory and is an option to describe a surface eroded by ion bombardment. We dealt with realistic coefficients in a dimensionless analysis.

The MMS was employed for code verification, and a second-order convergence was detected for coarser meshes comparison, while results between first and second-order convergence came up for more refined meshes, suggesting a possible issue with the manufactured solution stability. Regarding the scheme's stability, the tests revealed that for  $\Delta\tau \leq 2.0$ , the numerical scheme was sufficiently stable with a grid spacing  $\Delta X = 1.0$ .

Spatiotemporal chaotic structures appeared for the undamped case, whose dynamics fell continuously for the long time. A chaotic oscillatory pattern rose from the simulation with  $\alpha = 0.05$ , reaching a better ordered structure than the one for the undamped result, while maintaining a highly constant kinematic after the emergence of the hexagonal modes. Defectless hexagonal periodic structures were obtained for higher values of the damping coefficient, with an angle of incidence  $\theta = 30^\circ$ .

We performed a linear stability analysis, and used its results to guide our investigations on the evolution of the anisotropic DKS equation on preexisting patterns. There was a thorough discussion concerning the regimes before and after the emergence of hexagonal modes. Nanohole patterns were obtained in the long time for the majority of the evaluated initial patterns, using  $\theta = 30^\circ$ . Small variations in the wavenumber of the monomodal starting morphology were able to influence the retention of defects in the final structure.

Based on the previous work of Rost and Krug, we investigated a case when the nonlinearities compensate each other. This was achieved using  $\theta = 66.17^\circ$ , and an irregular oscillatory ripple structure with a clear orientation in the  $\vec{t}_X$  direction was obtained.

In summary, it is possible to affirm that the obtained results were physically consistent with the sputtering phenomenon, reproducing ripple morphologies and nanohole pattern formation experimentally attained by other authors. Further works could make advances in the investigation of the anisotropic DKS equation coefficients, seeking the possible acquisition of new kinds of patterns with the simulations. A reproduction of nanodot structures would be particularly interesting.

**APPENDIX A - PUBLICATIONS**

- ★ VITRAL, E., WALGRAEF D., PONTES, J., ANJOS, G.R., MAGIAVACCHI, N. *Nano-patterning of surfaces by ion sputtering: numerical study of the Kuramoto-Sivashinsky equation by implicit time splitting*, Proceedings of the ABM Week 70th Annual Congress, 2015.
- ★ VITRAL, E., WALGRAEF D., PONTES, J., ANJOS, G.R., MAGIAVACCHI, N. *Nano-patterning of surfaces by ion sputtering: numerical study of the damping effect on the anisotropic Kuramoto-Sivashinsky equation*, Proceedings of the 23rd ABCM International Congress of Mechanical Engineering, 2015.

## REFERENCES

- [1] LEFEVER, R.; LEJEUNE, O. On the origin of tiger bush. *Bulletin of Mathematical Biology*, Springer, v. 59, n. 2, p. 263–294, 1997.
- [2] NICOLIS, G.; PRIGOGINE, I. et al. *Self-organization in nonequilibrium systems*. [S.l.]: Wiley, New York, 1977.
- [3] PONTES, J. Determinism, chaos, self-organization and entropy. *Annals of the Brazilian Academy of Sciences*, p. to appear, 2015 (accepted).
- [4] KRINSKY, V. *Self-organization: autowaves and structures far from equilibrium*. [S.l.]: Springer, 1984.
- [5] WALGRAEF, D. Patterns, defects and microstructures in nonequilibrium systems: Applications in materials sciences; proceedings of the nato advanced research workshop, university of texas, austin, mar. 24-28, 1986. In: *Workshop organised by the University of Texas and Universite Libre de Bruxelles; Supported by NATO and NSF Dordrecht, Martinus Nijhoff Publishers (NATO ASI Series, No. E121)*, 1987, 395 p. *No individual items are abstracted in this volume*. [S.l.: s.n.], 1987. v. 1.
- [6] CHASON, E.; CHAN, W. L. Spontaneous patterning of surfaces by low-energy ion beams. In: *Materials Science with Ion Beams*. [S.l.]: Springer, 2010. p. 53–71.
- [7] GAGO, R. et al. Temperature influence on the production of nanodot patterns by ion beam sputtering of si (001). *Physical Review B*, APS, v. 73, n. 15, p. 155414, 2006.
- [8] WEI, Q. et al. Self-assembly of ordered semiconductor nanoholes by ion beam sputtering. *Advanced Materials*, Wiley Online Library, v. 21, n. 28, p. 2865–2869, 2009.
- [9] MOLLICK, S. A.; GHOSE, D.; SATPATI, B. Formation of au–ge nanodots by au- ion sputtering of ge. *Vacuum*, Elsevier, v. 99, p. 289–293, 2014.
- [10] GHONIEM, N. et al. Sputtering of molybdenum and tungsten nano rods & nodules irradiated with 150 ev argon ions. *Applied Surface Science*, Elsevier, 2015.

- [11] ASTE, T.; VALBUSA, U. Ripples and ripples: from sandy deserts to ion-sputtered surfaces. *New Journal of Physics*, IOP Publishing, v. 7, n. 1, p. 122, 2005.
- [12] PATTERN Formation with Ions - HZDR Webpage.  
[www.hzdr.de/db/Cms?p0id=24344&pNid=2707](http://www.hzdr.de/db/Cms?p0id=24344&pNid=2707). Retrieved: 15-10-14.
- [13] SAND Ripples, Namib Desert - Redbubble Webpage.  
[www.redbubble.com/people/jasonpomerantz/works/6357267-sand-ripples-namib-desert](http://www.redbubble.com/people/jasonpomerantz/works/6357267-sand-ripples-namib-desert). Retrieved: 14-10-14.
- [14] RIPPLED clouds - Flickr/Rebecca Coleman.  
[www.flickr.com/photos/61603002@N07/5640249650/](http://www.flickr.com/photos/61603002@N07/5640249650/). Retrieved: 28-03-15.
- [15] MAKEEV, M. A.; CUERNO, R.; BARABÁSI, A.-L. Morphology of ion-sputtered surfaces. *Nuclear Instruments and Methods in Physics Research Section B: Beam Interactions with Materials and Atoms*, Elsevier, v. 197, n. 3, p. 185–227, 2002.
- [16] KELLER, A.; FACKSKO, S. Ion-induced nanoscale ripple patterns on si surfaces: theory and experiment. *Materials*, Molecular Diversity Preservation International, v. 3, n. 10, p. 4811–4841, 2010.
- [17] ROST, M.; KRUG, J. Anisotropic kuramoto-sivashinsky equation for surface growth and erosion. *Physical review letters*, APS, v. 75, n. 21, p. 3894, 1995.
- [18] CHRISTOV, C. et al. Implicit time splitting for fourth-order parabolic equations. *Computer methods in applied mechanics and engineering*, Elsevier, v. 148, n. 3, p. 209–224, 1997.
- [19] CHRISTOV, C.; PONTES, J. Numerical scheme for swift-hohenberg equation with strict implementation of lyapunov functional. *Mathematical and computer modelling*, Elsevier, v. 35, n. 1, p. 87–99, 2002.
- [20] BEHRISCH, R.; ECKSTEIN, W. *Sputtering by Particle Bombardment: Experiments and Computer Calculations from Threshold to MeV Energies*. [S.l.]: Springer Berlin Heidelberg, 2007. (Topics in Applied Physics).
- [21] OHRING, M. *Materials Science of Thin Films*. [S.l.]: Academic Press London, 2002.

- [22] TRIMBLE, L.; CELLER, G. Evaluation of polycrystalline silicon membranes on fused silica for x-ray lithography masks. *Journal of Vacuum Science & Technology B*, AVS: Science & Technology of Materials, Interfaces, and Processing, v. 7, n. 6, p. 1675–1679, 1989.
- [23] SIGMUND, P. Theory of sputtering. i. sputtering yield of amorphous and polycrystalline targets. *Physical Review*, American Physical Society, v. 184, p. 383–416, 1969.
- [24] JOHNSON, R.; EVATT, R. Thermal spikes and sputtering yields. *Radiation Effects*, Taylor & Francis, v. 52, n. 3-4, p. 187–190, 1980.
- [25] HOFER, W.; BESOCKE, K.; STRITZKER, B. A search for a thermal spike effect in sputtering. *Applied Physics A*, Springer, v. 30, n. 2, p. 83–86, 1983.
- [26] FACKSKO, S. et al. Formation of ordered nanoscale semiconductor dots by ion sputtering. *Science*, American Association for the Advancement of Science, v. 285, n. 5433, p. 1551–1553, 1999.
- [27] FACKSKO, S. et al. Dissipative continuum model for self-organized pattern formation during ion-beam erosion. *Physical Review B*, APS, v. 69, n. 15, p. 153412, 2004.
- [28] FROST, F.; SCHINDLER, A.; BIGL, F. Roughness evolution of ion sputtered rotating inp surfaces: pattern formation and scaling laws. *Physical review letters*, APS, v. 85, n. 19, p. 4116, 2000.
- [29] BRADLEY, R. M.; HARPER, J. M. Theory of ripple topography induced by ion bombardment. *Journal of Vacuum Science & Technology A*, AVS: Science & Technology of Materials, Interfaces, and Processing, v. 6, n. 4, p. 2390–2395, 1988.
- [30] KURAMOTO, Y.; TSUZUKI, T. Persistent propagation of concentration waves in dissipative media far from thermal equilibrium. *Progress of theoretical physics*, Oxford University Press, v. 55, n. 2, p. 356–369, 1976.
- [31] CUERNO, R.; BARABÁSI, A.-L. Dynamic scaling of ion-sputtered surfaces. *Physical review letters*, APS, v. 74, n. 23, p. 4746, 1995.
- [32] VALBUSA, U.; BORAGNO, C.; MONGEOT, F. B. de. Nanostructuring surfaces by ion sputtering. *Journal of Physics: Condensed Matter*, IOP Publishing, v. 14, n. 35, p. 8153, 2002.

- [33] DOUGLAS, J.; RACHFORD, H. H. On the numerical solution of heat conduction problems in two and three space variables. *Transactions of the American mathematical Society*, JSTOR, p. 421–439, 1956.
- [34] YANENKO, N. N. *The method of fractional steps*. [S.l.]: Springer, 1971.
- [35] GHONIEM, N.; WALGRAEF, D. *Instabilities and Self-organization in Materials*. [S.l.]: Oxford Univ. Press, 2008.
- [36] BABUSKA, I.; ODEN, J. T. Verification and validation in computational engineering and science: basic concepts. *Computer Methods in Applied Mechanics and Engineering*, North-Holland, v. 193, n. 36, p. 4057–4066, 2004.
- [37] ROY, C. J. Review of code and solution verification procedures for computational simulation. *Journal of Computational Physics*, Elsevier, v. 205, n. 1, p. 131–156, 2005.
- [38] ROACHE, P. J. Code verification by the method of manufactured solutions. *Journal of Fluids Engineering*, American Society of Mechanical Engineers, v. 124, n. 1, p. 4–10, 2002.
- [39] MALAYA, N. et al. Masa: a library for verification using manufactured and analytical solutions. *Engineering with Computers*, Springer, v. 29, n. 4, p. 487–496, 2013.
- [40] STEINBERG, S.; ROACHE, P. J. Symbolic manipulation and computational fluid dynamics. *Journal of Computational Physics*, Elsevier, v. 57, n. 2, p. 251–284, 1985.
- [41] PANICONI, M.; ELDER, K. Stationary, dynamical, and chaotic states of the two-dimensional damped kuramoto-sivashinsky equation. *Physical Review E*, APS, v. 56, n. 3, p. 2713, 1997.
- [42] WALGRAEF, D. Nano-patterning of surfaces by ion sputtering: A proposal for a numerical study of the effect of preexisting patterns. Working notes, unpublished.